ROYAL INSTITUTE
OF TECHNOLOGY

Characterization of domain switching and optical damage properties in ferroelectrics

Junji Hirohashi

Doctoral Thesis
Department of Applied Physics
Royal Institute of Technology
Stockholm
Sweden
2006

Royal Institute of Technology
Department of Applied Physics –Laser Physics
Albanova
Roslagstullsbacken 21
SE-106 91 Stockholm, Sweden

Akademisk avhandling som med tillstånd av Kungliga Tekniska Högskolan framlägges till offentlig granskning för avläggande av teknologie doktorsexamen fysik, tisdagen den 26 september 2006, kl. 10 i Sal FB54, Albanova, Roslagstullsbacken 21, Stockholm.
Avhandligen kommer att försvaras på engelska.

TRITA-FYS 2006:59
ISSN 0280-316X
ISRN KTH/FYS/--06:59—SE

ISBN 91-7178-443-8

Cover: Schematics of periodically-poled structures consisting of 180°- and 90°-domains.

Printed by Universitetsservice AB, Stockholm 2006.

Junji Hirohashi
Characterization of domain switching and optical damage properties in ferroelectrics
Laser Physics and Quantum Optics, Department of Applied Physics, Royal Institute of Technology (KTH), SE-10691 Stockholm, Sweden.

Abstract

Nonlinear optical frequency conversion is one of the most important key techniques in order to obtain lasers with wavelengths targeted for specific applications. In order to realize efficient and tailored lasers, the quasi-phase-matching (QPM) approach using periodically-poled ferroelectric crystals is getting increasingly important. Also understanding of damage mechanisms in nonlinear materials is necessary to be able to design reliable and well working lasers. This is especially true for high power application lasers, which is a rapidly growing field, where the damage problem normally is the ultimate limiting factor.

In this thesis work, several promising novel ferroelectric materials have been investigated for nonlinear optical applications and the emphasis has been put on QPM devices consisting of periodically-poled structures. The materials were selected from three different types of ferroelectric materials: 1) MgO-doped stoichiometric $LiNbO_3$ (MgO:SLN) and $LiTaO_3$ (MgO:SLT), and non-doped stoichiometric $LiTaO_3$ (SLT), 2) $KTiOPO_4$ (KTP) and its isomorphs $RbTiOPO_4$ (RTP), and 3) $KNbO_3$ (KN). The focus in our investigations have been put on the spontaneous polarization switching phenomena, optimization of the periodic poling conditions, and the photochromic optical damage properties which were characterized by the help of blue light-induced infrared absorption (BLIIRA) measurements.

With electrical studies of the spontaneous polarization switching, we were able to determine quantitatively, and compare, the coercive field values of different materials by applying triangularly shaped electric fields. We found that the values of the coercive fields depended on the increase rate of the applied electric field. The coercive field of KN was the lowest (less than 0.5 kV/mm) followed by the ones of KTP, SLT, and MgO:SLT (1.5 to 2.5 kV/mm). MgO:SLN, and RTP had relatively high coercive fields, approximately 5.0 to 6.0 kV/mm, respectively. Based on the domain switching characteristics we found, we successfully fabricated periodically-poled devices in all of the investigated materials with 30 μm periodicities and sample thickness of 1 mm.

Blue light-induced infrared absorption (BLIIRA) has been characterized for unpoled bulk and periodically-poled samples using a high-sensitivity, thermal-lens spectroscopy technique. SLT showed a large photorefraction effect and the BLIIRA signal could not be properly measured because of the large distortion of the probe beam. The rise and relaxation time of BLIIRA, after switching the blue light on and off was in a time span of 10 to 30 sec except for KTP and its isomorphs, which needed minutes to hours in order to saturate at a fixed value. KN and MgO:SLN showed the lowest susceptibility to the induced absorption. Periodic poling slightly increased the susceptibility of KTP, MgO:SLT, and KN. Relatively high thresholds were observed in MgO:SLT and KN. By increasing the peak-power intensity of the blue light, the induced absorption for MgO:SLN, KTP and KN saturated at a constant value while that of MgO:SLT increase in a constant fashion. This trend is critical issue for the device reliability at high-power applications.

Keywords: quasi-phase matching, ferroelectric domains, stoichiometric $LiNbO_3$, stoichiometric $LiTaO_3$, $KTiOPO_4$, $KNbO_3$, polarization switching, periodic electric field poling, optical damages, grey tracking, blue light-induced infrared absorption

Preface

The thesis project has been made possible through generous grants from Göran Gustafsson Foundation as well as the Swedish Research Council.

The thesis has been carried out at two locations. Some parts of the electric-field poling and the domain characterization of $KNbO_3$ were done at Mitsui Chemicals, Inc. in Sodegaura, Japan. The other poling characterization and damage property measurements for the ferroelectrics were performed at The Royal Institute of Technology (KTH), Stockholm, Sweden.

List of publications

Publication included in this thesis

I. C. Canalias, **J. Hirohashi**, V. Pasiskevisius, and F. Laurell: “Polarization switching characteristics of flux grown $KTiOPO_4$ and $RbTiOPO_4$ at room temperature”, J. Appl. Phys. **97**, 124105 (2005).

II. **J. Hirohashi**, K. Yamada, H. Kamio, and S. Shichijyo: “Embryonic nucleation method for fabrication of uniform periodically poled structures in potassium niobate for wavelength conversion devices”, Jpn. J. Appl. Phys. **43**, p. 559 (2004).

III. **J. Hirohashi,** K. Yamada, H. Kamio, M. Uchida, and S. Shichijyo: “Controllability of specific domain structures in $KNbO_3$ single crystals by electric poling at room temperature”, J. Appl. Phys. **98,** 034107 (2005).

IV. **J. Hirohashi**, K. Yamada, H. Kamio, and S. Shichijyo: “Fabrication of 90-degree domain structures in $KNbO_3$ single crystals”, Ferroelectrics **282**, p. 29 (2003).

V. **J. Hirohashi** and V. Pasiskevicius: “Quasi-phase-matched frequency conversion in $KNbO_3$ structures consisting of 90-degree ferroelectric domains”, Appl. Phys. B **81**, p. 761 (2005).

VI. S. Shichijyo**, J. Hirohashi**, H. Kamio, and K. Yamada: “Total refraction of p-polarized light at the 90-degree domain boundary in the ferroelectric crystal”, Jpn. J. Appl. Phys. **43**, p. 3413 (2004).

VII. **J. Hirohashi**, V. Pasiskevicius, S. Wang, and F. Laurell: “Picosecond blue light-induced infrared absorption in single-domain and periodically poled ferroelectrics”, submitted to J. Appl. Phys.

Other publications by the author related to the subject, but not included in this thesis

A1. **J. Hirohashi**, K. Yamada, H. Kamio and S. Shichijyo: “Artificial fabrication of 60-degree domain structures in $KNbO_3$ single crystals”, J. Korean Phys. Soc. **42**, S1248 (2003).

A2. S. Shichijyo, **J. Hirohashi**, K. Yamada and H. Kamio: “Wide acceptance angle of second-harmonic green generation by periodically poled potassium niobate”, Jpn. J. Appl. Phys. **43**, p. 201 (2004).

A3. **J. Hirohashi**, K. Yamada, H. Kamio, and S. Shichijyo: “Compact integrated folded Solc filter using periodic 90-degree domain structures in $KNbO_3$ single crystals”, Jpn. J. Appl. Phys. **43**, p. 8069 (2004).

A4. N. E. Yu, S. Kurimura, K. Kitamura, O. Jeon, M. Cha, S. Ashihara, T. Ohta, T. Shimura, K. Kuroda, and **J. Hirohashi**: “Efficient broadband second harmonic generation of ultra-fast pulses in periodically-poled $KNbO_3$”, Appl. Phys. Lett. **85,** p. 5839 (2004).

These publications will be referred to in the text according to the notifications used here.

Contents

Chapter 1. Introduction **...** **1**
- 1.1. Aim and motivation 1
- 1.2. Outline of this thesis 3

Chapter 2. Basic principles of nonlinear optics **...** **7**
- 2.1. Introduction 7
- 2.2. The nonlinear polarization 7
- 2.3. Second-order nonlinear process and the d-coefficients 8
- 2.4. The coupled-wave equations 9
- 2.5. Phase-matching process 10
  - 2.5.1 Birefringent phase-matching 12
  - 2.5.2 Quasi-phase matching 12

Chapter 3. Nonlinear optical ferroelectrics **...** **15**
- 3.1. Introduction 15
- 3.2. Ferroelectric crystals 15
  - 3.2.1. Crystal symmetry 15
  - 3.2.2. Piezoelectricity 16
  - 3.2.3. Spontaneous polarization, pyroelectricity, and ferroelectrics 16
- 3.3. Crystal growth 17
  - 3.3.1. $LiNbO_3$ and $LiTaO_3$ 17
  - 3.3.2. $KTiOPO_4$ and its isomorphs 21
  - 3.3.3. $KNbO_3$ 23
- 3.4. Optical properties 29
  - 3.4.1. The d-coefficient and the figure of merit 29
  - 3.4.2. Transparency range 31
  - 3.4.3. Optical damage properties 31
  - 3.4.4. QPM periods 34

Chapter 4. Characterization of spontaneous polarization switching **..............** **37**
- 4.1. Introduction 37
- 4.2. Electric properties in spontaneous polarization switching 37
  - 4.2.1. The P-E hysteresis loop and the measurement setup 37
  - 4.2.2. Stoichiometric $LiNbO_3$ and $LiTaO_3$ 40
  - 4.2.3. $KTiOPO_4$ and its isomorphs 43
  - 4.2.4. $KNbO_3$ 45
  - 4.2.5. Dependence of the coercive field on the number of poling cycles 48
- 4.3. Domain morphology 50
  - 4.3.1. Domain characterization method 50
  - 4.3.2. $LiNbO_3$ and $LiTaO_3$ 50
  - 4.3.3. $KTiOPO_4$ and its isomorphs 51
  - 4.3.4. $KNbO_3$ 51
- 4.4. Summary 54

Chapter 5. Fabrication and characterization of periodically-poled devices **......** **57**
- 5.1. Introduction 57
- 5.2. Periodic-poling procedure 57

5.3. The poling setup 59
    5.3.1. The process monitoring method 59
    5.3.2. Effect of the serial resistance 60
    5.3.3. Electrode structures 61
5.4. Fabricating conditions of periodically-poled ferroelectrics 62
    5.4.1. Stoichiometric $LiNbO_3$ and $LiTaO_3$ 62
    5.4.2. $KTiOPO_4$ and its isomorphs 69
    5.4.3. $KNbO_3$ 70
5.5 Optical performances of the fabricated periodically-poled devices 75
    5.5.1. Comparison of OPOs pumped by pulsed 1064 nm laser 75
    5.5.2. Second harmonic generation by PP90KN 78

***Chapter 6. Comparison of laser-induced damage properties* 81**
6.1. Introduction 81
6.2. The BLIIRA measurement setup 82
6.3. The BLIIRA performance 83
    6.3.1 BLIIRA transitions when switching blue light on and off 84
    6.3.2 The BLIIRA dependences on the pulse intensities 87
6.4. Summary 89

***Chapter 7. Description of the original work and contribution by the candidate*... 93**

***Chapter 8. Summary* 97**

***Acknowledgement* 99**

Papers I – VII

Chapter 1. Introduction

1.1. Aim and motivation

Nonlinear optical frequency conversion is one of the most important key techniques to obtain lasers with wavelengths targeted for specific applications. There are several types of nonlinear frequency conversion, e.g., second-harmonic generation (SHG), sum-frequency generation (SFG), difference-frequency generation (DFG), optical parametric oscillation (OPO) and amplification (OPA). SHG, or frequency doubling, is the most common process used for frequency conversion from the near-infrared to the visible.1) SFG is also primarily used to get visible or UV light by the mixing of two different near infrared or visible light beams.2) SFG has also been demonstrated for wavelength sampling in an optical spectroscopy system.3) DFG has, for example, been used in frequency conversion between two different telecom frequency bands to obtain radiation in the mid-infrared region (THz radiation).4) OPOs or OPAs are employed for THz-wave generation or mid-infrared wave amplification often pumped by a pulsed laser such as a Q-switched Nd: YAG laser.5)

In order to realize those applications, ferroelectric crystals which have built-in electrical dipoles (spontaneous polarization) are widely used because of their efficient nonlinearity. When using these crystals, it is most important to have phase matched the incident beam(s) and the converted beam(s) inside the crystal. Traditionally, birefringent phase-matching (BPM) has been used to obtain efficient frequency conversion. However, there are drawbacks with this method. For example, there are limitations of the spectral range that can be covered, the elliptical form of the converted output beam caused by the beam walk-off is not ideal, and the lower nonlinear optical coefficient, *d,* used in this scheme is detrimental. The quasi-phase-matching (QPM) technique, on the other hand, has many attractive advantages compared with BPM. In the QPM-method, phase-matching between the incident beam and the converted beam are carried out by periodically modulating the sign of the non-linear optical coefficient, *d,* for each coherence length along the crystal. QPM makes it possible to employ the highest non-linear optical coefficients, *d*, in order to convert over the whole transmission spectrum of the crystal, normally from the UV to the IR by simply adjusting the periodicity of the spontaneous polarization, and to generate a circular beam by non-critical phase-matching. To realize the required modulation of the nonlinearity, ferroelectric domain reversal is used. To obtain such a structure, several methods have been developed for surface modulation, such as ion-diffusion and exchange on the c- face of the ferroelectrics as demonstrated in the early 1990s.6, 7) However, with the development of the electric-field poling, first demonstrated with $LiNbO_3$ in 1993,8) the fabrication of bulk, periodically-poled (PP) crystals became possible. Such structures have since then been intensively investigated and the field of nonlinear optical frequency conversion using the QPM-method has been widely spread.

The most intensively investigated material for PP structures is the conventional congruent $LiNbO_3$ because of its superior homogeneity and common availability. After a deeper understanding of its properties have been obtained, the limitations of congruent $LiNbO_3$ have also become clear. The first issue is its optical damage problem such as a low damage threshold for photorefraction. This limits its practical applications only to the infrared region or at high temperature operation at more than 100°C.9) The second limitation is its high coercive field (approximately 21 kV/mm) for switching of the spontaneous polarization, which makes it difficult to fabricate PP structures in samples thicker than 0.5 mm.10)

To overcome these limitations, several different new material candidates have been actively investigated. Mainly, there are three promising material groups. One is $LiNbO_3$ and $LiTaO_3$ doped with MgO or grown with a stoichiometric composition. The second one is $KTiOPO_4$ and its isomorphs. The third group consists of perovskite structures such as $KNbO_3$. In all of these three material groups, polarization switching by electric-field poling have been demonstrated and PP structures were fabricated around the mid or late 1990s.[11-13)]

Generally speaking, key factors when discussing the properties of nonlinear optical materials can be summarized in at least the following 10 points: 1) phase-matching condition, 2) transmission range, 3) optical nonlinearity, 4) homogeneity of the material, 5) damages of the chemical bond by an optical beam, 6) mechanical properties such as growth, polishing, and coating, 7) thermal properties such as refractive index dispersion and thermal conductivity, 8) lifetime, which is related to the chemical stability, hygroscopy, and aging, 9) optical damage properties such as the photorefractive damage and the photochromic effect (gray-tracking), and 10) availability of material with proper size, cost and uniformity. In this work, detailed focus has been put on the three most important properties of the PP materials: a) the optical damage properties, b) crystal homogeneity and availability, and c) the possibility of periodic poling.

There are two important optical damage types in ferroelectrics: photorefraction and gray tracking. Photorefractive damage can be obtained when shining a high intensity laser beam into a ferroelectric crystal. A small part of the radiation is absorbed creating an electron-ion pair and the electron is drifting out of the illuminated region driven by the inherent ferroelectric field. This sets up an electric field in the opposite direction which, in turn, will change the refractive index of the crystal. Gray tracking can be found when a high intensity laser beam is launched through the material and additional color centers are created inside the crystal. These color centers will absorb the incident and/or the converted beam. As a result, in both cases, the stability of the nonlinear frequency conversion process is deteriorated. $LiNbO_3$ has the highest nonlinear conversion efficiency among these three groups discussed above, but conventional congruent $LiNbO_3$ has a definite problem with a low threshold for photorefractive damages. To overcome this problem, MgO-doped congruent $LiNbO_3$ has been investigated; however, its homogeneity is still not perfect because of the necessary large amount of doping employed (5 mol%).[14)] The other approach is to fabricate a stoichiometric composition. Stoichiometric $LiNbO_3$ has been investigated and a relatively high resistance against photorefractive damages with 1 mol% MgO doping has been demonstrated.[15)] In the same group of crystals, $LiTaO_3$ is also an attractive material. Although the nonlinear conversion efficiency of $LiTaO_3$ is not so high compared with $LiNbO_3$, its higher threshold for photorefractive damages has made it very attractive presently.[16)] Particularly, as compared with $LiNbO_3$, stoichiometric $LiTaO_3$ with and without MgO doping, have been reported as having a much higher photorefractive damage threshold than the conventional congruent one. $KTiOPO_4$ and its isomorphs also have relatively high nonlinear conversion efficiency and display a higher resistance for photorefraction.[17)] All of these isomorphs, though, have gray-tracking problems at high power operation. Finally, $KNbO_3$ also has a relatively high nonlinear conversion efficiency and a quite high resistance for both photorefraction and gray-tracking.[18)]

From the point of view of the availability of the crystals, which, in turn, is strongly related to the crystal-growth method, each crystal group has its own problems. For the $LiNbO_3$ group, a double-crucible Czochralski (DC-CZ) method has been developed for stoichiometric $LiNbO_3$ and $LiTaO_3$, and crystal sizes have become available up to 2 to 3 inches in diameter.[19)] As described above, doping with MgO is necessary in order to improve the photorefractive damage properties. The control of the homogeneity is still an issue and continual development is ongoing. $KTiOPO_4$ and its isomorphs are primarily grown by the flux-grown method.[20)] Since these crystals are grown inside a melt in platinum crucibles, the sizes are limited up to approximately 1 inch in diameter. In addition, since the growth condition is difficult to control, the crystal homogeneity is varying to some extent from growth to growth, and especially the K^+ ion vacancy is changing, which will influence the optical and physical properties. $KNbO_3$, in turn, is grown by the top-seeded solution growth (TSSG) method.[21)] Although this crystal is grown with an almost stoichiometric composition, there is also in this case a limitation of the sizes of up to 1 inch in diameter because of its two phase transitions when cooling the crystal down to room temperature. In addition, since this material has several types of ferroelectric domain structures, there are some difficulties in obtaining large single-domain crystals and in the handling of the material.

From the point of view of obtaining periodic poling, the materials which have lower coercive electric fields for spontaneous polarization switching, lower conductivity, and good homogeneity of the crystals are preferable in order to get easier controllability of the periodic poling. Their domain morphology is also an important issue. For the $LiNbO_3$ and the $LiTaO_3$ groups, non-doped congruent ones have a very high coercive field and the domain morphology is triangular or hexagonal.22) Furthermore, a higher ionic conductivity is reported in MgO-doped materials. On the contrary, stoichiometric crystals, fortunately, have very low threshold fields (less than 4 kV/mm). The domain morphology, though, is still hexagonal which makes it rather difficult to obtain straight domain walls. In the case of $KTiOPO_4$ and its isomorphs, they have a relatively low coercive field (between 1 to 6 kV/mm) but the ionic conductivity is inconveniently high and inhomogeneously distributed throughout the as-grown crystals.11) $KNbO_3$ has a very low coercive field (less than 500 V/mm) and, also, has a low ionic conductivity.13) The latter two groups tend to provide rectangular domain morphology and it is rather easy to get straight domain walls.

As can be seen in many reports on these new material candidates, the spontaneous polarization switching properties and the optical damage properties are still not perfectly understood. One of the most obvious reasons for this is that there are still no commercial suppliers that can deliver crystals with high enough homogeneity and reproducible quality, similar to that of the conventional congruent $LiNbO_3$. Thus, comparisons between these crystals have not yet been investigated at the same levels as the earlier ones, both with regards to the spontaneous polarization switching properties and the optical properties. As can be noted, there are no particular reports of the effects of PP structures on the optical damage properties for these promising materials.

With regards to the above given background, the overall aim of the present project has been to find more suitable nonlinear optical materials that can be periodically-poled and designed and functioning for specific applications. Furthermore, an overall goal of the work is to get a deeper understanding of the spontaneous polarization switching process and the optical damage of the promising new ferroelectric materials. In this research work, the following materials have been investigated: a) DC-CZ grown 1 mol% MgO-doped stoichiometric $LiNbO_3$, b) 1 mol% MgO-doped stoichiometric $LiTaO_3$, c) non-doped stoichiometric $LiTaO_3$, d) flux-grown $KTiOPO_4$ and its isomorphs such as $RbTiOPO_4$, e) TSSG grown $KNbO_3$. The study has a main focus on three points. The first one is the spontaneous polarization switching characterization, the second point is the development of periodic-poling techniques and the last point is a comparison of the optical damage properties in both bulk and periodically-poled ferroelectric crystals. Throughout these investigations, I have tried to explore the many important physical properties of these materials.

1.2. Outline of this thesis

The thesis is composed as follows. Chapter 2 is a general introduction to the theory of nonlinear optics and to the quasi-phase-matching technique. In Chapter 3, the general properties of the investigated nonlinear ferroelectric materials are described. Especially, since I have worked at the crystal-growth division of a commercial company, the crystal growth and its related processes are described in detail. In addition, the optical properties of these materials as found in previously reported studies are described and compared for all of the chosen material candidates. In Chapter 4, I discuss the spontaneous polarization switching characterization of these ferroelectrics. Especially, the key material properties relevant for periodic poling (such as spontaneous polarization, conductivity, coercive field, and domain morphology), as based on our own experimental results, are described in detail. In Chapter 5, the process of optimizing the periodic poling conditions of the investigated materials are described together with some process improvement techniques for each material. In Chapter 6, finally, the properties of the optical damage both in unpoled and fabricated PP devices are discussed. Our method is based on monitoring the blue-light induced infrared absorption, which is a highly sensitive characterization method for photochromic damage. The important point here is that, since these experiments are carried out in the same set-up, it is possible to make a realistic comparison between the materials. In the last chapter, I summarize the content of this thesis and indicate some future prospects for the new materials.

References in Chapter 1

1) For example: K. Mizuuchi, A. Morikawa, T. Sugita, and K. Yamamoto: Jpn. J. Appl. Phys. **42**, L90 (2003).

2) For example: S. Johansson, S. Wang, V. Pasiskevicius, F. Laurell: Opt. Exp. **12**, 4935 (2004).

3) For example: T. Suhara, H. Ishizuki, M. Fujimura, and H. Nishimura: IEEE Photon. Tech. Lett. **11**, 1027 (1999).

4) For example: S. J. B. Yoo: J. Lightwave Tech. **14**, 955 (1996).

5) For example: A. Fragemann, V. Pasiskevicius, G. Karlsson, F. Laurell: Opt. Exp. **11**, 1297 (2003).

6) J. Webjörn, F. Laurell, and G. Arvidsson: J. Lightwave Tech. **7**, 1597 (1989).

7) K. Mizuuchi, K. Yamamoto, and H. Sato: J. Appl. Phys. **75**, 1311 (1994).

8) M. Yamada, N. Nada, M. Saitoh, and K. Watanabe: Appl. Phys. Lett. **62**, 435 (1993).

9) For example: T. Andres, P. Haag, S. Zelt, J.-P. Meyn, A. Borsutzky, R. Beogang, and R. Wallenstein: Appl. Phys. B **76** , 241 (2003).

10) G.. D. Miller: 'Periodically poled lithium niobate: Modeling, fabrication, and nonlinear-optical performance', Ph. D thesis, Stanford University, (1998).

11) H. Karlsson and F. Laurell: Appl. Phys. Lett. **71**, 3474 (1997).

12) J.-P. Meyn, M. E. Klein, D. Woll, R. Wallenstein, and D. Rytz: Opt. Lett. **24**, 1154 (1999).

13) T. Hatanaka, K. Nakamura, T. Taniuchi, H. Ito, Y. Furukawa, and K. Kitamura: Opt. Lett. **25**, 651 (2000).

14) B. C. Grabmaier, W. Wersing, and W. Koestler: J. Cryst. Growth **110**, 339 (1991).

15) K. Kitamura, Y. Furukawa, S. Takekawa, T. Hatanaka, H. Ito, and V. Gopalan: Ferroelectrics **257**, 235 (2001).

16) Y. Furukawa, K. Kitamura, A. Alexandrovski, R. K. Route, M. M. Fejer, and G. Foulon: Appl. Phys. Lett. **78**, 1970 (2001).

17) S. Wang, V. Pasiskevicius, and F. Laurell: J. Appl Phys. **96**, 2023 (2004).

18) U. Ellenberger, R. Weber, J. E. Balmer, B. Zysset, D. Ellgehausen, and G. J. Mizell: Appl. Opt. **31**, 7563 (1992).

19) K. Kitamura, J. K. Yamamoto, N. Iyi, and T. Hayashi: J. Cryst. Growth **116**, 327 (1997).

20) K. Iliev, P. Peshev, V. Nikolov, and I. Koseva: J. Cryst. Growth, **100**, 225 (1990).

21) T. Fukuda and Y. Uematsu: Jpn. J. Appl. Phys. 11, 163 (1992).

22) V. Gopalan, N. Sanford, J. A. Aust, K. Kitamura and Y. Furukawa: "Handbook of Advanced Electronic and Photonic Materials" edited by H. S. Nalwa, Academic Press (Oct. 2001) p. 62

Chapter 2. Basic principles of nonlinear optics

2.1. Introduction

In this chapter, the basic principles of nonlinear optics are described and the theoretical features of the quasi-phase-matching (QPM) process are introduced, which is one of the main topics in this thesis. In Section 2.2, the nonlinear polarization in the electromagnetic wave-equation is developed. Section 2.3 is focused on the second-order nonlinear interaction and the nonlinear optical coefficients (the ***d***-matrix) are introduced. In Section 2.4, the coupled wave equations are described, which are the basic equations for calculating energy transfer and the phase-matching conditions. Finally, the phase-matching process is explained in Section 2.5. The differences between the two different phase-matching processes [birefringent phase matching (BPM) and quasi-phase matching (QPM)] are described and the typical merits and drawbacks in both processes are discussed.

2.2. The nonlinear polarization 1)

When an electromagnetic wave passes through a dielectric material, it induces an electrical polarization inside the material, i.e., a displacement of the valance electrons from their stationary orbits. The induced polarization can be expressed as a function of the applied electric field:

$$P = \varepsilon_0 \chi^{(1)} E_1 + \varepsilon_0 (\chi^{(2)} E_1 E_2 + \chi^{(3)} E_1 E_2 E_3 + \cdots\cdots) = P^L + P^{NL}, \qquad (2.1)$$

where ε_0 is the permittivity of the vacuum, E_i is the i^{th} electric field component of the electromagnetic wave, and $\chi^{(m)}$ represents the susceptibility tensor of m:th order with the rank of (*m*+*1*). $P^L \equiv \varepsilon_0 \chi^{(1)} E_1$ corresponds to the linear part of the polarization and $P^{NL} \equiv \varepsilon_0 (\chi^{(2)} E_1 E_2 + \chi^{(3)} E_1 E_2 E_3 + \cdots\cdots)$ to the nonlinear part. The differences between P^L and P^{NL} are clearly seen in Fig. 2-2-1. When the irradiating electric field is small enough, the generated

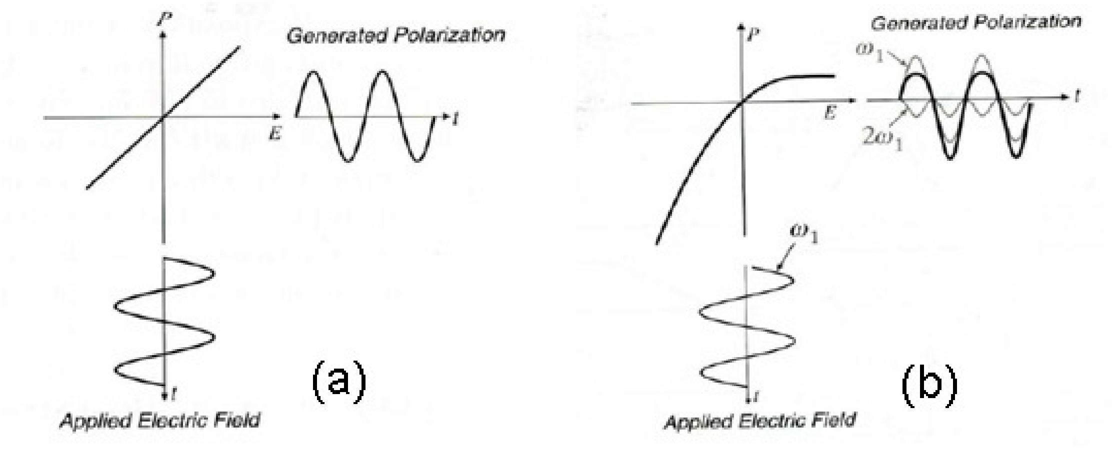

Figure 2-2-1. The differences between linear and nonlinear induced polarization: (a) Linear dependence holds for a low input field. (b) Non-linear induced polarization by inputting a high electric field. In the figure is shown the generated polarization of the second-harmonic of the applied frequency as an example of a nonlinear process. 1)

polarization is proportional to the applied electric field. On the other hand, when the irradiated electric field is high enough, the induced polarization is no more linear and will induce other frequency signals. From now on, we will focus on the P^{NL} effects.

2.3. Second-order nonlinear process and the d-coefficients

The most common process of nonlinear optics is the second-order process described by the expression: $P^2(\omega_3) \equiv \varepsilon_0 \chi^{(2)} E_1(\omega_1) E_2(\omega_2)$. Figure 2-3-1 shows the schematics of two different types of second-order processes. The first case, two input photons, which travel through the nonlinear medium, are either added or subtracted into one photon of either higher or lower energy, respectively, viz: $\omega_3 = \omega_1 \pm \omega_2$. For sum-frequency generation (SFG), the photon energies are added to create a new photon with higher energy, $\omega_3 = \omega_1 + \omega_2$. SHG is a special case of SFG when the two photons have the same frequency coming, for example, from the same laser mode, i.e., $\omega_1 = \omega_2 = \omega$, and $\omega_3 = 2\omega$. For difference-frequency generation (DFG), a photon with lower energy is created by subtraction of the lower energy from the higher, i.e., $\omega_3 = \omega_1 - \omega_2$.

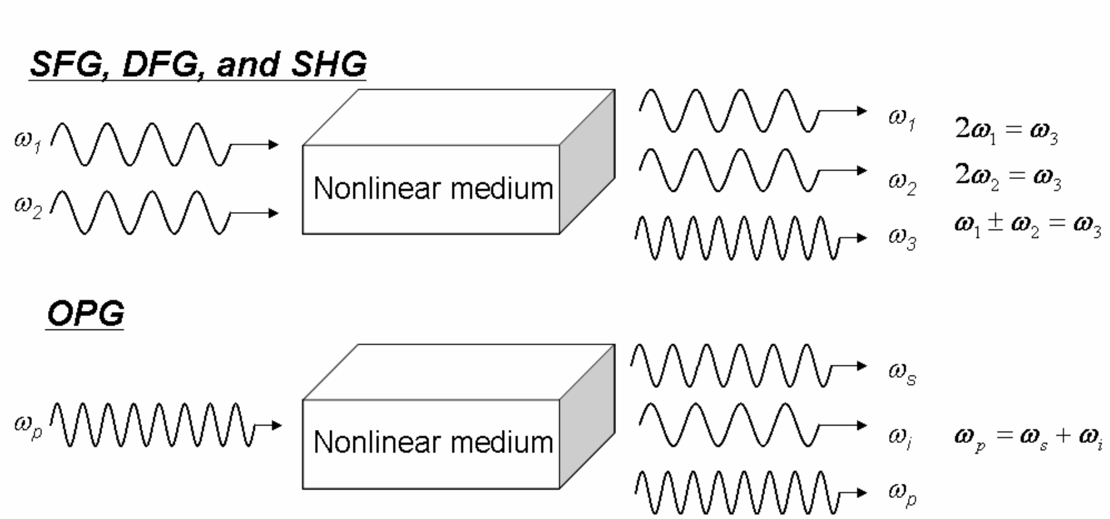

Figure 2-3-1. Frequency conversion processes in a second-order nonlinear medium.

The second case is called optical-parametric generation (OPG). In this process, a pump photon with frequency ω_p is split into two lower energy photons, called the signal photon with frequency ω_s and the idler photon with frequency ω_i, respectively, to keep the energy conservation, $\omega_p = \omega_s + \omega_i$. If the OPG is put into a resonator, an optical parametric oscillator is constructed.

Second-order nonlinear processes can only happen in materials without inversion center. In practice, the nonlinear ***d***-tensor has been commonly used instead of the $\chi^{(2)}$ tensor. The relationship between ***d*** and $\chi^{(2)}$ is given by the following expression:

$$d_{ijk} \equiv \frac{1}{2} \chi^{(2)}_{ijk} \quad , \qquad \text{(2-2)}$$

where *i, j*, and *k* are the Cartesian indices of the different frequency components. Because of the symmetry of this tensor, the components commute as follows, $d_{ijk} = d_{ikj}$, and a contracted notation is introduced where *j* and *k* are replaced by the index *l* as follows:

jk:	11	22	33	23, 32	13, 31	12, 21
l:	1	2	3	4	5	6

. (2-3)

By using the above notations, the second-order polarization in ***d***-matrix notation is given by

$$\begin{pmatrix} (P_{w_3}{}^{(2)})_x \\ (P_{w_3}{}^{(2)})_y \\ (P_{w_3}{}^{(2)})_z \end{pmatrix} = 2\varepsilon_0 K \begin{bmatrix} d_{11} & d_{12} & d_{13} & d_{14} & d_{15} & d_{16} \\ d_{21} & d_{22} & d_{23} & d_{24} & d_{25} & d_{26} \\ d_{31} & d_{32} & d_{33} & d_{34} & d_{35} & d_{36} \end{bmatrix} \begin{pmatrix} (E_{w_1})_x (E_{w_2})_x \\ (E_{w_1})_y (E_{w_2})_y \\ (E_{w_1})_z (E_{w_2})_z \\ (E_{w_1})_y (E_{w_2})_z + (E_{w_1})_z (E_{w_2})_y \\ (E_{w_1})_x (E_{w_2})_z + (E_{w_1})_z (E_{w_2})_x \\ (E_{w_1})_x (E_{w_2})_y + (E_{w_1})_y (E_{w_2})_x \end{pmatrix} , \qquad (2\text{-}4)$$

where $K = K(-\omega_3;\ \omega_1,\ \omega_2)$ is the degeneracy factor which takes on the value 1/2 for $\omega_1 = \omega_2$ and the value 1 for $\omega_1 \neq \omega_2$, respectively.

2.4. The coupled wave equations

The propagation of all electromagnetic fields is governed by Maxwell's equations. In the case of propagation in dielectric media, which do not have any free charges and negligible magnetic permeability, the Maxwell's equations are then reduced to the following equation:$^{1)}$

$$\nabla \times \nabla \times E = -\mu_0 \varepsilon_0 \frac{\partial^2 E}{\partial t^2} - \mu_0 \frac{\partial^2}{\partial t^2} P \ , \qquad (2\text{-}5)$$

where μ_0 is the permeability of vacuum. Using the vector relation $\nabla \times \nabla \times E \equiv \nabla(\nabla E) - \nabla^2 E$, neglecting static polarization $\nabla D = 0$, where D is given by $D = \varepsilon_0 E + P$, and using the definition of induced polarization P given by Eq. (2.1), Eq. (2-5) changes into the form given by:

$$\nabla^2 E - \varepsilon_0 \mu_0 (1 + \chi^{(1)}) \frac{\partial^2 E}{\partial t^2} = \mu_0 \frac{\partial^2 P^{NL}}{\partial t^2} \ . \qquad (2\text{-}6)$$

To solve this equation analytically, several assumptions can be made to simplify the solution. First, let the electromagnetic waves be quasi-monochromatic plane-waves and propagate along the *x*-axis. The electric field and the polarization can then be written as:

$$E(x,t) = \frac{1}{2}[E(x,\omega) e^{i(\omega t - kx)}] + c.c.,$$

and (2-7)

$$P(x,t) = \frac{1}{2}[P(x,\omega) e^{i(\omega t - kx)}] + c.c.,$$

where *k* is the wave-vector. It is defined, together with the refractive index *n,* at frequency ω, and with the speed of light *c,* by the following equations:

$$k = \frac{n\omega}{c}, \qquad n = \sqrt{\frac{\varepsilon(\omega)}{\varepsilon}} \; . \tag{2-8}$$

Here it is also assumed that the envelope of the plane-waves changes slowly with the distance. Then, the second-order derivatives with respect to distance and time can be neglected. This is called the slowly-varying envelope approximation, or SVEA:[2)]

$$\begin{aligned}
&\left|\frac{\partial^2 E(x,\omega)}{\partial x^2}\right| << \left|k\frac{\partial E(x,\omega)}{\partial x}\right| \\
&\left|\frac{\partial^2 E(x,\omega)}{\partial t^2}\right| << \left|\omega\frac{\partial E(x,\omega)}{\partial t}\right| \qquad . \\
&\left|\frac{\partial^2 P(x,\omega)}{\partial t^2}\right| << \left|\omega\frac{\partial P(x,\omega)}{\partial t}\right| << \omega^2 P(x,\omega)
\end{aligned} \tag{2-9}$$

By inserting Eq. (2-7) into Eq. (2-6), and taking SVEA into account, Eq. (2-6) can be simplified to a first-order differential equation;

$$\frac{\partial E}{\partial x} = \frac{i\mu_0 c\omega}{2n} P^{NL} \qquad . \tag{2-10}$$

For second-order nonlinear processes, all of the fields mix with all of the other and the three waves will couple to each other through the three polarizations, yielding three coupled-wave equations as follows:

$$\begin{aligned}
&\frac{\partial E_1}{\partial x} = \frac{i\omega_1^2}{n_1 c} K d_{eff} E_3 E_2^* e^{i(k_3-k_2-k_1)x} \qquad , \\
&\frac{\partial E_2}{\partial x} = \frac{i\omega_2^2}{k_2 c^2} K d_{eff} E_3 E_1^* e^{i(k_3-k_2-k_1)x} \qquad , \\
&\frac{\partial E_3}{\partial x} = \frac{i\omega_3^2}{k_3 c^2} K d_{eff} E_1 E_2 e^{-i(k_3-k_2-k_1)x} \qquad .
\end{aligned} \tag{2-11}$$

The frequency relation of the interacting waves obeys the expression $\omega_3 = \omega_1 + \omega_2$, and the phase-mismatch between them is given by $\Delta k = k_3 - k_2 - k_1$. The effective nonlinear coefficient, originating from the ***d***-matrix as given in Eq. (2-4), is now modified with a factor for the relevant phase-matching condition. The nonlinear interaction is maximized when $\Delta k = 0$, which can be achieved by properly choosing the direction of propagation of the interacting waves.

2.5. Phase-matching process

In order to obtain useful output power of the frequency-converted light, the phase-mismatch among the three interacting waves, Δk, should be equal to zero as noted above. For easy understanding, consider the optimized phase-matching ($\Delta k = 0$) and the arbitrary phase-mismatch ($\Delta k \neq 0$) conditions for the SHG, where the phase velocities of the fundamental and the second harmonic waves are given by $c/n(\omega)$ and $c/n(2\omega)$, respectively. The intensities of the SHG signal in both cases are illustrated in Fig. 2-5-1. When $\Delta k \neq 0$, the driving polarization and the generated field will drift out-of-phase relative to each other. Thus, the efficiency of the interaction is strongly reduced as the energy is transferred from the fundamental wave to the generated wave, and then back to the fundamental wave again while they propagate through the nonlinear medium as shown in curve c of Fig. 2-5-1. The distance over which the maximum transfer of the energy occurs between the fundamental wave and the generated wave is called the coherence length of the interaction; it is defined for a given phase-mismatch Δk by:

$$L_c = \left| \frac{\pi}{\Delta k} \right| \quad . \tag{2-12}$$

On the other hand, when $\Delta k = 0$, the interaction is phase-matched and the contributions to the second-harmonic wave generated at each point along the nonlinear material add up in phase with the contributions generated at every other point along the crystal, thus, the second-harmonic field grows linearly with distance in the crystal and its intensity grows quadratically as shown in curve a in Fig. 2-5-1.

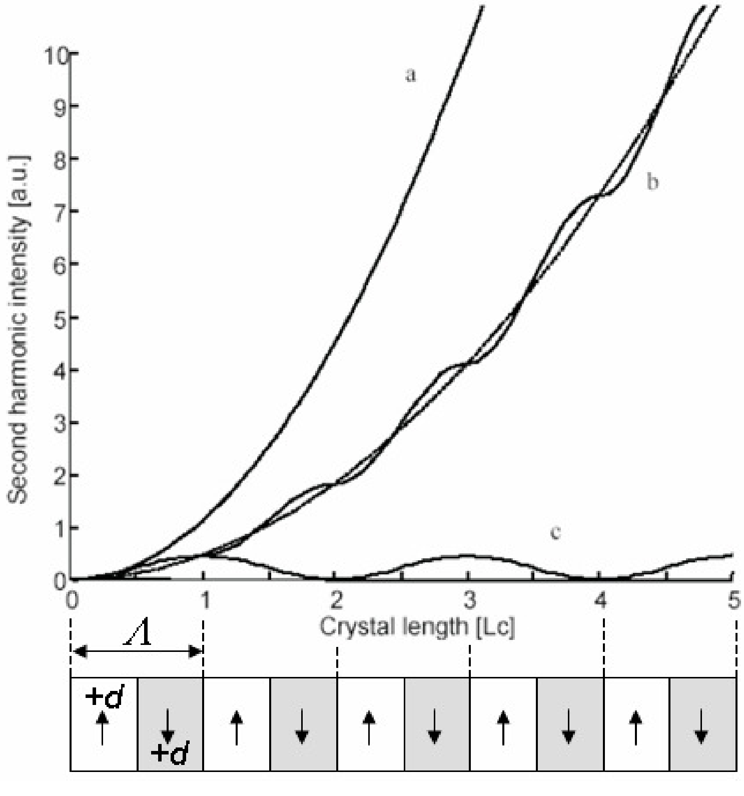

Figure 2-5-1. Second harmonic generation in a material with different phase matching conditions. Line (a): perfect phase matching, (b): the first order QPM by flipping the sign of the nonlinear coefficient every coherence length of the interaction of curve (c), (c): non-phase matched interaction.[2] *The bottom figure is the corresponding first order QPM structure.*[3]

There are two important techniques employed to satisfy the phase matching condition. One is termed birefringent phase-matching (BPM), as shown in curve a, and the other is called quasi-phase matching (QPM), as shown in curve b in Fig. 2-5-1.[3]

2.5.1. Birefringent phase-matching (BPM)

Since the refractive index of a nonlinear material has dispersion, the phase-matching condition $\Delta k = 0$ is not often satisfied by itself. But, by using the natural birefringence of the material, it is possible to meet the phase-matching condition. This situation depends on the material constants itself. Referring now to a three-wave nonlinear process, there are two main types of BPM. The type I BPM is the case when the fields of the incident beam, at frequencies ω_1 and ω_2, have the same polarization and the field of the converted beam, at frequency ω_3, has an orthogonal polarization. The type II BPM is defined as when the fields at ω_1 and ω_2 are orthogonally polarized with respect to each other.

In general, since one of the fields at any of the frequencies ω_1, ω_2, or ω_3 are often subject to what is commonly called the Poynting-vector walk-off in BPM, the angular tolerances of the incident beam is very narrow, therefore, it is also called 'critical phase matching' (CPM). In the special case when all of the fields propagate along the dielectric tensor axis, the angular tolerances of the incident beam are not critical, therefore, it is called 'non-critical phase-matching' (NCPM). Since the NCPM condition is determined by the refractive index dispersion, $n(\lambda)$, it is, generally speaking, not possible to control it without changing the material parameters.

Since the BPM technique is achieved by simply orienting the crystal properly during cutting and polishing, it is commonly applied in industrial applications such as visible-light generation in a multitude of applications. However, there are many limitations of this technique mainly due to the Poynting-vector walk-off, as mentioned briefly above. For example, the converted beam shape becomes elliptical because of the material birefringence; also the interaction length is limited. The other main disadvantage is that it is impossible to employ the d_{11}, d_{22}, or d_{33} tensor components because, at least one polarization of the field, should be orthogonal to the others in BPM. Since the diagonal component of many nonlinear optical materials is the largest one, this is one of the biggest disadvantages of BPM in comparison with QPM.

2.5.2. Quasi-phase matching (QPM)

QPM is an attractive alternative technique to birefringent phase-matching for compensating the phase-velocity dispersion in the case of frequency conversion applications, such as SHG and, thus, achieving efficient energy transfer among the interacting waves.

Armstrong et al.$^{4)}$ introduced the concept of QPM already in 1962. For a frequency conversion process, the phase-mismatch is accumulating with an increasing interaction length. After one coherence length, L_C, the conversion efficiency decreases as the energy flows back from the converted wave to the driving wave. If the nonlinear coefficient, d, is modulated with a period equal to twice the coherence length, meaning, in other words, that the nonlinear coefficient changes its sign after each coherence length, the accumulated phase-mismatch can be effectively offset. QPM achieves phase-matching through a artificially structuring of the nonlinear material rather than through its inherent birefringent properties. The periodic phase correction inherent in QPM causes the SH power to build-up in a stepwise fashion as shown in curve b in Fig. 2-5-1. The build-up process is less rapid than what would occur with BPM. Regardless of this reduced efficiency, there are many important advantages with QPM. First, it is possible to design the structure for any interacting frequencies within the transparency range of the material by periodically changing the sign of the nonlinear coefficient. Second, it is possible to design devices with the highest nonlinear coefficient under the non-critical phase-matching condition.

In order to achieve QPM, an artificially engineered +/− sign modulation of the nonlinear tensor d_{ijk} can be used. The nonlinear modulation can be described by a function, $g(x)$, which is a rectangular function with a period Λ and with a magnitude of +1 or −1. Then, $g(x)$ can be expressed by a Fourier expansion:[3)]

$$g(x) = \sum_{m=-\infty}^{\infty} G_m e^{iK_m x}\,, \tag{2.13}$$

where K_m is the magnitude of the m:th harmonic of the grating vector given by:

$$K_m = \frac{2\pi m}{\Lambda}\,, \tag{2.14}$$

and where G_m is the corresponding amplitude factor. The direction of the grating vector is along the propagation direction x of the electromagnetic waves.

The effective nonlinear coefficient, $d(x)$, can now be written as:

$$d(x) = d_{ijk}\, g(x)\,. \tag{2.15}$$

The power conversion will be quite efficient, even in the case of $\Delta k \neq 0$, if the following relationship is satisfied:

$$\Delta k_{total} = \Delta k - K_m = 0\,. \tag{2.16}$$

This equation is fulfilled for two conjugate terms in the series of $g(x)$. Thus, the effective nonlinear coefficient for QPM is reduced to $d_{eff} = G_m d_{ijk}$. For a rectangularly modulated structure with a duty-cycle of $D = L_p/L$, where L_p is the length of the grating that has a positive sign of its d_{ijk} and L is the total length of the structure, the coefficient G_m now takes on the values:

$$G_m = \frac{2}{\pi m}\sin(\pi m D)\,. \qquad (m = 1, 2, 3 \ldots.) \tag{2.17}$$

At the optimum value of D, i.e., a 50% duty-cycle, the sine function becomes 1 and d_{eff} is given by

$$d_{eff} = \frac{2}{\pi m} d_{ijk} \quad . \tag{2.18}$$

To realize this configuration, several types of structures have been demonstrated. The most common one is to create a device in which the spontaneous polarization direction each is one coherent length long, a so-called periodically-poled structure, which is the main focus of this thesis. The proper spatial period, Λ, is calculated by inserting Eq. (2.8) and (2.14) into Eq. (2.16):

$$\Lambda = \frac{m}{\frac{n_3}{\lambda_3} - \frac{n_2}{\lambda_2} - \frac{n_1}{\lambda_1}} \quad , \tag{2.19}$$

where n_1, n_2, and n_3 are the refractive indices corresponding to the wavelength λ_1, λ_2, and λ_3 of the interactive ways, respectively.

References in Chapter 2.

1) P. N. Butcher and D. Cotter: “The Elements of Nonlinear Optics”, Cambridge Studies in Modern Optics 9, Cambridge University Press, (1990)

2) M. M. Fejer, G. A. Magel, D. H. Jundt, and R. L. Byer: IEEE J. Quantum Electron. **28**, 2631 (1992).

3) L. E. Myers, R. C. Eckardt, M. M. Fejer, R. L. Byer, W. L. Bosenberg, and J. W. Pierce: J. Opt. Soc. Am. B **12**, 2105 (1995).

4) J. A. Armstrong, N. Bloembergen, J. Ducuing, and P. S. Pershan: Phys. Rev. **127**, 1918 (1962).

Chapter 3. Nonlinear optical ferroelectrics

3.1. Introduction

In this chapter, the basic material features of the investigated nonlinear optical ferroelectrics (stoichiometric $LiNbO_3$ and $LiTaO_3$, $KTiOPO_4$ and its isomorphs, and $KNbO_3$) are described. The issues in this chapter are divided in 2 parts: one is concerned with the material fabrication, and the other covers the relevant optical properties of these materials.

Before going into the details, the basics of ferroelectricity are described in the following section. Then, in Section 3.3, the materials are described from the point of view of crystal structure, crystal growth, phase transition, and post-growth processing. In Section 3.4, the optical properties of these materials are compared as based on previous reports. Especially, the nonlinear coefficient, ***d***, the figure of merit, the transparency range, and the damage properties are described. In addition, comparison of the QPM period for SHG is also given. The key ferroelectric properties which are related to the domain switching phenomena are described in the following chapter (Chapter 4).

3.2. Ferroelectric crystals

3.2.1. Crystal symmetry 1)

The response of anisotropic materials to the influence of an electric field is described by tensors whose properties are given by the point symmetry group of the crystal. According to Neumann's law, the crystal symmetry is given by a combination of point symmetry elements. There are 8 independent symmetry operations: rotation (1, 2, 3, 4, 6), mirror reflection (m), inversion ($\bar{1}$), and rotary inversion ($\bar{3}$, $\bar{4}$, $\bar{6}$). (The elements $\bar{3}$ and $\bar{6}$ are not independent, which are described by a combination of 3 and $\bar{1}$, and 3 and m, respectively.) The definition of the n^{th} rotation symmetry

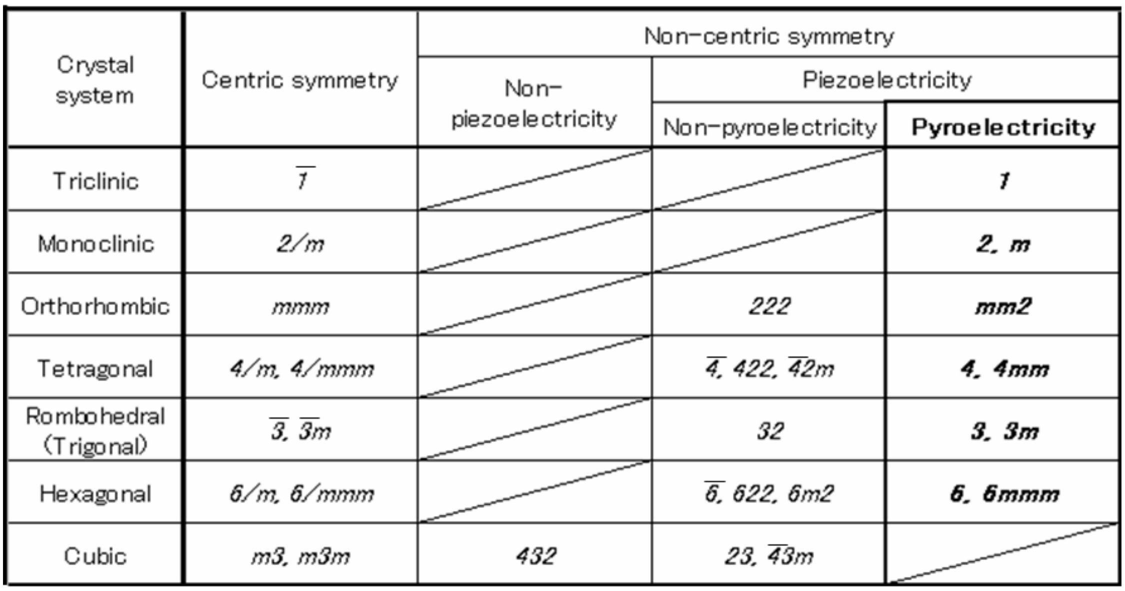

Crystal system	Centric symmetry	Non-centric symmetry		
		Non-piezoelectricity	Piezoelectricity	
			Non-pyroelectricity	**Pyroelectricity**
Triclinic	$\bar{1}$			**1**
Monoclinic	2/m			**2, m**
Orthorhombic	mmm		222	**mm2**
Tetragonal	4/m, 4/mmm		$\bar{4}$, 422, $\bar{4}2m$	**4, 4mm**
Rombohedral (Trigonal)	$\bar{3}$, $\bar{3}m$		32	**3, 3m**
Hexagonal	6/m, 6/mmm		$\bar{6}$, 622, 6m2	**6, 6mmm**
Cubic	m3, m3m	432	23, $\bar{4}3m$	

Table 3-2-1. Material symmetry.

is the resulting structure which is symmetric after rotating an angle of $2\pi/n$. All of the crystals are divided into 32 groups by the combination of these symmetry elements. These are classified in Table 3-2-1 from the point of view of the crystal system and centric symmetric, which is symmetric with respect to the center point of the lattice, or non-centric symmetry, which is not symmetric with respect to the center point of the lattice.

3.2.2. Piezoelectricity 1)

As shown in Table 3-2-1, the crystals which have non-centric symmetric structure have piezoelectric properties except for one group. Piezoelectricity is a phenomenon in which an electrical polarization is generated inside a crystal when a mechanical stress is applied to it and vice versa. The relationship between the induced polarization, P_i, and applied stress, X_{jk}, is given by:

$$P_i = d_{ijk} X_{jk} \quad , \qquad (3.1)$$

where d_{ijk} is a third-rank tensor called the piezoelectric coefficient tensor. The piezoelectric coefficients should not be confused with the second-order nonlinear optical coefficient matrix which is designated by the same letter ***d***. The most popular example of a piezoelectric material, which does not show pyroelectricity (see below), is quartz which belongs to the point group '*32*'.

3.2.3. Spontaneous polarization, pyroelectricity, and ferroelectrics 1-2)

Some piezoelectric materials also have a spontaneous polarization, P_s, which represents a non-zero macroscopic dipole moment existing inside the crystal without any externally applied electric field or stress. The spontaneous polarization is caused by the displacement of the centers of the positive and the negative charges in the unit cell. If the displacement distance is l and the amount of charge per unit volume is given by ρ, the spontaneous polarization value is given by the expression:

$$P_s = \rho l \quad . \qquad (3.2)$$

In general, P_s is a function of temperature, T. When the temperature changes by an amount of ΔT, the change in the spontaneous polarization, ΔP, is given by:

$$\Delta P_i = p_i \Delta T, \ (i = 1,2,3) \quad , \qquad (3.3)$$

where p_i is the pyroelectric coefficient. This polarization change is called pyroelectricity. The point groups which have pyroelectric response are also shown in Table 3-2-1. In some of the pyroelectric materials, the direction of the spontaneous polarization can be switched around by applying an electric field. These materials are called ferroelectrics. The group of materials we call pyroelectrics is larger than, but includes, the ferroelectric group. When an electric field, E, is applied along the polar direction of the ferroelectric materials as shown in Fig. 3-2-1, a *P-E* hysteresis loop is obtained. The electric field, E_c, which is defined by the half-area of the spontaneous polarization switched, is called the coercive field. Generally, the E_c and P_s are decreasing when the temperature is increasing because of the pyroelectric effect. As mentioned regarding the pyroelectric effect, the spontaneous polarization in the pyroelectric effect is a function of temperature. When increasing the temperature, the amount of spontaneous polarization decreases and, finally, it reaches zero. This temperature is called the Curie temperature, T_c and it is of great importance in solid-state physics. The ferroelectric materials show their ferroelectricity at temperatures lower than T_c and they become para-electric at temperature above T_c. All of the nonlinear crystals that are investigated in this thesis are ferroelectrics at room temperature.

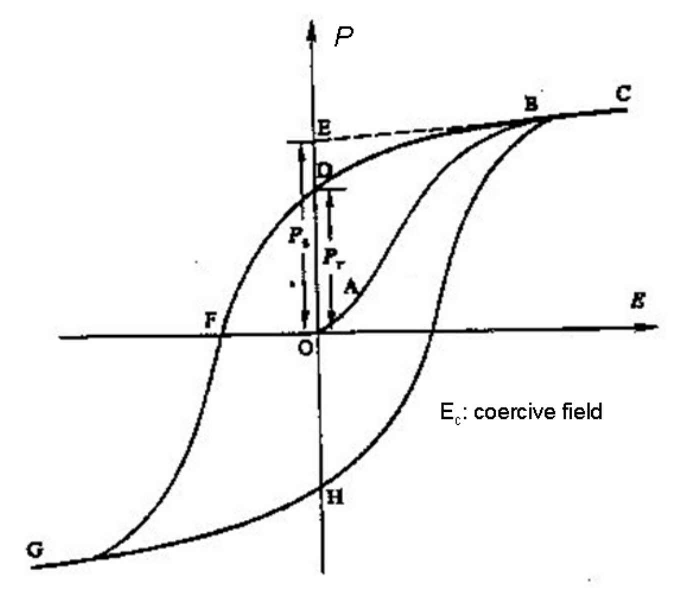

Figure 3-2-1. Ferroelectric P-E hysteresis loop.

3.3. Crystal growth

The material properties depend not only on the lattice structure but also on the basic crystal quality, e. g. concentration of vacancies, the variation of the stoichiometry, and inclusions. The latter two issues are strongly related to the technique of the crystal growth, which essentially determines the crystal composition and the concentration of the defects. In the case of periodic poling, the crystals are cut and polished in wafers in which the spontaneous polarization direction $\boldsymbol{P_s}$ in the material should be aligned in a single direction, the so-called single-domain wafers. In general, the $\boldsymbol{P_s}$-direction of the as-grown crystals is often randomly oriented in several possible directions in so-called multi-domain structures. Different methods exist in order to obtain single-domain crystals of which a common one is to apply an electric field between the seed and the melt during or after the growth. Here, the crystal growth methods and the poling treatment for each investigated material are described in detail in the ensuing sections.

3.3.1. $LiNbO_3$ and $LiTaO_3$

General features

$LiNbO_3$ (LN) and $LiTaO_3$ (LT) are rhombohedral crystals belonging to the point group 3m at room temperature. These crystals belong to the pseudo-ilumenite structures. The first fabrication of a synthetic $LiNbO_3$ crystal was done in 1949 by Mattias and Remeika3) by using a flux-growth method. After Ballman et al.4) succeeded in growing $LiNbO_3$ by the Czochralski (CZ) method, the material properties of both $LiNbO_3$ and $LiTaO_3$ have been studied intensively and it has been found that they have very high coefficients for both the piezoelectric and the optical properties. Because of the successively higher demands for both $LiNbO_3$ and $LiTaO_3$ for surface acoustic wave (SAW) devices, the growth techniques for them have been dramatically improved in the 1980s and the 1990s and they are now produced in up to 5-inch-diameter-wafers. CZ growth produces crystals of congruent composition which is not stoichiometric in the case of LN and LT. There are some basic limitations in the (conventional) congruent composition of $LiNbO_3$ (CLN) and $LiTaO_3$ (CLT) for optical applications, especially for use in the visible light region due to their inherently low threshold for optical-damage. CLN are thus primarily used for infra-red wavelengths, particularly in telecom and in sensor-waveguide applications. No outstanding optical applications have been forthcoming by using CLT. To alleviate the optical-damage problems, several approaches to modify the material composition have been investigated. The most common way is by doping MgO into CLN.5) The second most common technique has been to try to make stoichiometric composition crystals. Especially, stoichiometric-composition $LiNbO_3$ (SLN) and $LiTaO_3$ (SLT), are expected to have definite advantages in terms of better resistances to optical damages as well as a lower concentration of defects that reduce the coercive fields for the spontaneous polarization switching. 6-7)

The schematic of the lattice structures of $LiNbO_3$ or $LiTaO_3$ are shown in Fig. 3-3-1. These materials are paraelectric with the point group $\bar{3}m$ for temperatures above the Curie temperature, T_c, the value of which are approximately 1140°C and 601°C for $LiNbO_3$ and $LiTaO_3$, respectively.8-9) The mirror plane is the *X*-plane. Below the T_c, the Li^+ ions slightly shift to the $+Z$ direction away from the oxygen triangle and the Nb^{5+} or the Ta^{5+} ions also shift slightly in the $+Z$ direction from their respective center of the oxygen octahedron. These displacements are responsible for the spontaneous polarization effects, whose positive is directed along the +Z. The Curie temperature, T_c, increases when the compositions of the Li/Nb-ratio become close to the stoichiometric value or if the MgO concentration increases.

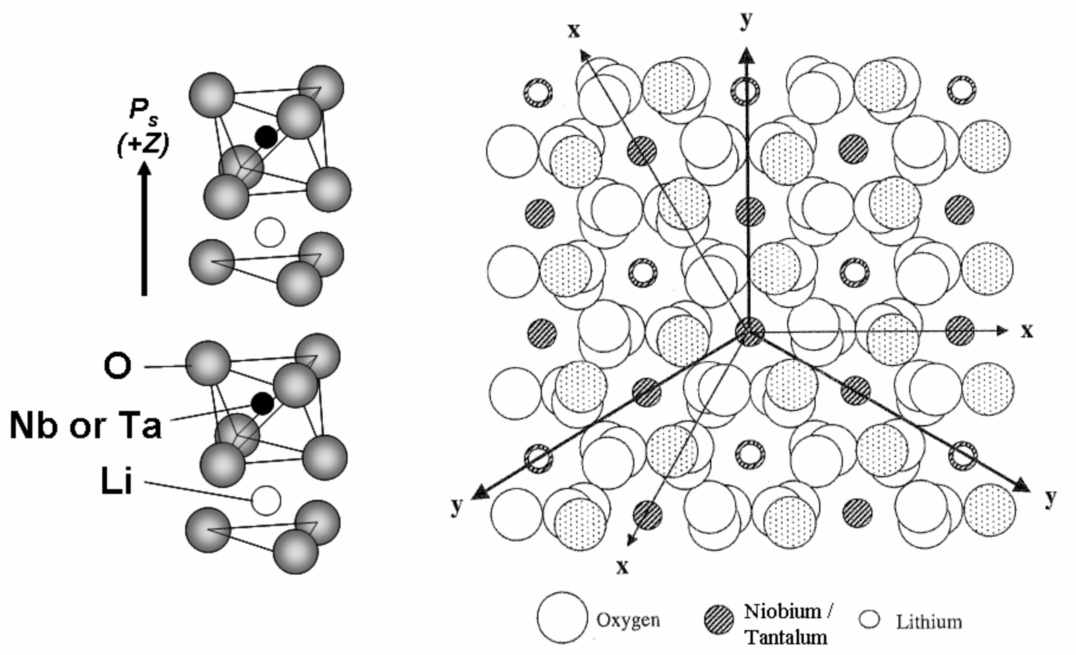

Figure 3-3-1. Schematics of the crystal structure of $LiNbO_3$ and $LiTaO_3$.

<u>*Crystal growth methods*</u>

Conventional congruent $LiNbO_3$ and $LiTaO_3$ are grown by the Czochralski (CZ) method. Typical growth procedures are shown in Fig. 3-3-2. Since the crystal is pulled during the growth process in the CZ method, it is possible to grow large-diameter and long-length crystals. Especially, by using an automatic diameter control (ADC) systems, the pulling process is almost automated, which tends to provide higher quality crystals.

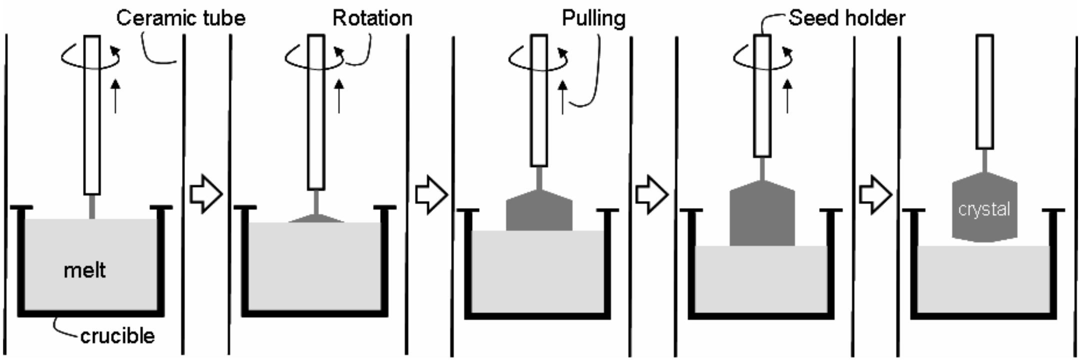

Figure 3-3-2. Schematics of a typical Czochralski (CZ) growth process.

An important question regarding the composition issue is what the term congruent crystals means. The phase diagram of the $LiNbO_3$ and $LiTaO_3$ materials are shown in Fig. 3-3-3.$^{10-11)}$ The congruent composition corresponds to the highest point on the melting temperature line. This composition is then approximately Li_2O:Nb_2O_5 or Li_2O:Ta_2O_5 $\approx$ 48.3 - 48.7 mol%: 51.7 - 51.3 mol%. When the melt of $LiNbO_3$ or $LiTaO_3$ are prepared with this composition, the composition of the whole grown crystal takes on this same (congruent) composition. If someone tries to grow a material from the off-congruent melt, the composition of the grown crystal would vary through the crystal, normally from top to bottom.$^{12-13)}$ The exact congruent composition depends on the growth system because of some slight the Li_2O out-diffusion which takes place during the growth process. According to Carruthers et al., the origin of the displacement from stoichiometry could be that the NbO_6 or TaO_6 octahedrons possess a substantial degree of covalency which makes it possible to accommodate the lithium vacancies at a small cost of energy.$^{10)}$

Since the ratio of Li:Nb or Li:Ta are not 1:1, there are many Li^+ vacancies in the congruent crystals. These vacancies will cause undesired effects in the optical properties; especially an increased photorefractive effect. One effort to overcome this is to dope MgO into the crystal to fill in the Li^+ vacancies. In the case of the congruent composition, the optimum MgO concentration has been found as high as 5 mol%.$^{8)}$ However, the growth of MgO-doped congruent material is associated with several difficulties such as relatively large amount of inhomogeneities and crystal twining because of the high MgO content.

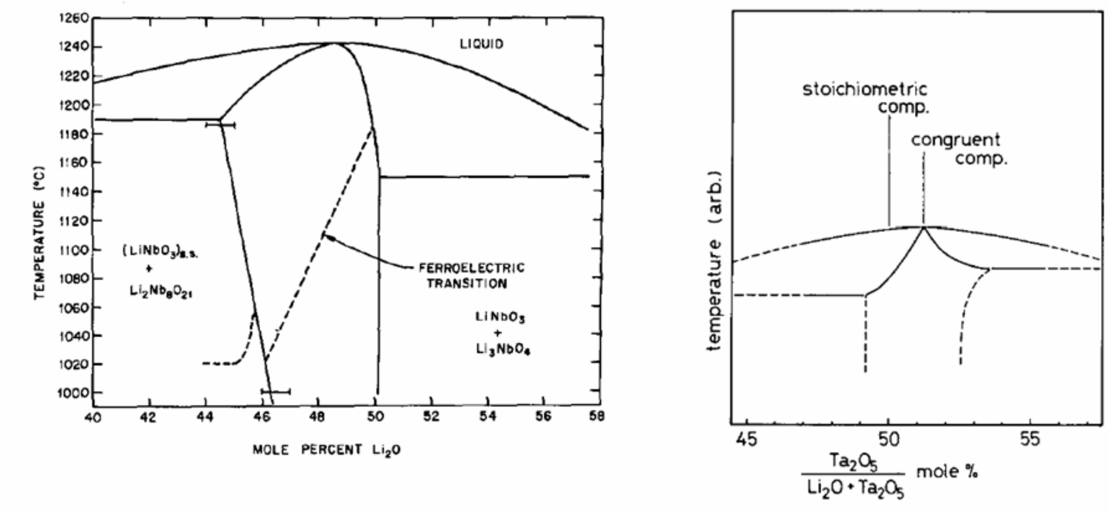

Figure 3-3-3. Phase diagram of $LiNbO_3$ (left) and $LiTaO_3$ (right).$^{10-11)}$

A second promising way in order to create a better crystal is to try to make a stoichiometric composition. Three different ways to achieve stoichiometric composition have been reported. The first one is by the vapor transport equilibration (VTE) technique.14) In this method, the congruent crystal wafer is heated in the presence of a Li_2O-rich mixture of powders heated to just below the melting point. As a result, Li^+ are diffusing into the wafer and a more Li rich composition is thus obtained. For long diffusion times, an almost stoichiometric composition is obtained. The second method is growing the crystal by using a K_2O flux.15) In this technique, the melt composition of Li:Nb equals about 1:1 and one only adds K_2O with more than 6 weight percents as a flux. In these two methods, however, mechanical twining has been reported to occur and that leads to crystals with poor quality.16)

The last method is the double-crucible Czochralski growth (DC-CZ) method.17) The schematics of this system are shown in Fig. 3-3-4. If the crystal is grown from the stoichiometric composition in the conventional CZ method, the composition of the melt is changing during crystal growth. In the DC-CZ method, however, powders consisting of a mixture of Li_2O and Nb_2O_5/Ta_2O_5 with almost stoichiometric composition are added into an outer crucible during the growing of the crystal. Thus, it is possible to keep almost the same melt composition during the whole process. Since this special technique is still a version of the general CZ method, the crystal is pulled out during the growth procedure in the usual way. Thus, it is possible to make a crystal with a large diameter and a long crystal length. Even when using the DC-CZ method, still the perfect stoichiometric composition crystal has not been obtained yet. However, *Z*-axis grown, near-stoichiometric $LiNbO_3$ with 49.8 mol% Li_2O concentration and *Z*-axis grown near-stoichiometric $LiTaO_3$ with more than 49.90 mol% Li_2O concentration have been demonstrated from a 58 mol% and 61 mol% Li_2O melt composition, respectively.18-19) Since Li^+ vacancies still exist in the crystals, and hence the material is photorefractive, additional MgO doping has also been demonstrated for near-stoichiometric composition crystals. MgO doping with concentrations higher than 1 mol% in both stoichiometric $LiNbO_3$ and $LiTaO_3$ have shown promising properties.20-21) Presently, 3-inch wafers of stoichiometric $LiNbO_3$ and 2-inch wafers of stoichiometric $LiTaO_3$ are available for commercial use. It is not obvious that stoichiometric composition is preferable for QPM due to the very low coercive fields, which makes crystal treatment and domain stabilization problematic.

Poling treatment

The poling treatment is performed for the as-grown crystal ingots in both congruent and stoichiometric $LiNbO_3$ and $LiTaO_3$. These ingots are clamped by a conductive powder-ceramics and an electric field is applied near the Curie temperature T_c. The poling technique is often a mixture of proprietary know-how and many special conditions that have been reported and patented. The typical conditions for the poling of congruent $LiNbO_3$, for example, are the application of E-fields of more than 0.2 V/mm at a temperature of approximately 1230°C maintained for 2 to 6 hours, and correspondingly for congruent $LiTaO_3$, approximately 1.5 V/mm at 605°C for 5 to 10 h. These cited conditions are critical because higher temperatures will strongly affect the compositions, particularly with regards to the Li^+ or O^{2-} contents. After the poling treatment, it is very important to avoid micro-domain formation, which can happen during the cutting or the polishing processes due to the pyroelectric effect and stress induced electric field through piezoelectric effect. Especially for stoichiometric materials, micro-domains are easily produced during heating or while cooling the samples in the wafer fabrication process. These micro-domains can cause disturbances of the periodic structure in the subsequent, periodically-poled processes and they have to be removed before the QPM fabrication.

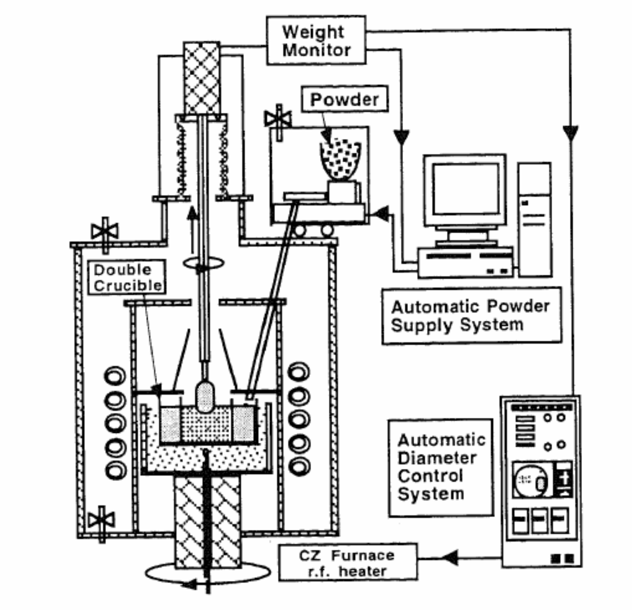

Figure 3-3-4. Schematic diagram of the double-crucible Czochralski method equipped with an automatic powder supply system.[17)]

3.3.2. $KTiOPO_4$ and its isomorphs

General features

$KTiOPO_4$ (KTP) was synthesized in 1890 for the first time.[22)] After that, it was almost forgotten until the 1970s. In 1976, researchers at the du Pont company in USA started to investigate its optical and mechanical properties.[23)] The material is an orthorhombic crystal belonging to the point group mm2 at room temperature. Its isomorphs $MTiOXO_4$, where M = K, Rb, or Tl, and X = P or As, also have the same orthorhombic structure.[24)] KTP melts at a temperature of approximately 1150°C, however it also decomposes itself at the same time. Thus, it is impossible to grow this crystal by the CZ method. In the early days, KTP was grown by the hydro-thermal growth method.[25)] Since this method requires a high-pressure and a high-temperature atmosphere, there is a high risk of exploding the autoclave. Presently, it is common to grow KTP by the flux-growth method. Commercially available sizes of single-domain crystal plates are up to 30 mm×30 mm. KTP and its isomorphs have relatively large nonlinear and electro-optic coefficients, and high photorefractive damage threshold. KTP is also one of the most commonly used materials for frequency doubling of 1.064 µm by using birefringent phase matching (BPM). Presently, it is also common to use periodically-poled KTP in commercial products.[26)] Its isomorphs have also been actively investigated, for instance, $RbTiOPO_4$, Rb-doped $KTiOPO_4$ (because of their low conductivity),[27-28)] and $KTiOAsO_4$ (higher transparency in the mid-infrared region).[29)]

The schematic of the lattice structure of KTP is shown in Fig. 3-3-5.[25)] The lattice constants of the material are a = 1.2814 nm, b = 0.6404 nm, and c = 1.0616 nm, respectively, at room temperature. The spontaneous polarization direction is defined as the +c direction. As shown in Fig. 3-3-5, the crystal structure is constructed around TiO_6 octahedrons and PO_4 tetrahedrons. The Curie temperature, T_c, is approximately 936°C and the point group above T_c is mmm. Below T_c, the K^+ ions move slightly in the c-direction, which is believed to be the origin of the spontaneous polarization. In addition, since K^+ has two nonequivalent sites, Ti-O lengths are distorted and that is probably the main cause for the nonlinearity. Since the TiO_6 octahedron chains are separated from the PO_4 tetrahedrons, the chemical bond in the a-plane, which is a cleavage plane, is relatively weak.

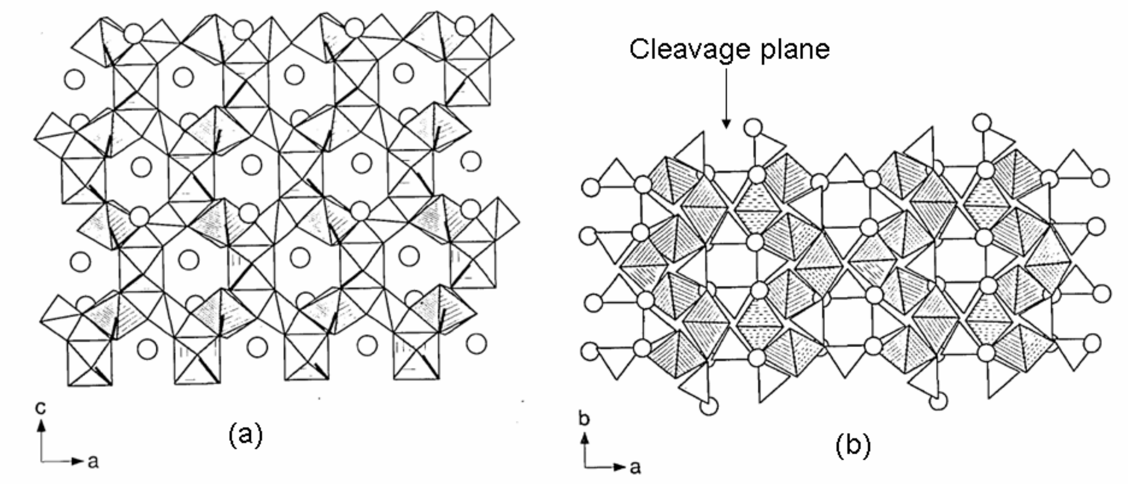

Figure 3-3-5. $KTiOPO_4$ crystal structure: (a) a-c projection, (b) a-b projection. Shaded elements are the Ti octahedra, open elements are the P tetrahedra, and open circles are the K ions. The short Ti-O bonds are shown as bold line.[25)]

Crystal growth methods

As mentioned, there are two different growth methods for KTP and its isomorphs: the hydrothermal growth (HT) method and the flux-growth method. The principle of the HT-method is quite similar to the setup for growing synthetic quartz. The seed crystal is held in an autoclave in which the melt solution is filled. The big difference between quartz and KTP, however, is the temperature and the pressure employed during the growth of KTP: approximately 600°C and a pressure of approximately 1.4×10^8 Pa.[25)] The crystal growth takes approximately 6 weeks for a sample of size 20 mm × 20 mm × 60 mm. Because of the considerable inconveniences regarding the growth conditions, the price of a HT-grown crystal is very high.

The flux-growth method is rather simple compared with the HT-method. The set-up of the crystal-growth system is very similar to the CZ method; however, in this case, the seed crystal is not pulled up during the growth and the crystals are grown inside the melt solution. There are several different types of flux solutions which have been investigated: PO_4, WO_3, and MoO_3. But, in the case of the WO_3 flux, it has been observed that WO_3 contaminates the grown crystals. On the other hand there is no contamination by other atoms while using the PO_4 flux. The phase diagram in the case of the PO_4 flux case is shown in Fig. 3-3-6.[30)] The crystals are grown at temperatures between 950°C and 850°C. The habit of the grown crystal is shown in Fig. 3-3-7.[25)] Since the flux solution is far away from the stoichiometric composition, there are many vacancies of the ions in the grown crystal, especially K^+ vacancies. This is the primary origin of the high ionic conductivity in flux-grown KTP.

Poling treatment

As-grown crystals of KTP have multi-domain structures as well, except for the special case in which KTP crystal is grown at a temperature lower than the Curie temperature.[31)] Although some of these domains are permanent, almost all of the domains have the possibility to invert their sign by applying an electric field as a post-growth process and it is, hence, possible to make single-domain crystals. An example of a reported poling treatment condition is by applying an appropriate electric field in order to keep a current density at a constant value of approximately 5 mA/cm^2. This condition is fulfilled by a voltage of 700 V at a temperature of 200°C or 25 V at 500°C.[32)]

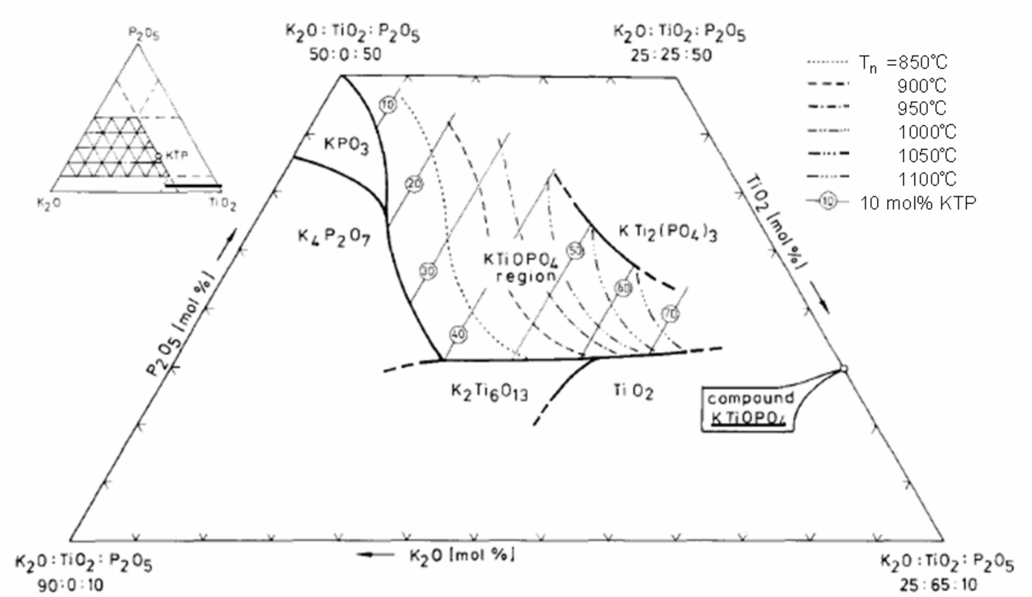

Figure 3-3-6. $KTiOPO_4$ phase diagram with PO_4 flux.[30)]

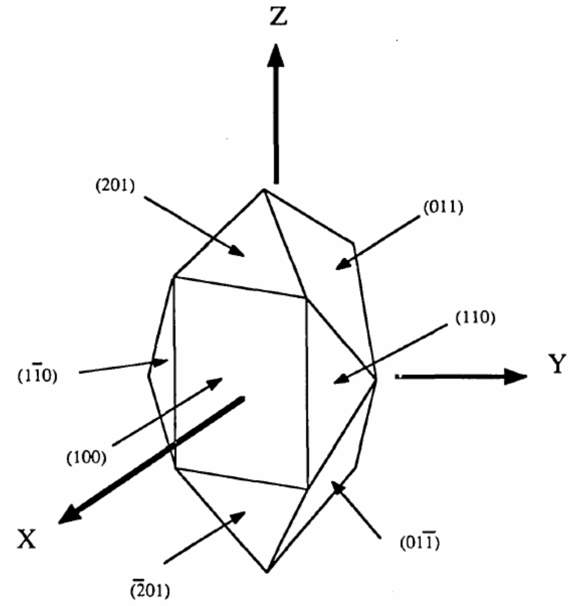

Figure 3-3-7. Natural $KTiOPO_4$ morphology.[25)]

3.3.3. $KNbO_3$

<u>General features</u>

$KNbO_3$ (KN) is an orthorhombic crystal belonging to the point group mm2 at room temperature.[33)] Its ferroelectricity was already observed in 1949.[34)] This crystal belongs to the same perovskite-type crystals such as $BaTiO_3$. Since this crystal has a large piezoelectric constant,[35)] a high electro-mechanical coupling coefficient,36) a relatively high nonlinear and electro-optical coefficient,37) a high optical damage threshold,38) as well as several important applications have been demonstrated for both the piezoelectric and the optical cases. But, the crystal growth of KN is much more difficult as compared to $LiNbO_3$ crystals because of its phase transition on cooling to room temperature and the existence of several possible spontaneous polarization directions. Available sizes of single-domain crystal plates are now available up to 20 mm×20 mm. This crystal has been used as the BPM-SHG material when generating 473 nm, 488 nm, and 532 nm radiation. Especially, the 473 nm radiation has been employed in digital photo-printing systems.

The schematics of the lattice structure of KN are shown in Fig. 3-3-8. The lattice constants are, a = 0.5695 nm, b = 0.3973 nm, and c = 0.5721 nm. The melting point and the Curie temperature, T_c, are approximately equal to 1060°C and 430°C, respectively. This crystal has a cubic structure at temperatures above T_c. Thus, it is sometimes convenient to use the axes of the cubic phase (it's called the pseudo-cubic axis and we therefore use the subscript 'pc' in this case).39) In the present work, when the pseudo-cubic axes are used, the +*a*-, +*b*-, and +*c*-directions of the orthorhombic phase are corresponding to the $[\bar{1}10]_{pc}$, $[001]_{pc}$, and $[110]_{pc}$ directions, respectively, as shown in Fig. 3-3-8.

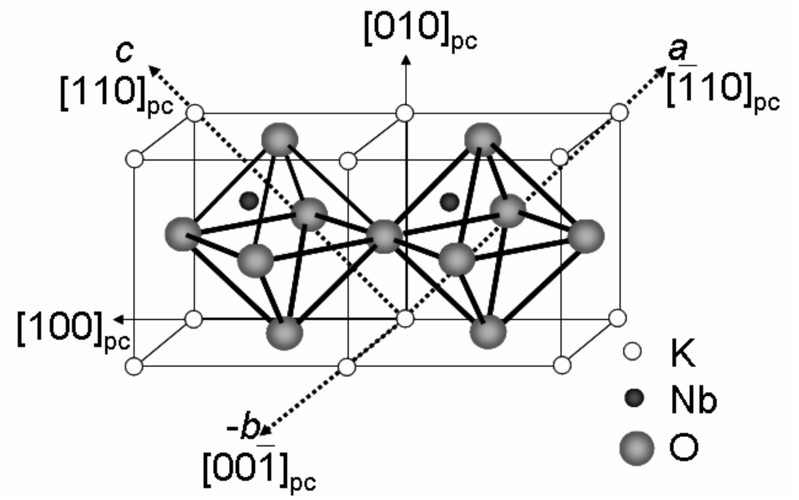

Figure 3-3-8. Schematics of $KNbO_3$ lattice structure and corresponding axes.

<u>Crystal growth methods</u>

The phase diagram of KN is shown in Fig. 3-3-9.40) This crystal is normally grown by the self-flux, top-seeded solution growth method (TSSG). The ratio of the melt composition is K_2O: Nb_2O_5 ≈ 52-54 mol%: 48-46 mol%. The crystal used in this work was grown without pulling from the melt and the material concentration of the grown crystal was almost stoichiometric.

Two different seed types have been demonstrated. One of them is termed $[110]_{pc}$ and the other is called $[100]_{pc}$. The crystals which were used in the present study were grown by employing the $[100]_{pc}$ seed. The schematics of the crystal growth are shown in Fig. 3-3-10. Although it is possible to grow large crystals of up to nearly crucible size, the probability of crack generation during the phase transition when cooling the material, puts a definite size limitation on the finished crystals. Thus, we (at Mitsui Chemicals, Inc.) always grew them to a size of 50 mm×50 mm×20 mm or smaller, which corresponds to approximately 200 g, or less. During the growth of the crystal, the temperature of the heater must go down very slowly by approximately 0.1°C/h, and the whole process took almost one week.

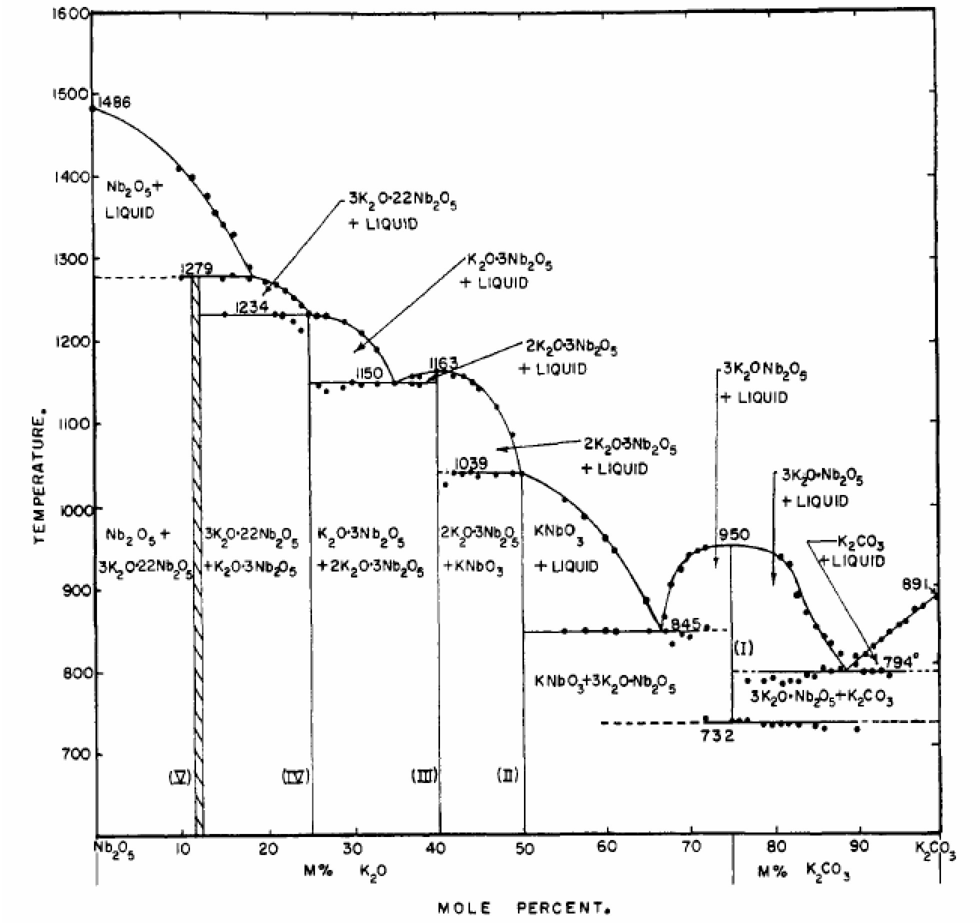

Figure 3-3-9. Phase diagram of the system K_2O-Nb_2O_5.[40)]

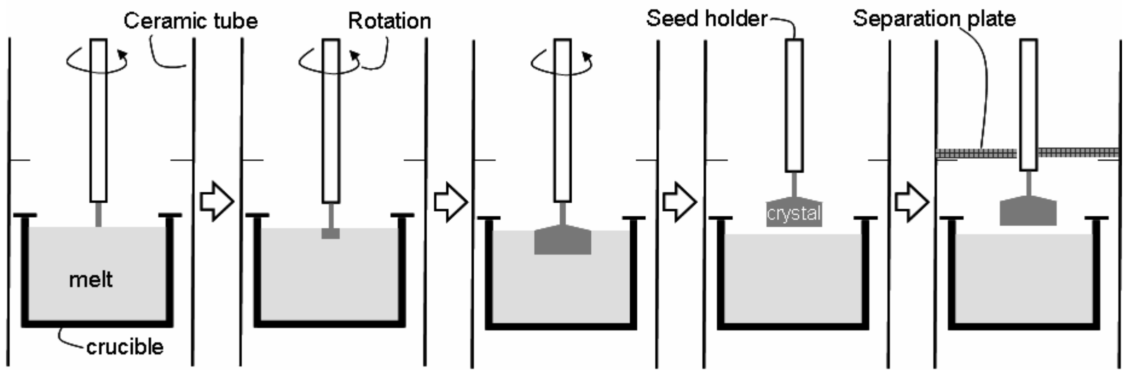

Figure 3-3-10. Schematics of a typical $KNbO_3$ growth process by top-seeded solution growth method (TSSG).

<u>*Phase transition and the cooling process*</u>

After the growth of the KN crystal, it needs to be cooled down to room temperature. As shown in Fig.

3-3-11, KN has four different phases at different temperatures: 1) Cubic (m3m), 2) tetragonal (4mm), 3) orthorhombic (mm2), and 4) rhombohedral (3m). From the growth to room temperature, there are two phase transitions, e. g. cubic to tetragonal and tetragonal to orthorhombic. There are two different types of phase transitions: the first and second order.[2)] The first order transition is characterized by that the amount of spontaneous polarization, $\boldsymbol{P_s}$, changes in a stepwise way at the phase transition. The second order one is defined as the situation in which the amount of $\boldsymbol{P_s}$ changes continuously. All transitions of KN belong to the first order phase transition while those of $LiNbO_3$, $LiTaO_3$, and KTP are of the second order type.

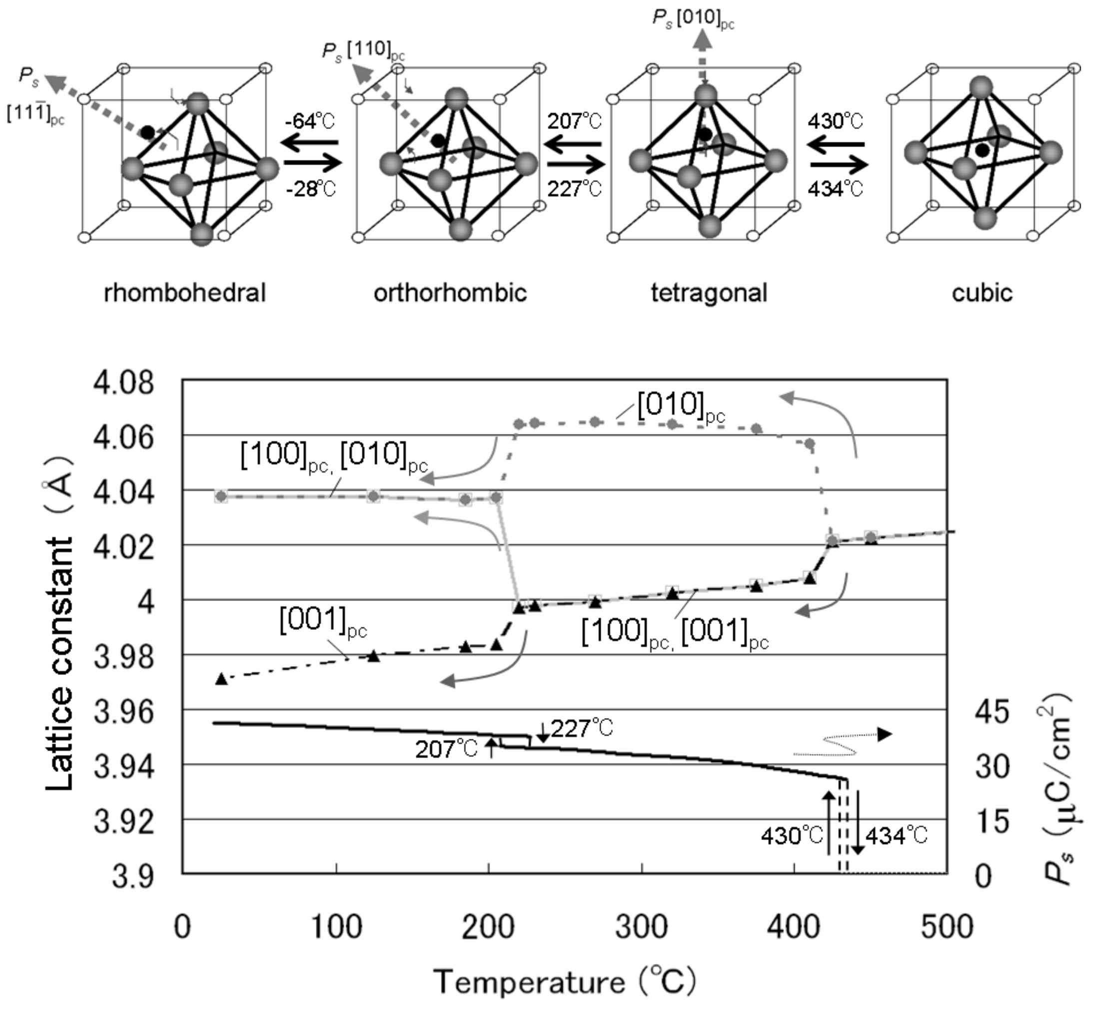

Figure 3-3-11. $KNbO_3$ phase transition.Upper: Schematics of lattice structure in each phase. The temperatures are measured phase transition temperatures. Middle: Temperature dependence of lattice constants of pseudo-cubic axes.[33)] Bottom: Schematics of P_s change and phase transition hysteresis.[41)]

Here, I will focus on the cubic-tetragonal and the tetragonal-orthorhombic phase transitions. The lattice constants of a unit cell of the cubic phase change stepwise at both of the phase transitions as shown in Fig. 3-3-11. At the cubic-tetragonal transition, the Nb^{5+} ion shifts to the $[010]_{pc}$ direction slightly. Thus, the $[010]_{pc}$ direction becomes the $\boldsymbol{P_s}$ direction. But, there are 6 equivalent possible shift directions of the Nb^{5+} ions: $[100]_{pc}$, $[\bar{1}00]_{pc}$, $[010]_{pc}$, $[0\bar{1}0]_{pc}$, $[001]_{pc}$, or $[00\bar{1}]_{pc}$. In principle the direction is chosen randomly. This stepwise change can also be seen visually as shown in Fig.

3-3-12, which displays pictures of a sliced KN plate with a thickness of 120 µm when changing the temperature slowly. When this transition is through smoothly from the top to the bottom, no cracks are occurring. But, when it starts at several different points in the material, these local transitions will collide with each other and produce cracks at the intersection points. Another factor which increases the probability of crack generation is related to the narrow temperature hysteresis of the phase transition. Measuring the phase transition temperature by the differential thermal analysis (DTA) method gives a temperature of 430°C on cooling and, correspondingly, 434°C on heating. Thus, if the temperature around the sample changes by more than 4°C, the phase transition boundary could move back and forth and the probability of crack generation would become higher. When the cracks have occurred, the tetragonal-orthorhombic phase transition boundaries are permanently pinned at those cracks and the un-removable domains will always remain in the crystals even after the single-domain poling treatment.

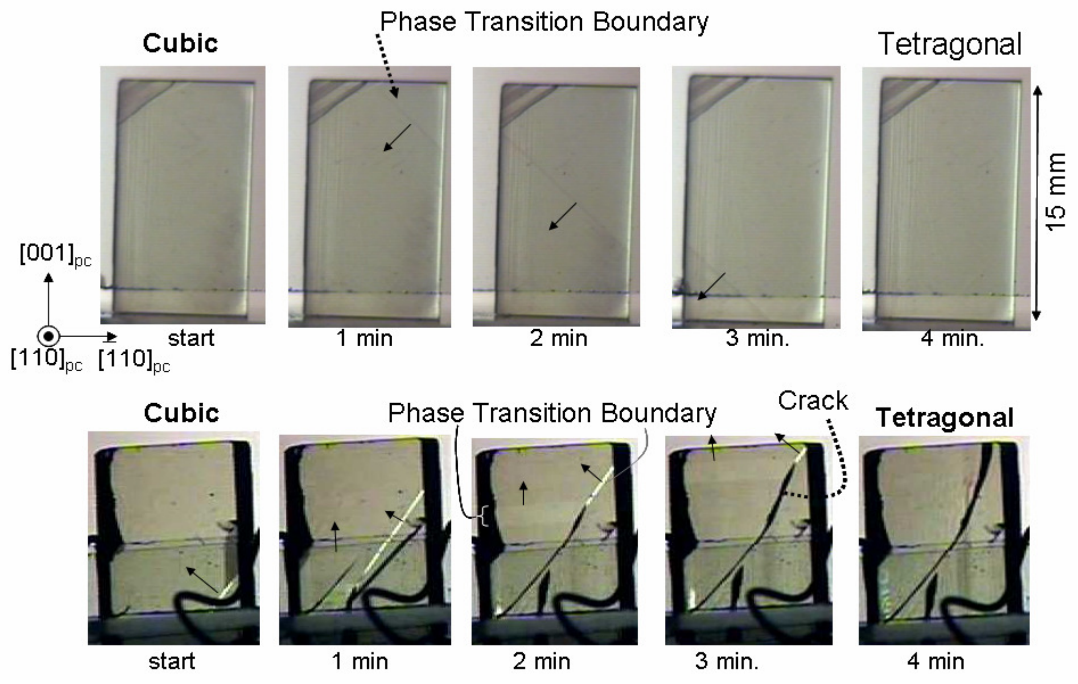

Figure 3-3-12. Cubic to tetragonal phase transition of $KNbO_3$. Upper: Without crack generation. Bottom: Crack created by two phase transition boundaries.

At the tetragonal-orthorhombic transition, the Nb^{5+} ions will shift relative in the $[110]_{pc}$ direction. Thus, the $[110]_{pc}$ now becomes the $\boldsymbol{P_s}$ direction. Here, again, there are 12 equivalent possible Nb^{5+} ion shift directions: $[110]_{pc}$, $[\bar{1}10]_{pc}$, $[1\bar{1}0]_{pc}$, $[\bar{1}\bar{1}0]_{pc}$, $[101]_{pc}$, $[10\bar{1}]_{pc}$, $[\bar{1}01]_{pc}$, $[\bar{1}0\bar{1}]_{pc}$, $[011]_{pc}$, $[01\bar{1}]_{pc}$, $[0\bar{1}1]_{pc}$, or $[0\bar{1}\bar{1}]_{pc}$, and the one which is chosen is selected randomly. This phase transition is also monitored by using a thin KN plate as shown in Fig. 3-3-13. The transparent shadows correspond to the domain walls whose directions are not parallel to the observed direction. Many domain walls are generated when the phase transition starts. After this, the number of the domain walls are reduced. The reason for this might be that the domain wall energy is low at temperatures just below the phase transition temperature and that makes it an easy task for them to merge with each other. This phase transition temperature, as measured by the DTA method, was at 207°C on cooling and 227°C on heating, displaying a hysteresis of 20°C. There would also be some risks for crack generation at this phase transition. Thus, this process also needs to be performed under precise temperature control.

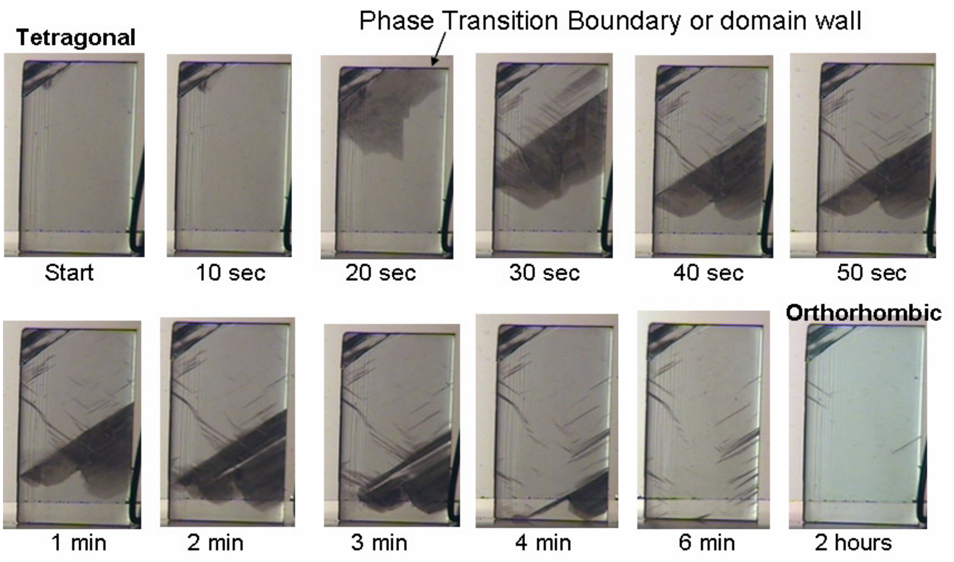

Figure 3-3-13. Tetragonal to orthorhombic phase transition of $KNbO_3$. The sample is the same of above picture in Figure 3-3-12.

Keeping these phase transition phenomena in mind, we have corrected the conditions for the method of the as-grown crystal cooling process accordingly in order to avoid the generation of cracks. This process normally takes one week. We used to cool the grown crystals with a speed of 1.5°C/h within ± 30°C at around both of the phase transition temperatures. However, the cracks were occurring at both of the transitions, especially for the cubic-tetragonal transition. So, the yield of the crystals was normally less than 20%. Since the temperature cooling rate was slow enough, the exact distribution of temperature was also checked. It was more than 15°C at around the first phase transition. As described above, since this phase transition has a hysteresis of only 4°C, this large distribution might be the most detrimental factor in generating the cracks. After we had found that the temperature uncertainty was mainly caused by cold air flowing from the seed holder, a separation plate was inserted when the furnace temperature became around 600°C, as shown in Fig. 3-3-10. As a result, the temperature distribution reduced to approximately 1°C and the yield of the crystals improved to more than 80%. An example of an as-grown, crack-less KN crystal is shown in Fig. 3-3-14.

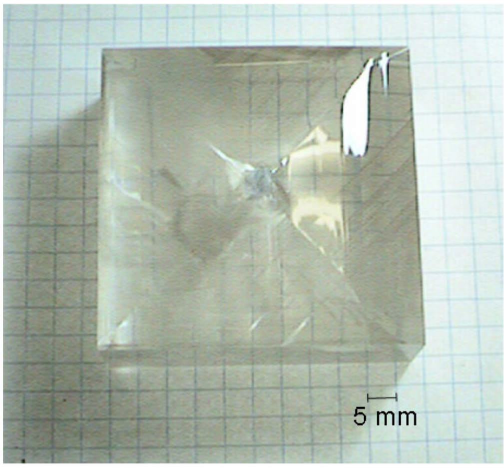

Figure 3-3-14. As-grown $KNbO_3$ crystal.

Poling treatment

As was discussed above, in the orthorhombic phase, there are 12 possible spontaneous polarization directions and these domains are mixed in the as-grown crystal. To make a single-domain crystal, it therefore needs to be poled in one direction. The schematics of the poling process are shown in Fig. 3-3-15. There are no known growth surfaces in the as-grown crystals whose direction is perpendicular to the *c*-axis. Thus, first the *b*-axis is found by using a crossed optical polarizers arrangement, and then we cut the crystal at an angle of 45° from the growth surfaces in order to make it into a cubic block with sides along the *a*-, *b*-, and the *c*-axes. In this cubic block, since the 90°-domains still remain in most cases, the *a*- and the *c*-axis are not yet completely fixed. So, in principle, it is possible to apply the electric field to one of the axes which are perpendicular to the b-axis. However, since the number of 90°-domains has already been stabilized at this stage, it is better to pole in the predominant *c*-axis direction. It is also easy to find the dominant orientation of the domains by measuring the differences of the dielectric coefficients; $\varepsilon_a = 150$ and $\varepsilon_c = 44$. These new blocks were now poled by applying an electric field of 200 V/mm at just below the phase-transition temperature (approximately 215°C) with for 2 hours. To avoid the contamination of the electrode materials, the crystal blocks were clamped by two pieces of sodium glasses which have high conductivities. After this treatment, they were covered by a carbon paste and are annealed at 195°C for 120 hours in order to stabilize the poled domain. Finally, the single-domain crystal blocks were obtained.

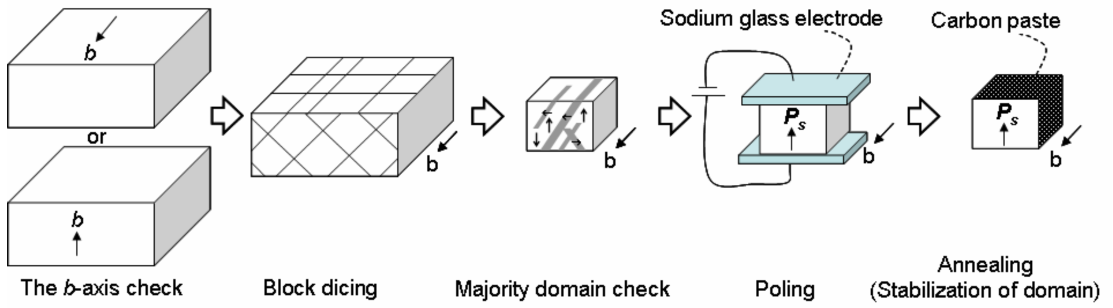

Figure 3-3-15. $KNbO_3$ poling process.

3.4. Optical properties

As described in Section 3.3, the material stoichiometry, the doping, and the domain structure are possible to control during the crystal growth and the post-growth processing. In this section, we describe the comparisons between the important optical properties (the ***d***-coefficient, the figure of merit, the transparency range, and the damage properties) of each material based on the reported values from the literature. We also give a comparison of the QPM periods for the different ferroelectrics for some typical applications.

3.4.1. The d-coefficient and the figure of merit

As mentioned in Section 2.3, the efficiency of the second-order interaction depends on the ***d***-matrix elements employed. The largest of the d elements in the materials which are investigated in this thesis are the d_{33}'s. Naturally, this component is mostly employed in the QPM applications. There are several reported values of the ***d***-coefficients. However, they differ from report to report as shown in Table 3-4-1. The discrepancies observed depend on the fact that measurement methods with different accuracies have been used. Shoji *et al.* reported their results for those investigated ferroelectrics by using the same setup and the same sample dimension. (see the bottom line in Table 3-4-1). Furthermore, the *d*-coefficients are not constant, but they depend on the wavelength region of the interaction. The Miller's Δ can be a good estimation of this dependence. The values of the *d*-coefficient are also to a certain degree dependent on the details of the material composition. It has been reported that the ***d***-coefficients are increasing when the composition becomes near stoichiometric in $LiNbO_3$ and in $LiTaO_3$.[7, 44-45] The ***d***-coefficient (d_{33}) in $LiNbO_3$ is higher than that of the other investigated ferroelectrics. Other components of the ***d***-coefficients are about one order smaller than the d_{33}, except for the d_{31} and d_{32} of $KNbO_3$, which have the values of 11.9 pm/V and 13.7 pm/V for second-harmonic generation of 1.064 μm, respectively.[37]

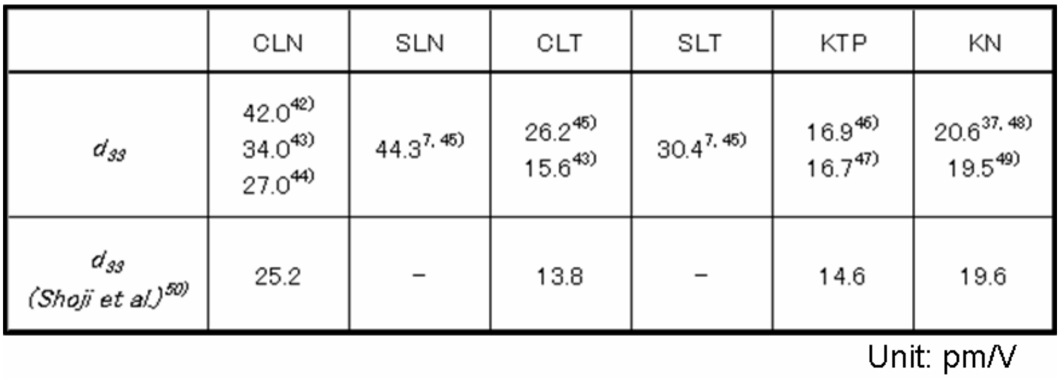

	CLN	SLN	CLT	SLT	KTP	KN
d_{33}	42.0[42] 34.0[43] 27.0[44]	44.3[7, 45]	26.2[45] 15.6[43]	30.4[7, 45]	16.9[46] 16.7[47]	20.6[37, 48] 19.5[49]
d_{33} (*Shoji et al.*)[50]	25.2	–	13.8	–	14.6	19.6

Unit: pm/V

Table 3-4-1. Reported nonlinear coefficient d_{33} values at 1.064 μm.

The actual conversion efficiency is not only a function of the ***d***-coefficient alone but depends also on the refractive indices. For example, the relation between the output power of SHG, $I_{2\omega}$, and the input fundamental intensity, I_ω, is given by the following equation in case of plane waves:[51]

$$I_{2\omega} = \frac{2\omega^2 d^2 L^2 I_\omega^2}{n_{2\omega} n_\omega^2 \varepsilon_0 c^3} sinc^2 \left(\frac{\Delta k L}{2} \right) \quad , \qquad (3.4)$$

where n_ω and $n_{2\omega}$ are the refractive indices at frequencies ω and 2ω, respectively, and L is the interaction length. The other example is the pump intensity at the threshold of OPO, I_{th}, which is given by the following equation:[52]

$$I_{th} = \sqrt{\frac{2}{\pi}} \cdot \frac{2.25}{\kappa \cdot g_s \cdot L^2 \cdot (1+\gamma)^2} \cdot \left(\frac{L}{2c \cdot \tau} \ln(\frac{P_n}{P_o}) + 2 \cdot \alpha \cdot L + \ln \frac{1}{\sqrt{R}} + \ln 4 \right)^2 \quad , \qquad (3.5)$$

where the factor κ is given by the expression:

$$\kappa \equiv \frac{2 \cdot \omega_s \cdot \omega_i \cdot d^2}{\varepsilon_0 \cdot c^3 \cdot n_s \cdot n_i \cdot n_p} \quad , \qquad (3.6)$$

and n_s, n_i, and n_p are the refractive indices for each of the frequencies ω_s, ω_i, and ω_p, respectively, and g_s, L, γ, τ, P_n, P_o, α, and R are parameters related to the experimental condition of the OPO. In both formulas, the material-related components are given by the expression:

$$\frac{d^2}{n_{\omega_1} \cdot n_{\omega_2} \cdot n_{\omega_3}} \quad . \qquad (3.7)$$

This is then the definition of the important *figure of merit* for nonlinear optical materials. The figure of merits are summarized in Table 3-4-2. It is worth noting that the refractive index of $KTiOPO_4$ is considerably smaller than those of the other materials and this partly compensates for the lower value of the nonlinear coefficient for the SHG efficiency.

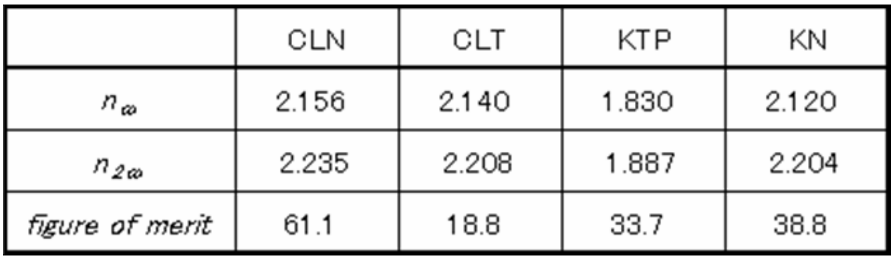

	CLN	CLT	KTP	KN
n_{ω}	2.156	2.140	1.830	2.120
$n_{2\omega}$	2.235	2.208	1.887	2.204
figure of merit	61.1	18.8	33.7	38.8

Table 3-4-2. Comparison of 'the figure of merit' for SHG at 1.064 μm for d_{33}.[50)]

3.4.2. Transparency range

The transparency is, of course, an important parameter for the choice of material in many applications. The reported transparency ranges are summarized in Table 3-4-3. The shorter wavelength cutoff is given by the fundamental electron energy gap, E_g, which is a function of crystal structure and the type of bonds. Non-stoichiometry and other defects in crystallinity are expected to produce band-tails where absorption is possible, thus shifting the apparent cut-off to longer wavelengths. A typical example of the effect of non-stoichiometry is the shorter cut-off wavelengths of stoichiometric $LiNbO_3$ and $LiTaO_3$ than those of the congruent ones. In the mid-infrared, all oxide ferroelectrics are cut-off at wavelengths around 5 μm, due to a predominant absorption of light frequency vibration by the oxygen bonds (P-O, Nb-O, Ta-O, or As-O). As a general trend, heavier metals in the bonds give a slightly smaller vibration frequency, which means a longer absorption cut-off wavelength. Thus, as an example, $KTiOAsO_4$ has a higher transmission and a longer cut-off wavelength than that of $KTiOPO_4$.

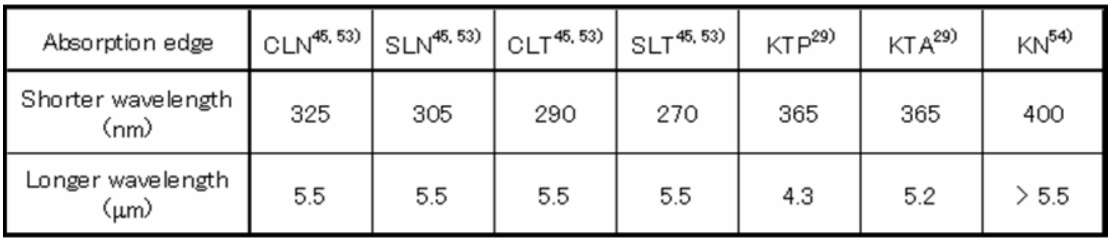

Absorption edge	CLN[45, 53)]	SLN[45, 53)]	CLT[45, 53)]	SLT[45, 53)]	KTP[29)]	KTA[29)]	KN[54)]
Shorter wavelength (nm)	325	305	290	270	365	365	400
Longer wavelength (μm)	5.5	5.5	5.5	5.5	4.3	5.2	> 5.5

Table 3-4-3. Transparency range of different materials. CLN: congruent $LiNbO_3$*, SLN: stoichiometric* $LiNbO_3$*,CLT: congruent* $LiTaO_3$*, SLT: stoichiometric* $LiTaO_3$*,, KTP:* $KTiOPO_4$*, KTA:* $KTiOAsO_4$*, KN:* $KNbO_3$

3.4.3. Optical damage properties

There are mainly three different types of optical damages: photorefraction, color center formation (gray-tracking), and ionic bond breakdown due to multi photon ionization, thermal stress, local melting, etc. These effects depend on the experimental conditions such as the peak intensity, the average power, the wavelength, and the types of nonlinear process.

Photorefraction is a light-induced change of the refractive index. High intensity light incident on a material will produce photocarriers inside the material. These carriers will be separated at the electron and hole traps in the material either by different diffusion rates or by the internal electric fields. There they will produce an electric field and, through the electro-optic effect, create a refractive index change. This phenomenon is substantial and easily observed in congruent $LiNbO_3$ and $LiTaO_3$. In the early days of this research, it was expected that photorefraction could be reduced by decreasing the number of Li^+ vacancies. However, photorefraction in fact becomes strong for compositions close to stoichiometry in $LiNbO_3$.55) In the case of $LiTaO_3$, though, the stoichiometric composition shows less photorefraction than the congruent one.6) In both the stoichiometric and the congruent $LiNbO_3$ and $LiTaO_3$, it has been reported that MgO doping will effectively reduce the photorefraction as shown in Fig. 3-4-1.6, 56) $KTiOPO_4$ does not show photorefraction, a fact that might be due to its high conductivity, which largely screens out the internal and the induced electric fields. $KNbO_3$ does not show it either, which might be due to its almost stoichiometric composition.

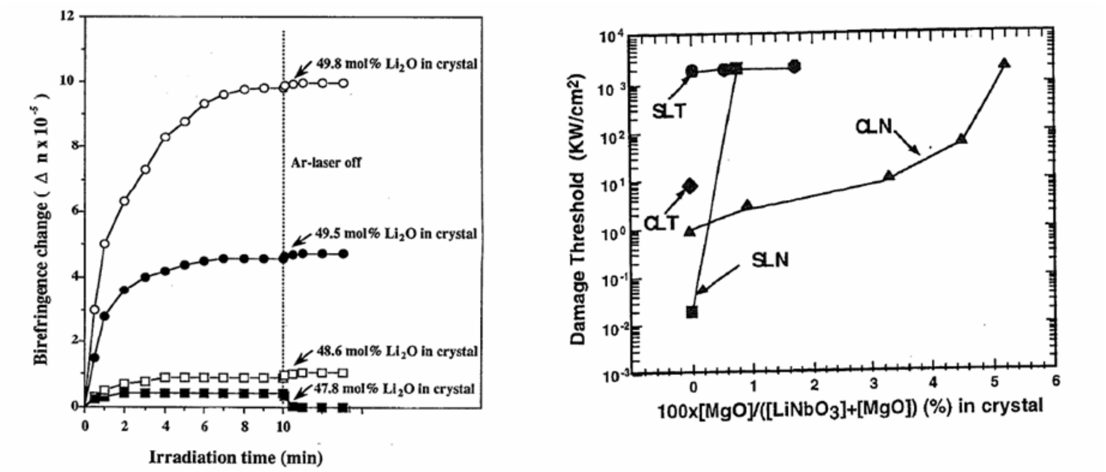

Figure 3-4-1. Photorefraction phenomena in $LiNbO_3$ and $LiTaO_3$.6, 54) Left: Transition of photorefraction of $LiNbO_3$ with different Li_2O concentration. Right: Photorefractive damage threshold as a function of MgO concentration. CLN: congruent $LiNbO_3$, SLN: stoichiometric $LiNbO_3$, CLT: congruent $LiTaO_3$, SLT: stoichiometric $LiTaO_3$,

Gray-tracking is a phenomenon in which high-power laser light creates absorbing color centers in the material. This effect is reported in $KTiOPO_4$ and its mechanisms have been investigated extensively.57) Some new and doped $KTiOPO_4$ crystals with a reported high gray-track threshold have been produced lately; however, unfortunately, it has been found difficult to change their $\boldsymbol{P}_s$ direction by applying electric fields, probably due to domain wall pinning by the additional dopants. The process of creating the color centers is quite similar to the increase of the light-induced broadband absorption caused by exposure to a combination of visible and infrared radiation, which is called GRIIRA (green light-induced infrared absorption) or BLIIRA (blue light-induced infrared absorption). Since this effect causes problems for frequency doubling from the infrared to visible light, it has also been carefully investigated for $LiNbO_3$,56) $LiTaO_3$,6) and for $KNbO_3$.58) We have systematically investigated BLIIRA in a number of our ferroelectrics which have a high potential for QPM SHG applications as discussed in Chapter 6.

The typical GRIIRA properties observed in $KTiOPO_4$ are shown in Fig. 3-4-2.59) This profile shows a relatively slow accumulation of color centers with a time constant of 1.3 s. The GRIIRA in $LiNbO_3$ and $LiTaO_3$ have mainly been investigated for their characteristic properties by employing a 5 ns pulsed green laser as shown in Fig. 3-4-3.6) GRIIRA can also be suppressed by MgO doping. Generally speaking, $LiTaO_3$ has a lower GRIIRA response and its stoichiometric composition also shows a lower induced absorption than the congruent one without MgO doping. Existing models try to explain the GRIIRA phenomena in $LiNbO_3$ and $LiTaO_3$ by referring to native defects. For example, an anti-site Nb-ion model has been introduced, in which some Nb-ions are located at the Li-ion sites.20) Based on this idea, if there are no anti-site Nb ions, the GRIIRA effect should be suppressed. But, the origin of GRIIRA is not clearly understood as yet. BLIIRA in $KNbO_3$ has also been reported by using a continuous wave (CW) 860 nm laser and its second-harmonic blue light.[58] The BLIIRA starts to get observable at an intensity of 5 kW/cm^2 of CW blue light. This is a rather low threshold value compared to those reported for $LiNbO_3$ and $LiTaO_3$ in the case of pulsed excitation. These results are pointing to the importance of investigating the creation of the induced color centers and the corresponding relaxation dynamics in these materials, which we have carried out in this thesis.

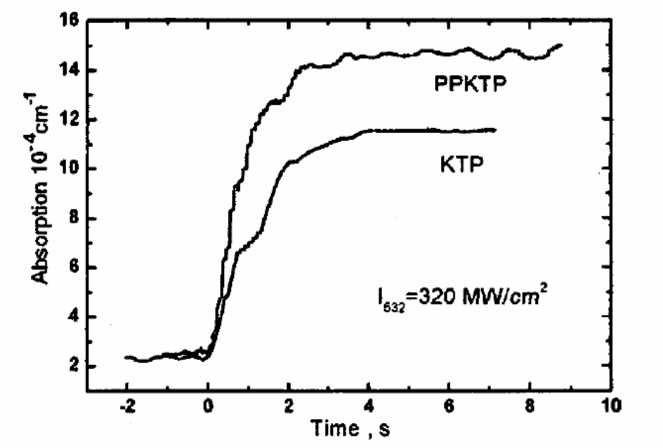

Figure 3-4-2. Typical GRIIRA transition in $KTiOPO_4$ (KTP) and in periodically-poled KTP (PPKTP).[58]

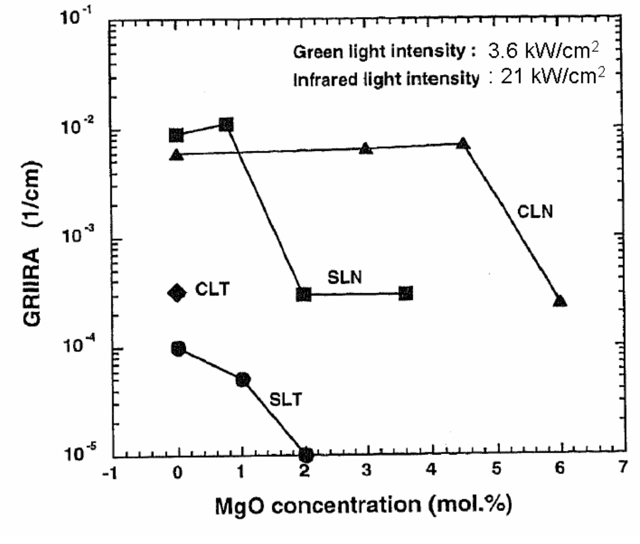

Figure 3-4-3. GRIIRA versus MgO concentration in $LiNbO_3$ and $LiTaO_3$.[6] *CLN: congruent $LiNbO_3$, SLN: stoichiometric $LiNbO_3$, CLT: congruent $LiTaO_3$, SLT: stoichiometric $LiTaO_3$.*

The last issue is the mechanical breakdown. By increasing the peak intensity or the average power of the incident laser beam, all crystals will break down mechanically by burning or cracking at some certain power level. Since $KTiOPO_4$, $LiNbO_3$, and $LiTaO_3$ all have photorefractive and/or gray-tracking problems, these effects could also reduce their corresponding thresholds of the mechanical breakdown. The mechanical breakdown of $KNbO_3$ has also been reported and the attended threshold level was 8.2 GW/cm^2 for 532 nm radiation of a 500 ps pulsed laser.[38] The power level of catastrophic mechanical breakdown is typically much higher than that of the GRIIRA, the

BLIIRA, or the photorefractive damage thresholds. In KTP, the material breakdown threshold has been investigated by pulsed 1.046 μm laser. When the pulse repetition rate was increased, the breakdown threshold level decrease, for example, in the case of a pulse width of 220 ns and with a repetition rate of 1.2 kHz case, the threshold was 71 MW/cm^2, while in the case of a pulse widths of 220 ns and with a repetition rate of 15 kHz case, the threshold was 16.4 MW/cm^2.60)

3.4.4. QPM periods

The QPM period can be calculated from Eq. (2.19). The phase differences are calculated from the corresponding wavelength dependences of the refractive indices. As a comparison of the QPM periods, Fig. 3-4-4 shows the wavelength dependences of the QPM period for second-harmonic generation by using the d_{33} coefficient. Although the Sellmeier Equation for stoichiometric $LiNbO_3$ has not been reported yet, the difference of the periods between that of the congruent and the near stoichiometric cases is only a few percent. The QPM period for $KTiOPO_4$ is relatively longer than that of $LiNbO_3$, $LiTaO_3$, and $KNbO_3$. Especially around the visible light region, the period of $KTiOPO_4$ is roughly 1.5 times larger than those of $LiNbO_3$ and $KNbO_3$. This is an advantage because the fabrication of periodically-poled structures gets dramatically more difficult for periods smaller than 10 μm. It is worth noting that the QPM period for $KNbO_3$, when employing the d_{31} components for the blue-green region, is much larger and hence it is easier to fabricate the structure.Paper II) This is because $KNbO_3$ has a non-critical phase-matching point for a second-harmonic wavelength of 488 nm. It is also important to note that the QPM period is almost the same at around the 780 nm region (which corresponds to a fundamental wavelength around 1.55 μm) by using the d_{31} components of $KNbO_3$. This rather wide wavelength acceptance is very useful for pulse compression by using the so-called $\chi^{(2)}$-cascading technique.Paper A4) The corresponding period for OPO applications when pumped by a 1.064 μm is approximately 30 μm for all of the investigated materials by employing the d_{33} components.

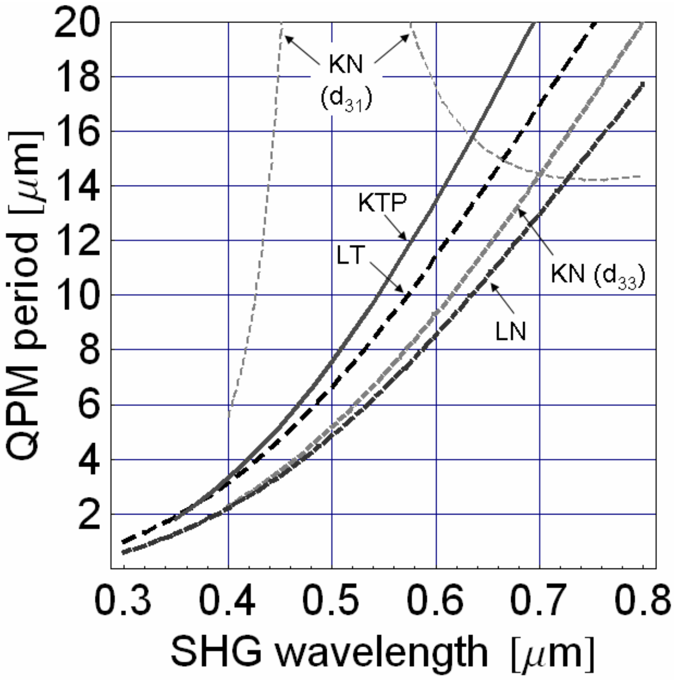

Figure 3-4-4. QPM periods for SHG by using d_{33} for $LiNbO_3$,61) $LiTaO_3$,62) $KTiOPO_4$,63) and $KNbO_3$.64) (LN: MgO-doped congruent $LiNbO_3$, LT: non-doped stoichiometric $LiTaO_3$.)

References in Chapter 3

1) B. A. Auld: Acoustic fields and waves in solids (Wiley, New York. 1973), Chap. 7, p. 191.

2) T. Nakamura, T. Sakudo, Y. Ishibashi, and Y. Tominaga: Ferroelectricity involved in structural phase transitions (Shokabo, Tokyo. 1988), p. 6.

3) B. T. Matthias and J. P. Remeika: Phys. Rev. **76**, 1886 (1949).

4) A. A. Ballman: J. A. Ceram. Soc. **48**, 112 (1965).

5) Y-F. Zhou, J-C. Wang, P-L. Wang, L-A. Tang, Q-B. Zhu, Y-A. Wu, and H-R. Tan: J. Cryst. Growth, **114**, 87 (1991).

6) K. Kitamura, Y. Furukawa, S. Takekawa, T. Hatanaka, H. Ito, and V. Gopalan: Ferroelectrics **257**, 235 (2001).

7) T. Fujuwara, M. Takahashi, M. Ohama, A.J. Ikuhima, Y. Furukawa, and K. Kitamura: Elctron. Lett. **35**, 499 (1999).

8) B. C. Grabmaier, W. Wersing, and W. Koestler: J. Cryst. Growth **110**, 339 (1991).

9) Y. Furukawa, K. Kitamura, E. Suzuki, and K. Niwa: J. Cryst. Growth **197**, 889 (1999).

10) J. R. Carrunthers, G. E. Peterson, M. Grasso, and P. M. Bridenbaugh: J. Appl. Phys. **42**, 1846 (1971).

11) S. Miyazawa and H. Iwasaki: J. Cryst. Growth **10**, 276 (1971).

12) J. Kushibiki, T. Okuzawa, J. Hirohashi, and Y. Ohashi: J. Appl. Phys. **87**, 4395 (2000).

13) J. Kushibiki, Y. Ohashi, and J. Hirohashi: J. Appl. Phys. **98**, 123507 (2005).

14) D. H. Jundt, M. M. Fejer, and R. L. Byer: IEEE. J. Quant. Electron. **26**, 155 (1990).

15) K. Polgar, A. Peter, L. Lovacs, G. Corradi, and A. Szaller: J. Cryst. Growth **177**, 211 (1997).

16) B. M. Park, K. Kitamura, K. Terabe, Y. Furukawa, Y. Ji, and E. Suzuki: J. Cryst. Growth **180**, 101 (1997).

17) K. Kitamura, J. K. Yamamoto, N. Iyi, and T. Hayashi: J. Cryst. Growth **116**, 327 (1997).

18). Y. Zheng, E. Shi, Z. Lu, S. Cui, S. Wang, and W. Zhong: J. Cryst. Growth **275**, 895 (2005).

19) M. Nakamura, S. Takekawa, Y. Furukawa, and K. Kitamura: J. Cryst. Growth **245**, 267 (2002).

20) Y. Furukawa, K. Kitamura, S. Takekawa, A. Miyamoto, M. Terao, and N. Suda: Appl. Phys. Lett. **77**, 2494 (2000).

21) N. E. Yu, S. Kurimura, Y. Nomura, M. Nakamura, K. Kitamura, Y. Takeda, J. Sakuma, and T. Sumiyoshi: Appl. Phys. Lett., **85**, 5134 (2004).

22) L. Ouvrard and M. Troost: Compt. Rend. **111**, 170 (1890).

23) F. C. Zumsteg, J. D. Bierlein, and T. E. Gier: J. Appl Phys. **47**, 4980 (1976).

24) L. K. Cheng, E. M. McCarron III, J. Calabrese, J. D. Bierlein, and A. A. Ballman: J. Cryst. Growth, **132**, 280 (1993).

25) J. D. Bierlein and H. Vanherzeele: J. Opt. Soc. Am. B **6**, 622 (1989).

26) http://www.cobolt.se.

27) H. Karlsson, F. Laurell, and L. K. Cheng: Appl. Phys. Lett. **74**, 1519 (1999).

28) Q. Jiang, P. A. Thomas, K. B. Hutton, and R. C. C. Ward: J. Appl Phys. **92**, 2717 (2002).

29) G. Hansson, H. Karlsson, S. Wang, and F. Laurell: Appl. Opt. **39**, 5058 (2000).

30) K. Iliev, P. Peshev, V. Nikolov, and I. Koseva: J. Cryst. Growth, **100**, 225 (1990).

31) M. N. Satyanarayan and H. L. Bhat: J. Cryst. Growth, **181**, 281 (1997).

32) J. D. Bieriein and F. Ahmed: Appl. Phys. Lett. 51, 1322, (1987).

33) A. W. Hawat: J. Phys. C: Sol. Stat. Phys **6**, 2559 (1973).

34) B. T. Matthias: Phys. Rev. **75**, 1771 (1949).

35) M. Zgonik, R. Schlesser, I. Biaggio, E. Voit, J. Tscherry and P. Gunter: J. Appl. Phys. **74** (1993) 1287.

36) K. Nakamura, T. Tokiwa, and Y. Kawamura: J. Appl. Phys. **91** (2002) 9272.

37) I. Biaggio P. Kerkoc, L.-S. Wu, P. Gunter, and B. Zysset: J. Opt. Soc. Am. B **9**, 507 (1992).

38) U. Ellenberger, R. Weber, J. E. Balmer, B. Zysset, D. Ellgehausen, and G. J. Mizell: Appl. Opt. **31**, 7563 (1992).

39) E. Weisendenger: Czech. J. Phys. B **23**, 91 (1973).

40) A. Reisman and F. Holtzberg: J. Am. Chem. Soc. **77**, 2115 (1955).

41) P. Gunter: J. Appl. Phys. **48**, 3475 (1974).

42) G. D. Boyd, R. C. Miller, K. Nassau, W. L. Bond, and A. Savage: Appl. Phys. Lett. **5**, 234 (1964).

43) R. C. Miller and A. Savage: Appl. Phys. Lett. **9**, 169 (1966).

44) R. C. Miller, and W. A. Nordland: J. Appl Phys. **42**, 4145 (1971).

45) www.opt-oxide.com.

46) H. Vanherzeele and J. D. Bierlein: Opt. Lett. **17**, 982 (1992).

47) V. Pasiskevicius, S. Wang, J. A. Tellefsen, F. Laurell, and H. Karlsson: Appl. Opt. **37**, 7116 (1998).

48) J.-C. Baumert, J. Hoffnagle, and P. Gunter: SPIE **492**, 374 (1984).

49) D. A. Roberts: IEEE. J. Quant. Electro. **28** 2057, (1992).

50) I. Shoji, T. Kondo, A. Kitamoto, M. Shirane, and R. Ito: J. Opt. Soc. Am. B, **14**, 2268 (1997).

51) G. D. Boyd and D. A. Kleinman: J. Appl. Phys. **39**, 3597 (1968).

52) S. J. Brosnan and R. L. Byer: IEEE J. Quant. Electro. **15**, 415 (1979).

53) V. Gopalan, N. Sanford, J. A. Aust, K. Kitamura and Y. Furukawa: "Handbook of Advanced Electronic and Photonic Materials" edited by H. S. Nalwa, Academic Press (Oct. 2001) p. 62

54) T. Fukuda and Y. Uematsu: Jpn. J. Appl. Phys. 11, 163 (1992).

55) Y. Furukawa, M. Sato, K. Kitamura, Y. Yajima, and M. Minakata: J. Appl Phys. **72**, 3250 (1992).

56) Y. Furukawa, K. Kitamura, A. Alexandrovski, R. K. Route, M. M. Fejer, and G. Foulon: Appl. Phys. Lett. **78**, 1970 (2001).

57) For example:M. P. Scripsick, D. N. Lolacono, J. Rottenberg, S. H. Gollner, L. E. Halliburton, and F. K. Hopkins: Appl. Phys. Lett. 66, 3428 (1995).

58) H. Mabuchi, E. S. Polzik, and H. J.Kimble: J. Opt. Soc. Am. B **11**, 2023 (1994).

59) S. Wang, V. Pasiskevicius, and F. Laurell: J. Appl Phys. **96**, 2023 (2004).

60) S. Wang, "Fabrication and characterization of periodically-poled KTP and Rb-doped KTP for applications in the visible and UV," Ph. D Thesis. ISBN 91-7178-153-6, Royal Institute of Technology, (2005).

61) D. E. Zelmon, D. L. Small, and D. Jundt: J. Opt. Soc. Am. B **14**, 3319 1997).

62) A. Bruner, D. Eger, M. B. Oron, P. Blau, M. Katz, and S. Ruschin: Opt. Lett. **28**, 194 (2003).

63) T. Y. Fan, C. E. Huang, B. Q. Hu, R. C. Eckardt, Y. X. Fan, R. L. Byer, and R. S. Feigelson: Appl. Opt. **26**, 2390 (1987).

64) B. Zysset, I. Biaggio and P. Gunter: J. Opt. Soc. Am. B **9**, 380 (1992).

Chapter 4. Characterization of spontaneous polarization switching$^{\text{Paper I-IV)}}$

4.1. Introduction

In order to consistently fabricate high fidelity domain structures for QPM applications, it is important to understand the close interplay between the material properties such as doping, concentration of vacancies, etc, and the electrical characteristics relevant for electric-field poling such as the ionic conductivity, spontaneous polarization, and coercive field. This understanding will facilitate optimization of the electric pulse shape, its amplitude, and the poling procedure which is critical for successful QPM fabrication. At the same time, the ferroelectric domain morphologies are also important issues for consideration in sub-µm domain structures as well as in the ferroelectrics which can sustain several different types of domains, such as $KNbO_3$.

In this chapter, first, the typical switching properties of bulk, single crystals and the measurement setup are described. Then, the measured fundamental properties for each investigated ferroelectric material are described as based on our own experimental results. In the case of $KNbO_3$, the domain switching phenomena of non-180° domain structures are also described. In Section 4.3, the domain morphologies are shown and its origin is discussed.

4.2. Electrical properties in spontaneous polarization switching

4.2.1. The P-E hysteresis loop and the measurement setup

As mentioned in Section 3.2, the spontaneous polarization can be switched by applying an electric field and a typical *P-E* hysteresis loop is shown in Fig. 3-2-1. The hysteresis loop is measured by applying a triangular electric field to the ferroelectric materials and monitoring the current through the sample. The relation between the current, i, and spontaneous polarization, P_s, is given by the following equation:

$$P_s = \frac{Q}{2A} = \frac{\int i \cdot dt}{2A} \quad , \qquad (4\text{-}1)$$

where A is the size of the switching area and Q is the total integrated charge transferred through the circuit. Here, the inherent assumption is that only the polarization switching current contributes to the total measured current for any given voltage. For the case of thin film ferroelectrics, this hysteresis sequence is typically symmetric both for the polarization, P, and the electric field, E. This is because it is easy to flip back the P_s by applying an electric field and no remnant stress then will remain inside the film. These measurements are typically performed at a high frequency of around 100 kHz since the typical application is focused on ferroelectric memory devices by using the spontaneous polarization switching.$^{1)}$

In the case of bulk single crystals, it is important to know the detail of the electrical properties of the material at low frequencies. For example, electric-field pulses with durations ranging from milliseconds to minutes are typically used for the periodic-poling process of different ferroelectrics. The spontaneous polarization of bulk single crystal is rather more difficult to switch back and forth compared with that of the thin films. Since the remnant polarization stress or internal fields remain after the switching, the *P-E* hysteresis becomes asymmetric. A typical example for congruent $LiTaO_3$ is shown in Fig. 4-2-1.$^{2)}$ Here, we define the forward and the reverse poling as the poling of the original state to the opposite state and, consequently, that of the opposite state to the original state, respectively. The coercive field for forward poling, E_{cf}, is typically larger than that of the reverse poling, E_{cr}. The differences between E_{cf} and E_{cr} are related to the Li^+ vacancies in the $LiNbO_3$ or $LiTaO_3$ cases. This is described by a parameter called the internal field, E_i, which is defined by $E_i = [E_{cf}-E_{cr}]/2$. It has been reported that all of the values of E_{cf}, E_{cr}, and E_i become smaller as the concentration becomes near stoichiometry in the cases of $LiNbO_3$ and $LiTaO_3$.$^{2-3)}$

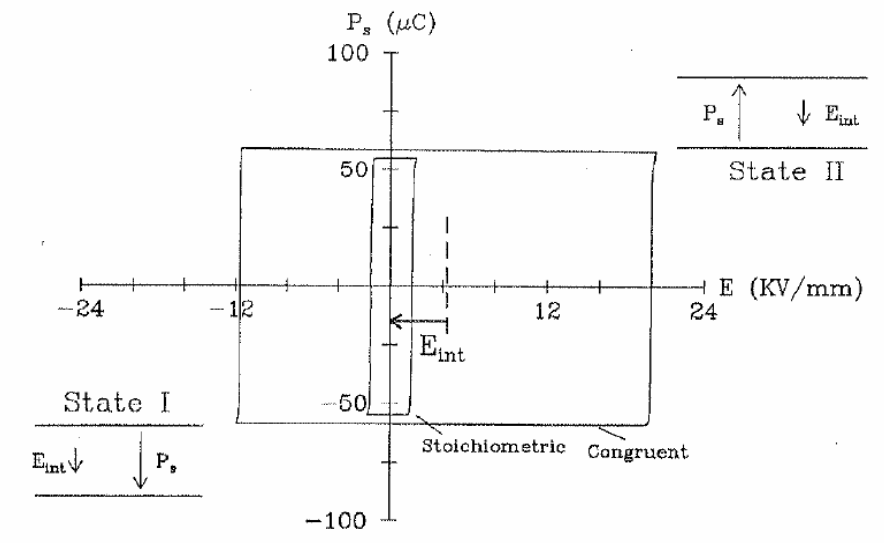

Figure 4-2-1. P-E hysteresis loop of congruent and stoichiometric $LiTaO_3$.$^{2)}$

A second important factor is the material conductivity. If the material has a high electrical conductivity, the current which flows during the applied electric field is not only due to the spontaneous polarization change, as described in Eq. (4-1). In that case, based on the Mott-Gurney quadratic law,$^{4-5)}$ the current density during the poling is more completely given by the expression:

$$J = \frac{9}{8}\varepsilon\varepsilon_0\mu\frac{V^2}{L^3} + 2P_s\frac{1}{A}\frac{\partial A_i}{\partial t} \quad , \qquad (4\text{-}2)$$

where ε is the permittivity of the material, ε_o is the permittivity of the vacuum, μ is the ionic mobility, L is the thickness of the material, V is the applied voltage and A_i is the area of the inverted region. Even for highly conductive materials, it has indeed been possible to measure the approximate coercive field by choosing a properly shaped triangular pulse which is satisfied the following equation:

$$\frac{\partial V}{\partial t} < \frac{8}{9}\frac{P_s L^3}{\varepsilon\varepsilon_0\mu A}\frac{\partial^2 A_i}{\partial t^2} \quad . \qquad (4\text{-}3)$$

A third important issue is the capacitive charge layers which might exist on the surface of the investigated samples in order to neutralize the spontaneous polarization-related electric field. This effect could be one of the sources which will determine the coercive field, the switching time, and the stabilization for the domain switching. This effect might change by the different surface conditions such as the metal coating and by the surface roughness of the samples.

Summarizing the above effects, it could be valid to make an equivalent circuit for the sample as shown in Fig. 4-2-2(a), where C_B and C_s are the capacitances of the bulk and the surface layer, respectively, and R_B and R_s are the resistance of bulk and the surface layer, respectively. Domain switching can appear after the filling of charges in both capacitances C_B and C_s. Thus, the coercive field, then, is a function of not only the bulk properties but also of the surface properties.

The experimental setup used in this thesis for the measurement of these parameters is shown in Fig. 4-2-2(b). The high-voltage signal is delivered from an amplifier (Trek model 20/20C or Matsusada Precision Inc, Model HEOPT-20B10), and controlled by an arbitrary function generator (Agilent model 33120A or Yokogawa Electric Corp. Model AG2200). It is then applied to the ferroelectric crystal. In general, the measured coercive field, E_c, depends on the measuring frequency, the structure of the electrodes, the waveform of the applied voltages, and the size of the poled area. In this work, the contacts to the samples were made with a nearly saturated solution of LiCl or KCl. In all of the cases, the serial resistance, R_1, is relatively low (0 Ω or 15 kΩ). The voltage across the sample and the current are monitored through the voltage across the resistance R_3 and R_4, respectively. The R_2, R_3, and R_4 were set to be equal to 100 MΩ, 100 kΩ, and 10 kΩ, respectively.

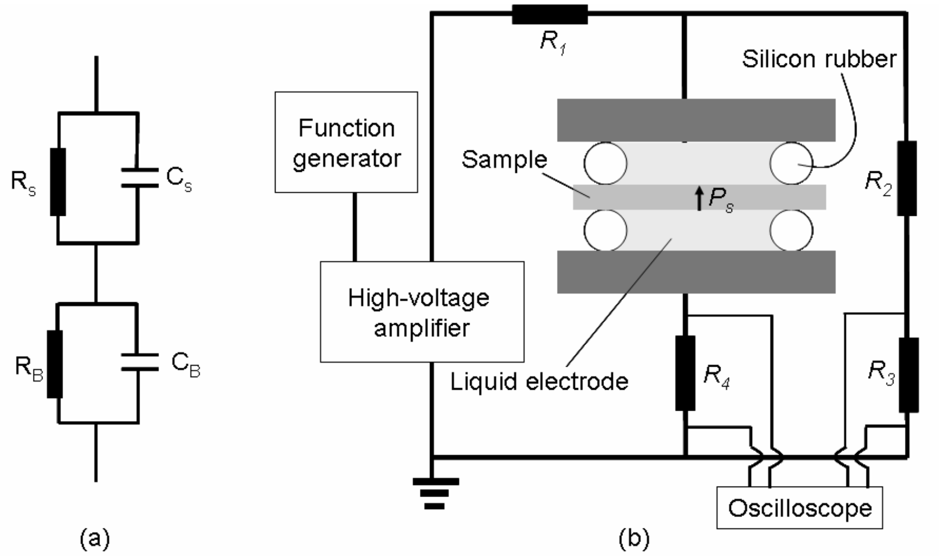

Figure 4-2-2. (a) Equivalent circuit model for the material and (b) poling circuit.

The triangular electric pulse was applied with a rate optimized to clearly see the coercive field and the switching current. The poled area was approximately of size ranging from 0.25 cm×0.25 cm to 0.40 cm×0.40 cm. Although it would seem that the best way to compare the different materials is to apply the same ramp rate of the voltage, it is difficult to do so because of the huge differences between the material properties such the conductivity and the coercive fields. Nevertheless, whenever possible, we tried to use the same 100 ms long triangular pulse length for the characterization. The sampling scale depended on the expected coercive field. For the condition of a low increase rate of the applied voltage, the current caused by the effects of the material bulk capacitance, C_B, are negligible. Since some materials could not be switched during such a short time period, different pulse widths were also tested. In addition, the dependence of the coercive field on the number of repetitions of the P_s switching was also investigated.

The investigated materials are listed below and their properties are described in the following sections. In what follows, periodically-poled crystals are denoted by the abbreviations PP (for example, PPMgO:SLN and PPKTP). The thickness of all of the measured samples was 1 mm.

MgO:SLN: 1 mol% MgO-doped stoichiometric $LiNbO_3$ fabricated by the DC-CZ method by OXIDE Corporation.

MgO:SLT:	1 mol% MgO-doped stoichiometric $LiTaO_3$ fabricated by the DC-CZ method by OXIDE Corporation.
SLT:	Non-doped stoichiometric $LiTaO_3$ fabricated by the DC-CZ method by OXIDE Corporation.
KTP:	$KTiOPO_4$ grown by the flux-growth method by Bright Crystals Technology, Inc.
RTP:	$RbTiOPO_4$ grown by the flux-growth method by Crystal Laser.
KN:	$KNbO_3$ grown by the TSSG method by Mitsui Chemicals, Inc.

4.2.2. Stoichiometric LiNbO₃ and LiTaO₃

MgO:SLN

The initial conductivity of the MgO:SLN was low enough for poling and could not be measured. Figures 4-2-3(a)-(c) show the measured electric field and the current profile for different pulse lengths (100 ms, 1 s, and 10 s). For the case of the pulse width of 100 ms, the current did not flow until the voltage signal was applied three times. For the case of the widths of 1 s, the current started to flow after decreasing the amplitude of the applied voltage. For the case of the width of 10 s, it was possible to check the coercive field. From these results, it was expected that the MgO:SLN needed a relatively higher energy accumulation in order to switch the P_s direction, thus, it was necessary to apply a longer pulse or even many pulses. The measured coercive fields (E_{cf}, E_{cr}) and the internal field, E_i, at 10 s long pulses were 5.32 kV/mm, 2.96 kV/mm, and 1.18 kV/mm, respectively. Comparing this to that of the other reports, measured values are larger than the reported values of E_{cf} = 3.9 kV/mm, E_{cr} = 3.7 kV/mm and E_i = 0.1 kV/mm, respectively, at a voltage increase rate of 10 kV/mm/s, which is a faster ramp rate than our case.[6] This result might indicate a noticeable difference in the material composition.

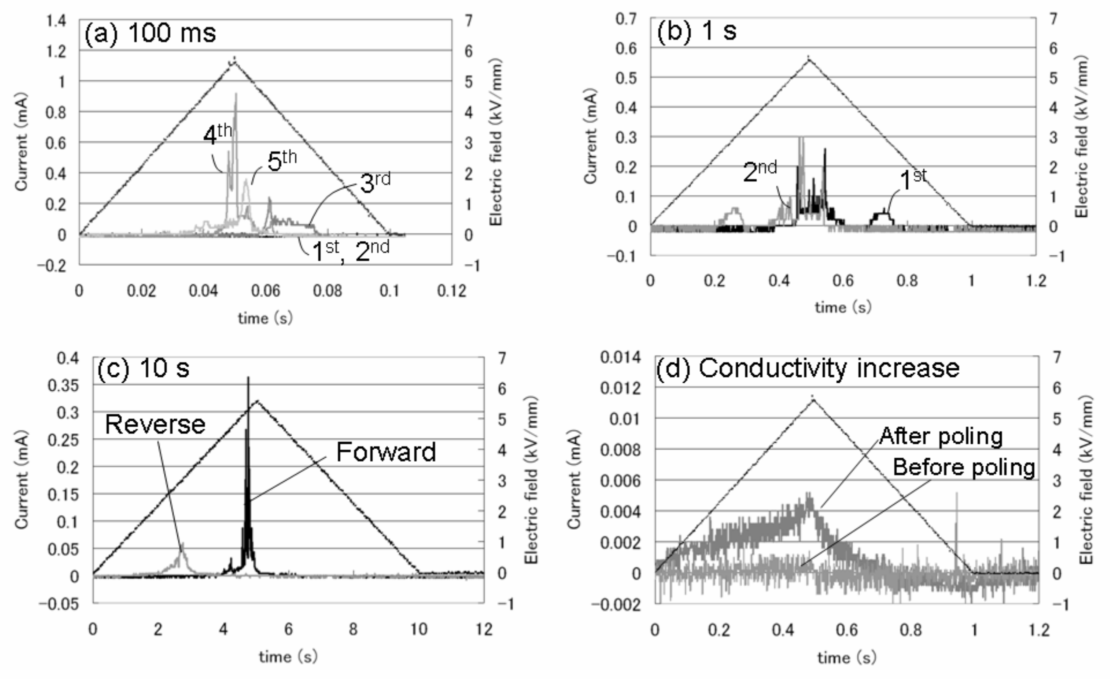

Figure 4-2-3. MgO:SLN switching properties. Triangular waveforms correspond to the applied electric field.

Concerning the slow switching time, similar results have been reported for MgO-doped congruent $LiNbO_3$, in which this delay time is often called incubation time.[7-9] The long incubation time might suggest that the MgO:SLN has a very large surface capacitance, C_s, which might make the domain switching be slow.

After having applied 10 triangular pulses in the forward poling direction, the conductivity increased only slightly. An example is shown in Fig. 4-2-3(d). This can be interpreted as a decreasing of the bulk resistance, R_B. This phenomenon was also observed for MgO-doped congruent $LiNbO_3$.[7-9] These increases of the conductivity was not observed in non-doped congruent $LiNbO_3$, which might be caused by the MgO doping. Based on the 10 s pulse width measurement, the value of P_s is expected to be approximately 90 μC/cm^2. This value is also larger than the reported value of 76.6 μC/cm^2,[6] a fact which might be due to the effect of the slightly increased conductivity.

MgO:SLT

The initial conductivity of MgO:SLT was also low and could not be measured with our equipment. Figure 4-2-4 shows the measured electric field and the current profile for different pulse lengths (100 ms and 1 s). In the case of the 100 ms pulse width, the switching current is clearly recognized; however, a small current flowed backwards after switching off of the electric field. This result is assumed to be related to the surface capacitance, C_s, which might be discharged with a short pulse length. It needed at least three pulses in order to completely pole under the electrode area. In the case of the 1 s pulse width, one pulse was enough to pole the whole area. In these experiments, it took more than several hundred seconds to stabilize the switched spontaneous polarization. The measured coercive fields (E_{cf}, E_{cr}) and the internal field, E_i, in the case of the 100 ms pulse were 3.44 kV/mm, 2.80 kV/mm, and 0.32 kV/mm, respectively, and, in the case of the 1 s pulse, they were 2.04 kV/mm, 2.00 kV/mm, and 0.02 kV/mm, respectively. The observed differences between the internal fields for the two cases seem to indicate a difference in the stabilization process of the new domains. Compared to the reported values of the coercive field (less than 1.7 kV/mm),[10] our measured values are similar or slightly larger. However, since the absolute value of the measured internal field is quite small by itself, the observed differences between the measured and the reported values might simply reflect the different measurement conditions. They might also depend on the sample stoichiometry at the micro-scale level and on the surface condition.

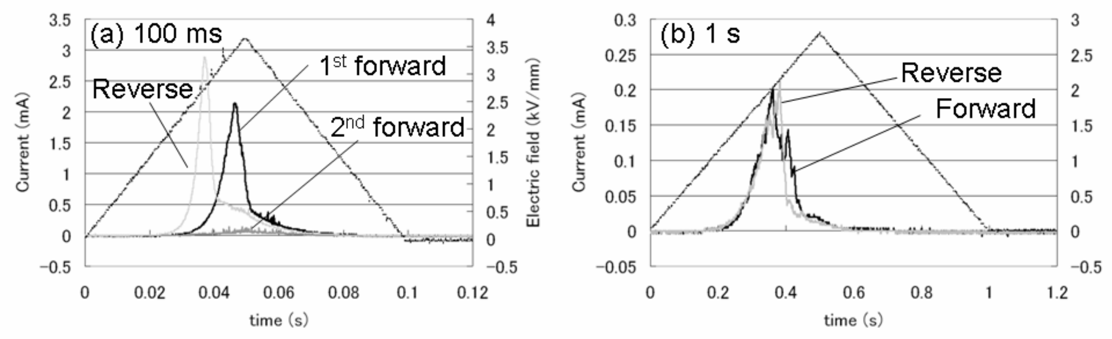

Figure 4-2-4. MgO:SLT switching properties.

The conductivity change in the material was different from sample to sample. Most of the samples did not show any remarkable increase of the conductivity after the poling process. The measured P_s value was approximately 50 to 70 μC/cm^2. The largest experimental error in comparison to the reported value (50 to 55 μC/cm^2) comes from the accuracy of the estimation of the poled area.[2]

SLT

As for the above case, the initial conductivity of the SLT samples was below the lowest detection limit and could, therefore, not be measured. Figure 4-2-5 shows the measured electric field and the current profile for different pulse lengths (100 ms, and 1 s). In the case of the 100 ms pulse width, again a small current flowed backwards after the switching off of the electric field. This current means that some of the poled area switched back to the original direction, the so-called backswitching current. This might also be related to the large surface capacitance, C_s, which remains after switching off of the electric field. It needed at least ten pulses in order to completely pole under the electrode area. In the case of the 1 s pulse width, a single pulse could pole the whole area. It might be because of an enough slow increase and decrease of the ramp rate of the applied electric field in order to compensate the charging and the discharging of the surface capacitance, Cs. The measured coercive fields (E_{cf}, E_{cr}) and the internal field, E_i, in the 100 ms pulse width case were 1.76 kV/mm, 1.48 kV/mm, and 0.14 kV/mm, respectively, and, in the 1 s pulse width case, they were 1.64 kV/mm, 1.32 kV/mm, and 0.16 kV/mm, respectively. These measured coercive fields are similar to the reported values. It is interesting to note that it seems to take a much longer time to stabilize the switched domains in the case of SLT although the E_c's of SLT is lower than that of the MgO:SLT. In addition, the measured current peak of SLT is much sharper than that of MgO:SLT. There might be several reasons for this: a) MgO:SLT might have less Li vacancy sites which will cause domain pinning; that might be expected from the observation of a larger number of spike pulse in the case of SLT, (those spike pulses are so-called the Barkhausen pulse which is related to the domain pinning),11) b) doping of MgO makes the crystal homogeneity worse hence the homogeneity of the nucleation might also be distributed as a function of the electric field in MgO:SLT. The conductivity did not increase in this case, and the measured P_s value of SLT was again approximately 50 to 70 μC/cm^2, quite similar to that of the MgO:SLT.

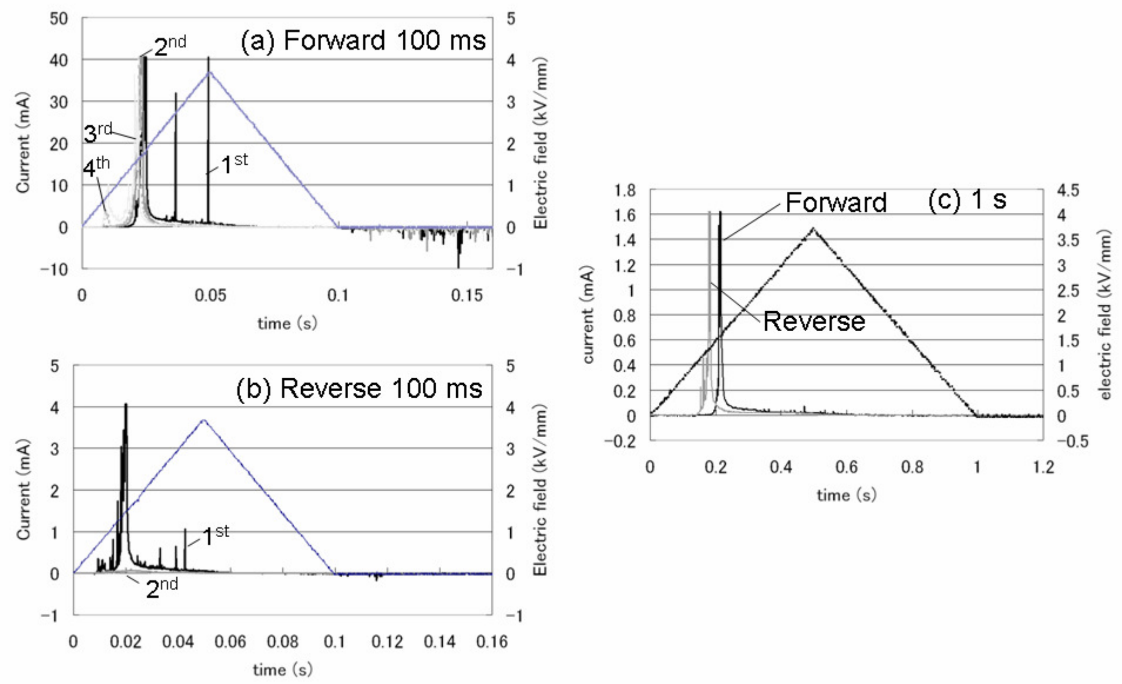

Figure 4-2-5. SLT switching properties.

4.2.3. KTiOPO$_4$ and its isomorphs $^{\text{Paper I)}}$

KTP

KTP has a high ionic conductivity as reported in a multiple of previous papers, see, for instance, Ref. 12. The conductivity depends on the method of the crystal growth. Generally, hydro-thermal grown KTP shows a lower conductivity than the flux-grown one does as shown in Fig. 4-2-6(a). The origin of this difference is not clear but could be associated with a lower K^+-mobility and/or a lower concentration of vacancies. In the case of the flux-grown crystal, there are typically conductivity distributions in the wafer as shown in Fig. 4-2-6(b). This variation is mainly related to the inhomogeneity of the K^+-vacancies, which probably is associated with a small temperature gradient during the crystal growth. The areas with the higher conductivity are corresponding to the higher densities of the K^+-vacancy.

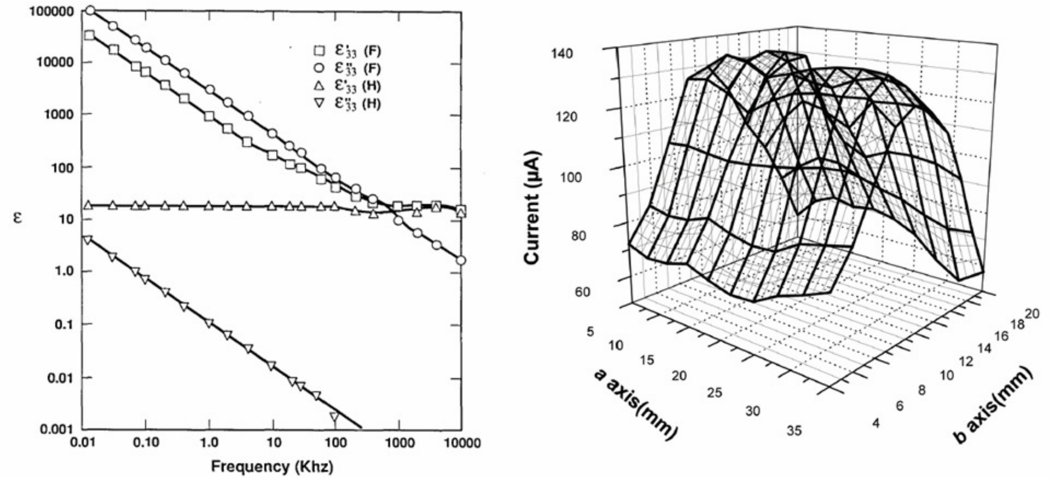

(a) (b)

Figure 4-2-6. (a): Frequency dependence of dielectric constant ε_{33}' and ε_{33}" for (F) flux-grown and (H) hydrothermally-grown KTP.[9)] *(b): Conductivity variation in flux-grown KTP wafer. The 100 μA level corresponds to a conductivity of approximately 8.5 X 10^{-7} S/cm.* $^{\text{Paper I)}}$

Since PPKTP can be made from any part of the flux-grown KTP wafer, two typical different parts of the wafer were investigated: 1) a relatively low conductive area whose conductivity was 6.8×10^{-7} S/cm (denoting LC-KTP) and 2) a high conductive area whose conductivity was 11.1×10^{-7} S/cm (HC-KTP). In order to measure the coercive field, 100 ms duration pulses were used, satisfying the condition as given by Eq. (4-2). Much longer pulse lengths would cause crystal breakdown because of its high conductivity. The measured current properties are shown in Fig. 4-2-7. Even with the high conductivities, the current peak can be clearly distinguished due to the switching of the spontaneous polarization. However, the conductive current component prevents the measurement of the P-E hysteresis loop. Since the current peak is almost symmetric, the position of the peak is taken to be the coercive field in this thesis. The coercive fields, E_{cf}, E_{cr}, and the internal field, E_i, for the measured samples were 2.20 ± 0.02 kV/mm, 2.12 ± 0.02 kV/mm, and 0.04 kV/mm, respectively, for the LC-KTP samples and 2.28 ± 0.02 kV/mm, 2.54 ± 0.02 kV/mm, and –0.13 kV/mm for the HC-KTP sample, respectively. The reason of the negative value of internal field in the case of HC-KTP can not be completely explained as yet and further studies will be needed in the future to clear this up. However, it might be related to the original spontaneous polarization state of the as-grown crystal, or to the differences of the screening current effect caused by the different conductivities of each state. The higher coercive fields in the HC-KTP cases suggest that the higher

K^+ vacancy concentration could also cause an increase in the internal fields in KTP, which would be similar to what is being observed in $LiNbO_3$ and $LiTaO_3$. Recently, K^+ ion enrichment into a flux-grown KTP wafer was performed by putting it into a melt-solution of KNO_3 at 350°C. That particular sample showed a much lower conductivity and possessed a much lower coercive field. This result also confirms that the coercive field is related to the number of K^+ vacancies.13)

Compared to MgO:SLN, SLT, and MgO:SLT, the switching time for KTP is rather short. It means that the surface capacitance, C_s, is lower which, again, might be associated with a higher bulk conductivity which makes it easier to fill in the surface charges.

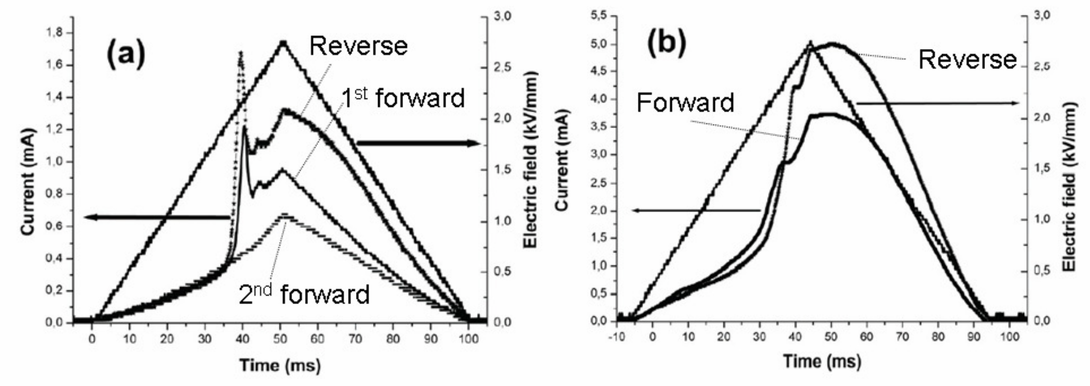

Figure 4-2-7. Coercive field measurement for KTP.Paper 1) (a): LC-KTP. (b): HC-KTP.

Due to the relatively high conductivity, it is difficult to directly measure the P_s value of KTP and its isomorphs. Since it is a known fact that the conductivity decreases at lower temperatures, it is possible to measure the P_s value in this case. Rosenman et al. have reported that the P_s value of KTP at 170 K is 27 μC/cm^2.14) Since the value of P_s decreases when increasing the temperature, it is expected that the P_s at room temperature is lower than 27 μC/cm^2. Thus, the P_s value of KTP is substantially lower than that of $LiNbO_3$ and $LiTaO_3$.

RTP

The coercive field of RTP was measured as shown in Fig. 4-2-8. Since the conductivity of RTP is much lower than that of KTP, the switching current peak is clearly shown. The coercive fields (E_{cf}, E_{cr}) and the internal field, E_i, were 6.00 ± 0.04 kV/mm, 5.50 ± 0.04 kV/mm, and 0.25 kV/mm, respectively. The measured value of E_{cf} was quite a bit higher than that which has been reported by Karlsson et al.15) and by Jiang et al.,16) however, the measurement methods were also different. This difference might reflect the fact that there were higher concentrations of Rb^+ vacancies in the investigated materials in the present study than in the other reports.15, 16) RTP is still an inconvenient material, one needs to determine E_{cf} on a new wafer before attempting QPM structuring.

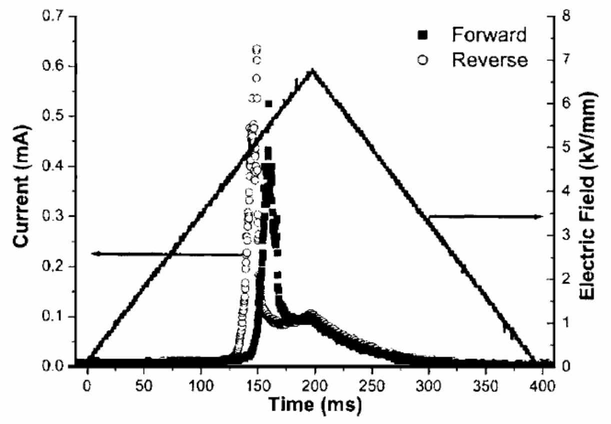

Figure 4-2-8. Coercive field measurement for RTP.$^{Paper\ I)}$

4.2.4. KNbO$_3$ $^{\text{Paper II, III)}}$

As mentioned in Section 3.3.3, KN has several spontaneous polarization directions at room temperature. In this section, two different types of domain switching phenomena are discussed separately: 1) 180°-domain switching whose spontaneous polarization directions are anti-parallel to each other and 2) non-180°-domain switching in which the spontaneous polarization directions are not anti-parallel.

180°-domains

The initial conductivity of KN is below our measurement limits. Figure 4-2-9 shows the measured electric field and the current profile for different pulse lengths (100 ms and 1 s). In both cases, one pulse is enough in order to pole the whole area under the electrode. The measured coercive field (E_{cf}, E_{cr}) and the internal field, E_i, in the case of 100 ms pulse width are 0.508 kV/mm, 0.456 kV/mm, and 0.026 kV/mm, respectively and, in the 1 s pulse case, 0.380 kV/mm, 0.316 kV/mm, and 0.032 kV/mm, respectively. When the pulse width was increased to 3 s,$^{\text{Paper II)}}$ those values were 0.260 kV/mm, 0.190 kV/mm, and 0.035 kV/mm, respectively and, thus, much smaller than those for the case of the shorter pulse width cases. The differences in the coercive fields which depend on the different ramp rate of the electric field might again be related to the surface capacitance, C_s. The measured values are also in this case lower than the reported values of E_{cf} = 0.552 kV/mm, E_{cr} = 0.214 kV/mm and E_i = 0.169 kV/mm.[17)] Since the measured internal field is much lower in our cases than the reported ones, the differences in the coercive field values might reflect the differences of the material stoichiometry. The conductivity did not change after the switching of the P_s direction (180° reversal). The measured P_s value was 38 μC/cm^2, which is almost the same as the reported value[18)] and less than for MgO:SLN, SLT, and MgO:SLT, but larger than that for KTP.

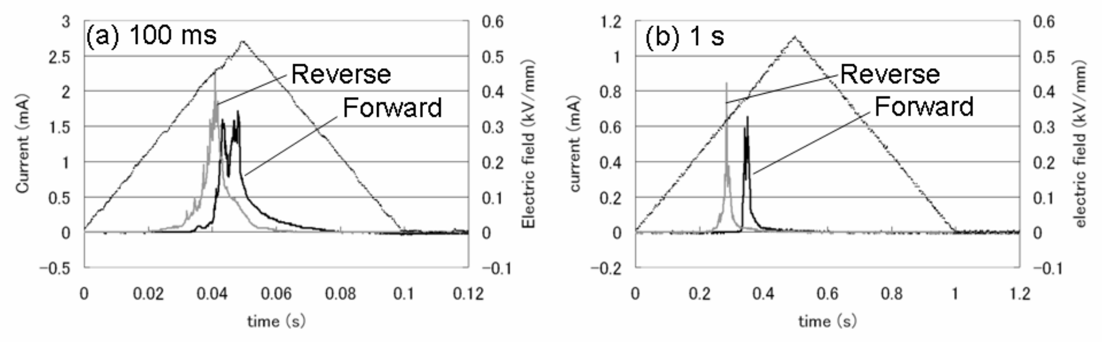

Figure 4-2-9. KN switching properties.

Non-180°-domains

Figure 4-2-10 shows the schematics of the four different types of domain pairs, viz, 60°-, 90°-, 120°-, and 180°- domain pairs. The first three domain pairs are usually considered as undesirable in many applications because they will cause unwanted scattering. Especially, it is considered a critical problem when those unwanted domain pairs such as the 60°- or 90°-domains, are simultaneously generated during the fabrication process yielding PPKN with 180°-domains. From another point of view, those other three domain pairs also have attractive possibilities in many optical applications if they can be reliably controlled by proper domain engineering. Therefore, it is both important and interesting to investigate the fabrication conditions of those alternative domain pairs.

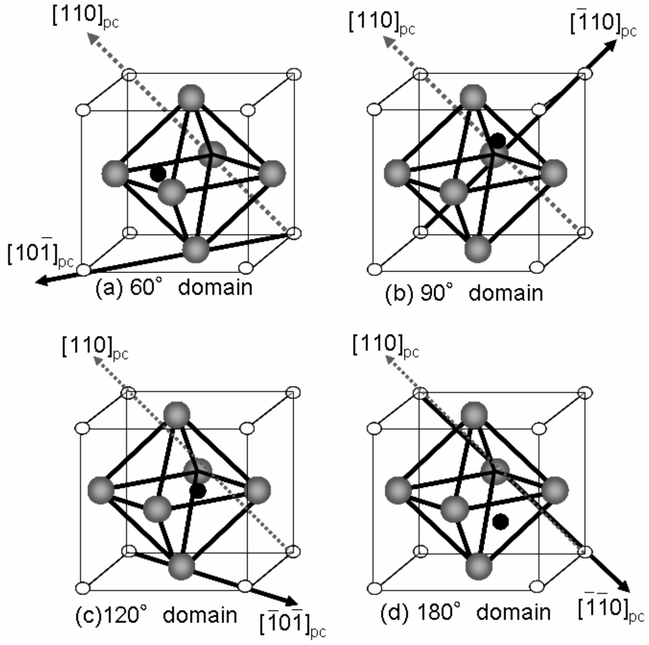

Figure 4-2-10. The schematics of the lattice structure compared to that of the original domain.[Paper III)]

In order to check the controllability of the various types of domain growth, 2-mm-thick samples cut with 9 different orientations were prepared as shown in Fig. 4-2-11. The detailed results are presented in Paper III. In the following, we will describe the most optimum poling conditions for the 60°- and 90°-domain fabrication, which is the termed differential vector poling (DVP) method as summarized in Table 4-2-1. In this method, the sample is poled in the direction which corresponds to the difference in the vector directions between the original and the intended spontaneous polarization directions: for the case of the 60°- and 90°-domain pairs, for instance, the directions are those of No. 8 and No. 4, respectively (See Fig. 4-2-11). For all of the samples, both of the main surfaces were optically polished and contacted by silver paste electrodes which were oriented parallel to the theoretical domain wall directions in order to reduce the generation of complex unwanted domains. The parallel side surfaces of the samples were also optically polished for in-situ monitoring of the domain generation processes using a video camera.

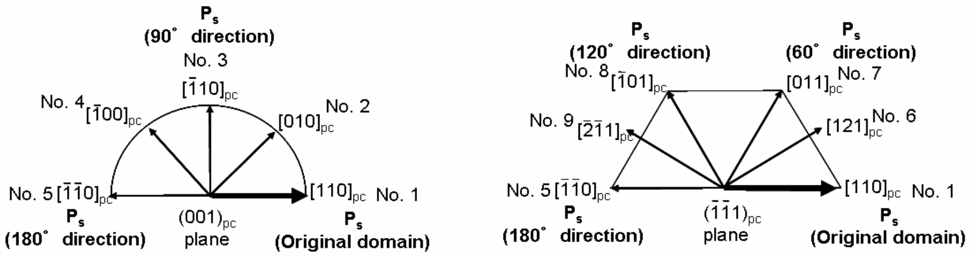

Figure 4-2-11. The cutting surface directions of the prepared KN samples. (The direction is also the same as for the poling direction.)$^{\mathrm{Paper\ III)}}$

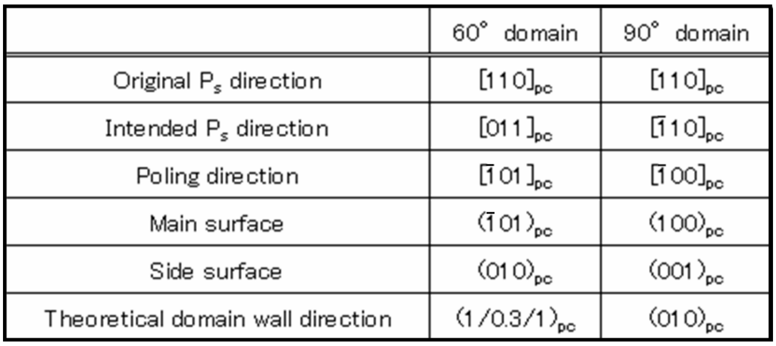

	60° domain	90° domain
Original P$_s$ direction	$[110]_{pc}$	$[110]_{pc}$
Intended P$_s$ direction	$[011]_{pc}$	$[\bar{1}10]_{pc}$
Poling direction	$[\bar{1}01]_{pc}$	$[\bar{1}00]_{pc}$
Main surface	$(\bar{1}01)_{pc}$	$(100)_{pc}$
Side surface	$(010)_{pc}$	$(001)_{pc}$
Theoretical domain wall direction	$(1/0.3/1)_{pc}$	$(010)_{pc}$

Table 4-2-1. Condition of differential vector poling (DVP) for 60°- and 90°-domain fabrication.

The experimental results show that the DVP direction is the optimum direction for controlling the arbitrary domain pairs. Here, we are focusing on the measured results of the DVP method for the 90°- and the 60°-domain pairs. In the case of the 90°-domain pair, the profile of the poling current is shown in Fig. 4-2-12(a). By monitoring the domain generation process by the video camera, we observed a multitude of domain walls generated under the electrode when the current peak was reached. After applying an electric field above the threshold for approximately 10 minutes, the generated domain walls slowly merged with each other and, finally, a very sharp and clear domain wall was obtained only at the edge of the electrode without any other domain generation. During the application of the electric field, the measured current decreased as the number of domain walls under the electrode decreased.$^{\mathrm{Paper\ A3)}}$ The total charge, Q, through the circuit was also more than 1000 times larger than that calculated from the spontaneous polarization changes. This result suggests that the conductivity of the domain wall region might be higher than that of the bulk single crystal area.

The 60°-domain walls were generated when a field of approximately 240 V/mm was applied as shown in Fig. 4-2-12(b). Since the domain switching was finished within 300 ms, the switching speed or the domain wall propagation speed of the 60°-domain is at least 100 times faster than that of the 90°-domain. After the circuit current peak has passed, no residual domain walls were observed and the current went down to zero again. This result suggests that the apparent conductivity could be very low, as in bulk KN, and all of the domain walls, under the electrode, were completely removed.

Using the measured P_s value in the c-direction, as mentioned above, the partial elements of the spontaneous polarization for the $[10\bar{1}]_{pc}$ direction is estimated to be 19 μC/cm^2 (38 μC/cm$^2\times$cos 60°). On the other hand, the change in the P_s value was calculated as 15 μC/cm^2 from the observed Q value and the associated poled area A, based on Eq. (4-1). This value is roughly in agreement with the theoretically estimated value (approximately 80% of the estimation). That is, almost all of the current in the circuit should have been a result of the spontaneous polarization change.

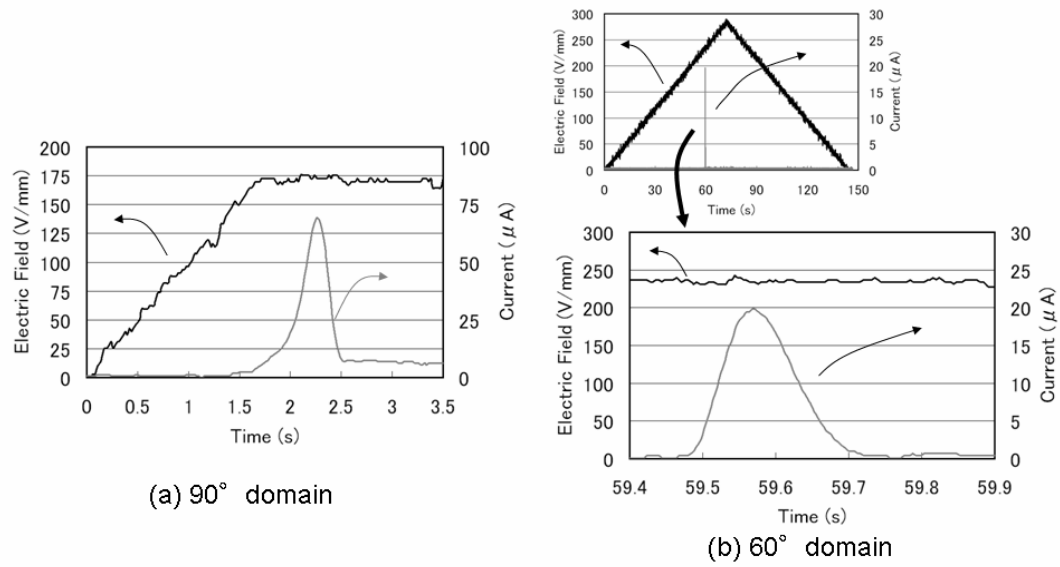

(a) 90° domain

(b) 60° domain

Figure 4-2-12. The voltage and current profile of (a) 90°-domain and (b) 60°-domain generation in KN.$^{\textit{Paper III)}}$

Comparing all of the coercive fields in the 60°-, 90°-, and the 180°-domain pairs, it is evident that the 90°-domains had the lowest coercive field. In order to explain the differences, the piezoelectric constants in each of the applied electric field directions were investigated. The detailed calculations are mentioned in Paper III. The calculations show that the value of the piezoelectric constant for the applied electric field directions of the 60°-, 90°-, and 180°-domain pairs are 6.50, 8.71, and 3.05 $\times 10^{-11}$ C/N, respectively. Normally, the piezoelectric response is largest for the direction parallel to the $\boldsymbol{P_s}$ direction; however, this is not the case for KN. The piezoelectric constant is basically related to the amount of displacement of each ion in the material. That is, since the displacement of the ions at the same applied electric field is the largest for the 90°-domains configuration, the expected threshold electric field for the 90°-domains should be the lowest. This expectation is in good agreement with our measured results.

4.2.5. Dependence of the coercive field on the number of poling cycles

The values of the coercive fields are typically discussed only in the case of the initial forward and reverse poling cycle. That is because, normally, only the first forward poling process is used in the QPM fabrication process. However, it was interesting to see how the coercive field varies by a repetition of the poling process. In all of the investigated cases, except for the RTP, the coercive field decreased after repetitions of the poling as shown in Fig. 4-2-13. The exact values of the coercive field depend on the pulse length and on how quickly the switching back and forth is performed. The coercive fields of the forward poling were decreased more than that of the reverse poling after the repetition.

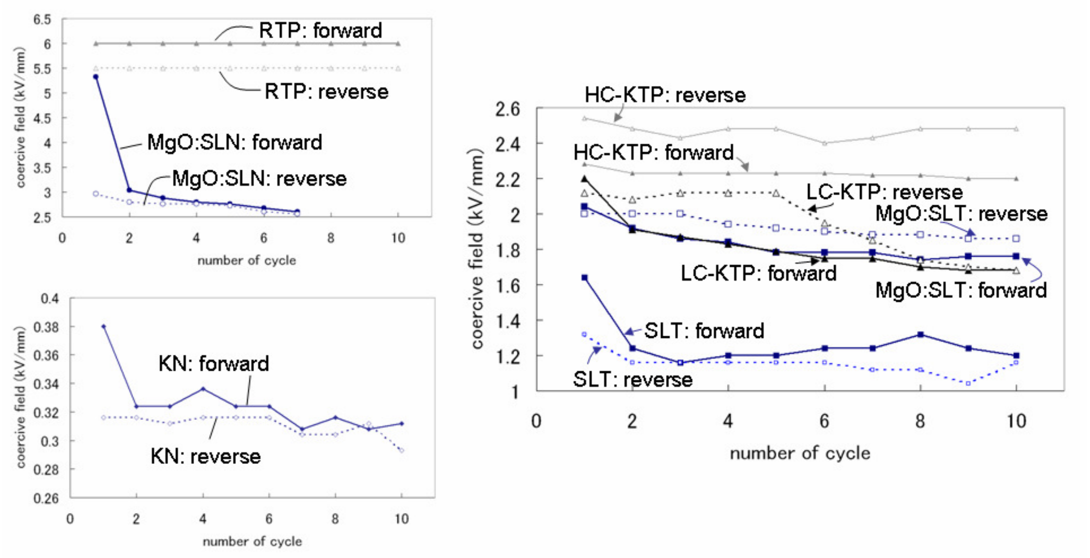

Figure 4-2-13. The coercive field dependence on the number of poling cycles.

The most interesting thing to note is the threshold of the switching, as shown in Fig. 4-2-14. Typically, the width of the switching current becomes broader and the current starts to flow at a much lower voltage compared to the first forward poling cycle. That fact might also make it easier to switch the spontaneous polarization compared to the first forward poling. The possible reasons for this reduction might be 1) earlier nucleation due to the creation of dead layer at the sample, 2) partial

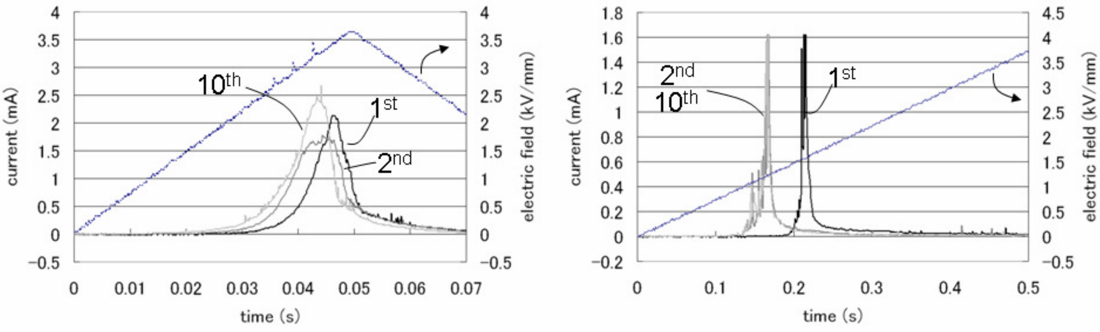

(a) MgO:SLT 100 ms (b) SLT 1 s

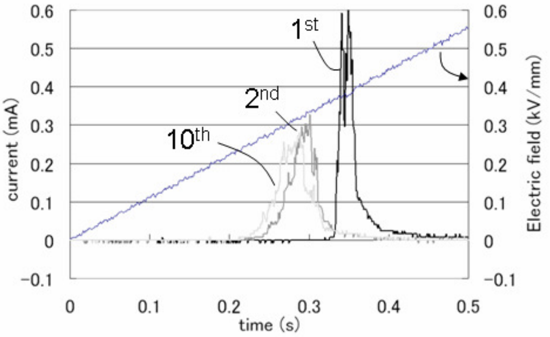

(c) KN 1 s

Figure 4-2-14. The differences for the forward poling process of the first, second, and tenth repeated cycles.

annealing of the pinning cracks will make the movement of domain wall possible at lower electrical energy. Some parts of these sources might also cause a reduction of the surface capacitance, C_s, and the surface resistance, R_s, hence, the coercive fields after a repetition of domain switching were also decreased. In the case of PPKN fabrication, this effect was employed as shown in the next chapter. By switching the orientation too many times could, however, sometimes cause material breakdown. Especially in the case of MgO:SLN, this material cannot tolerate extensive domain switching repetitions, and it is easy to generate cracks at the edges of the electrodes as is shown in Fig. 4-2-15.

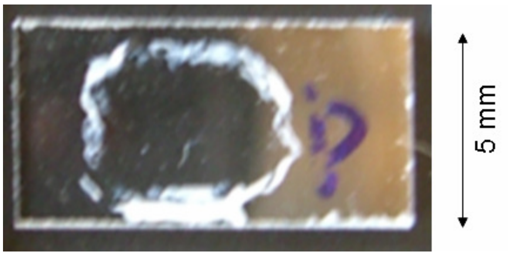

Figure 4-2-15. Material breakdown in MgO:SLN after the 7th poling cycle.

4.3. Domain morphology

4.3.1 Domain characterization method

Since there is no difference in the refractive indices between the poled and the unpoled 180°-domain structures, it is rather difficult to visualize the differences between the domain structures by using a conventional optical microscope. There are, however, several other methods that have been used in order to visualize these domain morphologies: a) atomic force microscope (AFM) with a piezoelectric response,19) b) non-linear optical microscope,20) c) scanning nonlinear dielectric microscope,21) and d) etching techniques when using strong acids or alkalis. Even though the first three methods are non-destructive methods, they are not suitable for observing the micro- to macroscopic QPM structures. The etching technique, which employs the difference between the etching rate of the $+P_s$ and the $-P_s$ surfaces, is destructive but a very simple and useful characterization method. Even though this technique is destructive, there are not a problem for bulk QPM applications because the etched area is only located at the polar surface with less than 1 μm etching depth and no particular destructions of the optical surfaces (the *X*-surfaces for LN and LT, the *a*-surfaces for KTP and its isomorphs, and the *b*-surfaces for KN). Thus, the characterizations of the domains in this work were mainly carried out by the etching technique method. 40 to 50% hydrofluoric acid were employed as an etchant for the $LiNbO_3$, $LiTaO_3$, and $KNbO_3$ materials, and a mixture of $KOH:KNO_3$ for the $KTiOPO_4$ crystals.

4.3.2. $LiNbO_3$ and $LiTaO_3$

The domains of MgO:SLN, MgO:SLT, and SLT materials tend to acquire a hexagonal shape as shown in Fig. 4-3-1. The apexes correspond to the ± *Y* directions and the sides are perpendicular to the ± *X* directions. On the other hand, congruent $LiTaO_3$ has been reported to have either triangular or hexagonal shapes whose apexes correspond to the X-axis. These hexagonal shapes could reflect the basic crystal symmetry which is originally a hexagonal structure above the Curie temperature; however, the reason why the domain wall direction is different in the case of congruent $LiTaO_3$, has not been well explained yet.10) Due to the morphology of the three investigated materials, the QPM grating vectors should be chosen to be parallel to the *X* direction.

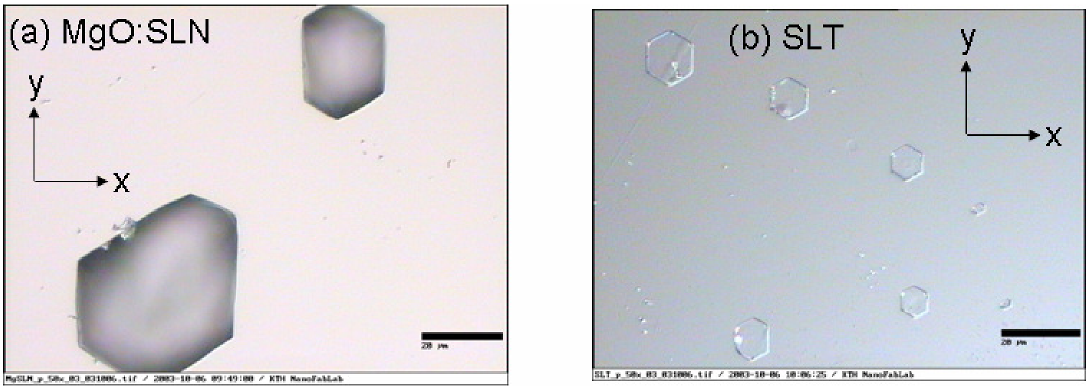

Figure 4-3-1. The domain morphology of MgO:SLN, SLT and MgO:SLT. Inside the hexagonal areas are etched −z domain and the other parts are less-etched +z domain.

4.3.3. KTiOPO$_4$ and its isomorphs Paper I)

The domains of KTP tend to spread out in a rectangular shape as shown in Fig. 4-3-2. The domain spreading speed in the *b*-direction is faster than that for the *a*-direction. According to Bierlein et al.,22) the Ti-O chains oriented along the (011) and the (011) directions contribute to the *c*-directed polarization. Since the (100) plane does not intersect the Ti-O chains, the domain walls parallel to the (100) planes (i. e, perpendicular to the *a*-direction) will be preferred. Its isomorphs also show the same anisotropy. Due to this anisotropy, the QPM grating vectors should be chosen parallel to the *a*-axis.

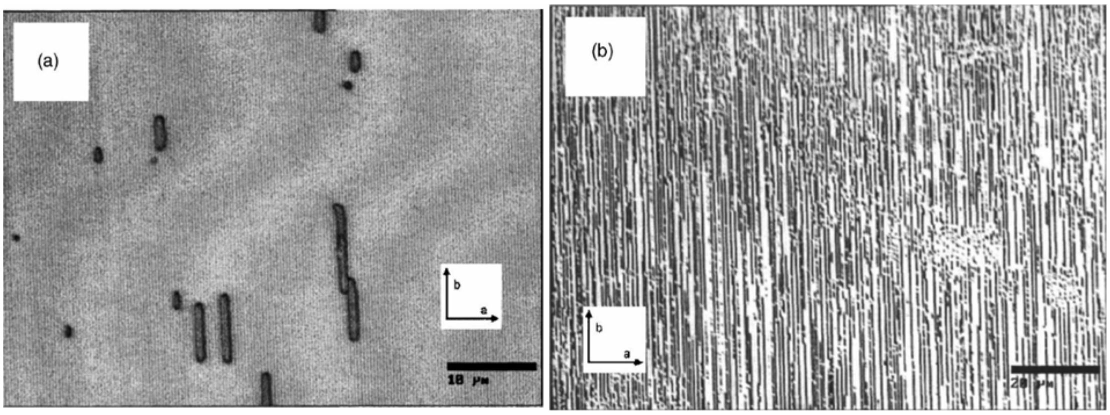

Figure 4-3-2. Domain morphology of KTP.Paper I)

4.3.4. KNbO$_3$ Paper III, IV)

180°-domains

The domains in KN tend to acquire rectangular shapes as shown in Fig. 4-3-3. The domain spreading speed in the *a*-direction is faster than that for the *b*-direction. This anisotropy has not been explained in detail yet. A plausible explanation relates to the relatively strong bonding along the *b*-axis. That is because, as shown in Fig. 3-3-11, the *b*-axis ($[001]_{pc}$ axis) is never expanding during the phase transition and it is shorter than the other pseudo-cubic axes. By another approach we investigated the origin of this anisotropy by focusing on the change of the positions of the atomic ions before and after a 180°-domain switching. Figure 4-3-4 shows the distances of each ion as projected onto two different planes [(a): the *a*-*c* and (b): the *b*-*c* plane] before and after a domain switching. The distances between each ion are calculated as based on neutron diffraction data as reported in Ref. 23. The niobium ions only move parallel to the *c*-direction and the pseudo-cubic lattice structure of the potassium ions does not change its shape before and after the domain switching. Thus, the displacement component of the oxygen octahedron is most important. In order to eliminate the displacement in the *c*-direction, we have considered only the displacements in the *a*-, and the *b*-directions away from the base planes (*b*-*c* and *a*-*c* plane, respectively) on which the niobium ion is located (as shown by the gray bar in Figs. 4-3-4). The displacements of each ion with respect to the *a*- and the *b*-axes are summarized in Table 4-3-1.

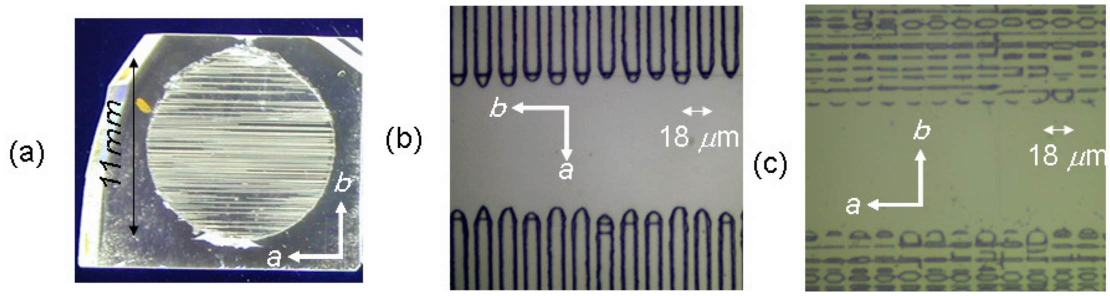

Figure 4-3-3. Anisotropic domain propagation in 180°-domain switching. All samples are etched after poling. Picture (a) is the sample which is poled without patterned electrode. Picture (b) and (c) are the samples which are poled with the periodic electrode patterns formed perpendicular to the b- and the a-direction, respectively. The periodicity of pattern is 18 μm.

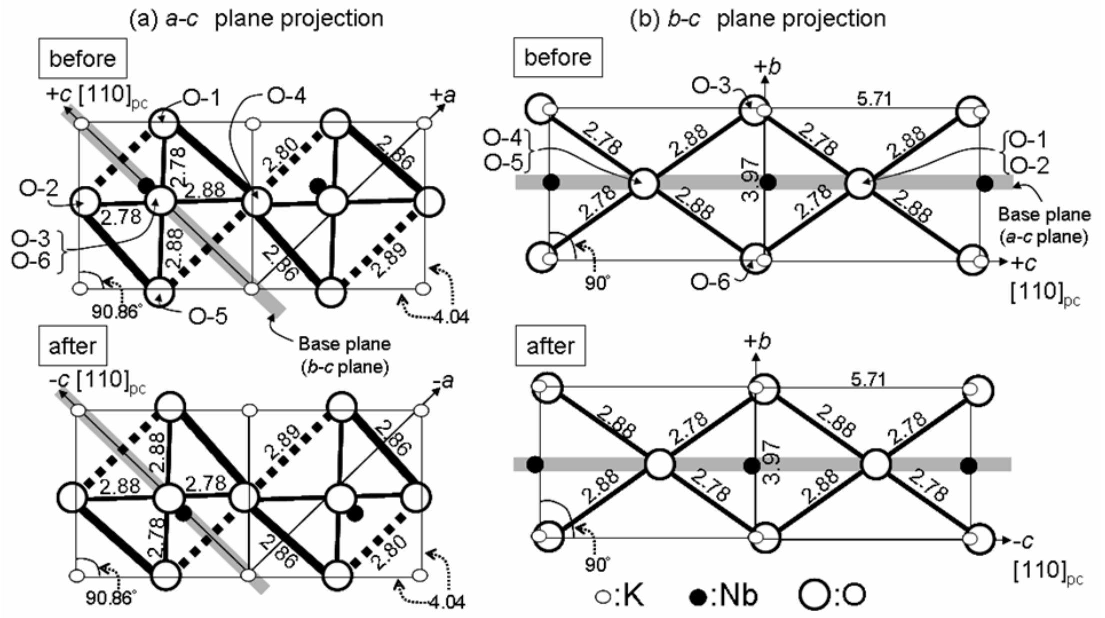

Fig. 4-3-4. Ion position changes before and after 180°-domain switching. (a): The a-c plane projections (b): The b-c plane projections The unit of distances is Å. All ion positions were exaggerated in order to see the differences of the domains clearly. The gray bars indicate the base plane in order to calculate the oxygen ion displacements to the a-, and b-axes. Small open circles, large open circles, and the solid circles indicate the K-, O-, and the Nb-ions, respectively.

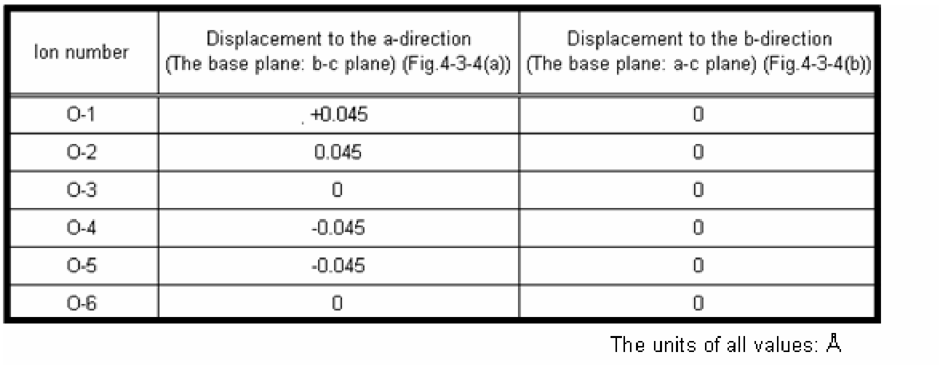

Ion number	Displacement to the a-direction (The base plane: b-c plane) (Fig.4-3-4(a))	Displacement to the b-direction (The base plane: a-c plane) (Fig.4-3-4(b))
O-1	+0.045	0
O-2	0.045	0
O-3	0	0
O-4	-0.045	0
O-5	-0.045	0
O-6	0	0

The units of all values: Å

Table 4-3-1. Displacement of the oxygen ions to the a-, and b- directions before and after 180°-domain switching. Each ion number is corresponding to the number in Fig. 4-3-4. Displacement is defined as the distance changes between each ion position and the base plane before and after domain switching.

As shown, there is no displacement in the *b*-direction, which means that each oxygen ion only shifts parallel to the *c*-direction in the *b-c* plane projection. On the other hand, the four oxygen ions are displaced in the *a*-direction. This is also clearly recognized from the positions of the oxygen ions (O-1, O-2, O-4, and O-5, respectively). Following this reasoning, the small lattice miss-match in the *b*-direction would actually allow the existence of a stable domain wall along the normal to the *b*-axis in adjacent domains. Contrary, the large lattice miss-match in the *a*-direction would require a high energy concentration at the domain wall. The domain wall can then become unstable and propagate easily along the *a*-axis direction. These theoretical considerations can actually support our experimental results of a much faster domain wall velocity along the *a*-axis direction than in the *b*-axis direction. From this anisotropy, the QPM grating vector should be chosen parallel to the *a*-axis.

Non-180°-domains

Domain wall directions between two adjacent domains were theoretically investigated by Fousek et. al.[24)] Weisendanger[25)] also have investigated the domains for KN in detail and classified the possible domain structures. The possible domain wall directions for 90°- and 60°-domain walls are the $[101]_{pc}$ and $[1/0.3/1]_{pc}$ directions, respectively. Since the refractive index changes at the non-180°-domain walls, it is possible to characterize the domains by optical methods employing the differences in the birefringence. It is also possible to confirm the domain structure by measuring the surface profiles of the samples using, for example, scanning-probe microscope because the switched area is tilted to the non-switched area at a certain angle which should satisfy the continuity condition of the domain boundary which van be calculated from the lattice constants.

The wall directions of the 60°- and the 90°-domain pairs were confirmed by various means by using optical microscopy, X-ray diffraction analysis, and surface profiles by scanning-probe microscope as shown in our papers[Paper III, IV, A1, A3)]. The fabricated domain wall directions of both the 60°- and the 90°-domain pairs are coincident with the theoretical direction of the uncharged domain walls. The most important differences of the morphology between the 180°-domains and the non-180°-domains are that, since the wall direction is only permitted in a specific direction in the non-180°-domain case, these domain walls must be created from the top to the bottom and from the one edge to another edge of the sample. Otherwise, unwanted domains are also generated at the edges of the poled area. On the contrary, the 180°-domains can be created only at the middle of the samples.

4.4. Summary

The measured coercive fields and the morphologies of the different materials are summarized in Table 4-4-1. The coercive fields are also plotted in Fig. 4-4-1 as a function of the increased rate of the electric field. These parameters are quite important when optimizing the periodic poling conditions as described in the next chapter. The coercive fields in KN are much lower than that of the other measured materials. The coercive fields of KTP, MgO:SLT, and the SLT are relatively similar. MgO:SLN and RTP have higher coercive fields. Considering the domain switching dynamics, we can conclude that MgO:SLN has the longest nucleation time and, therefore, a time much longer than 1 s is required for switching the $\boldsymbol{P}_s$ in this case. Newly switched domains in SLT and MgO:SLT have to be stabilized as revealed by the backswitching current after a 100 ms poling pulse. On the contrary, the stabilization time of KN and KTP and its isomorphs might be short.

pulse width		MgOSLN	MgOSLT	SLT	LC-KTP	HC-KTP	RTP	KN
0.1-0.2s	E_{cf}	none	**3.44**	**1.76**	**2.20**	**2.28**	**6.00**	**0.508**
	E_{cr}		2.80	1.48	2.12	2.54	5.50	0.456
	E_i		0.32	0.14	0.04	−0.13	0.25	0.026
1 s	E_{cf}	none	**2.04**	**1.64**	breakdown	breakdown	–	**0.380**
	E_{cr}		2.00	1.32				0.316
	E_i		0.02	0.16				0.032
3 – 10 s	E_{cf}	**5.32**	–	–	breakdown	breakdown	–	**0.260**
	E_{cr}	2.96						0.190
	E_i	1.18						0.035
morphorogy		hexagonal	hexagonal	hexagonal	rectangular	rectangular	rectangular	rectangular
proper grating vector direction		X	X	X	a	a	a	b

Table 4-4-1.Comparison of the fundamental domain switching properties. The unit of the coercive field is kV/mm. 'none': not enough duration time, '-': not measured

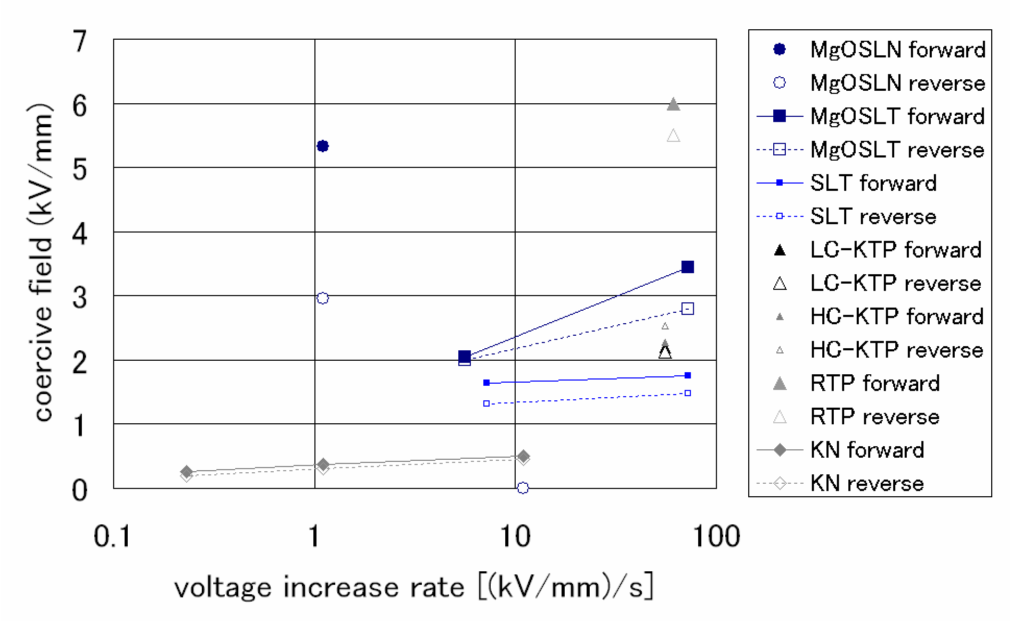

Figure 4-4-1. Comparison of the coercive field as a function of the increase rate the electric field.

References in Chapter 4

1) For example, L. F. Schloss, and P. C. McIntyre: J. Appl. Phys. **93**, 1743 (2003).

2) K. Kitamura, Y. Furukawa, K. Niwa, V. Gopalan, and T. E. Mitchell: Appl. Phys. Lett. **73**, 3073 (1998).

3) V. Gopalan, T. E. Mitchell, Y. Furukawa, and K. Kitamura: Appl. Phys. Lett. **72**, 1981 (1998).

4) D. Natali and M. Sampoetro: J. Appl. Phys. **92**, 5310 (2002).

5) H. C. F. Martens, W. F. Pasveer, H. B. Brom, J. N. Huiberts, and P. W. M. Blom: Phys. Rev. B **63**, 125328 (2001)

6) K. Hodoyama, M. Maruyama, Y. Kato, H. Nakajima, Y. Nomura, S. Kurimura, and K. Kitamura: The 8th international symposium on ferroic domains and micro- to nanoscopic structures (ISFD-8), Tsukuba, Japan, (2004), P01-21.

7) A. Kuroda, S. Kurimura, and Y. Uesu: Appl. Phys. Lett. **69**, 1565 (1996).

8) K. Nakamura, J. Kurz, K. Parameswaran, and M. M. Fejer: J. Appl. Phys. **91**, 4528 (2002).

9) K. Mizuuchi, A. Morikawa, T. Sugita, and K. Yamamoto: Electron. Lett. **40**, 819 (2004).

10) T. Hatanaka, K. Nakamura, T. Taniuchi, H. Ito, Y. Furukawa, and K. Kitamura: Opt. Lett. **25**, 651 (2000).

11) A. G. Chynoweth: Phys. Rev. **110**, 1316 (1958).

12) J. D. Bierlein and H. Vanherzeele: J. Opt. Soc. Am. B **6**, 622 (1989).

13) C. Canalias: "Domain engineering in $KTiOPO_4$", Ph. D thesis, Chapter 8, ISBN 91-7178-152-8, Royal Institute of Technology, (2005).

14) G. Rosenman, P. Uremski, A. Arie, M. Roth, N. Angert, A. Skliar, and M. Tseitlin: Appl. Phys. Lett. 76, 3798 (2000).

15) H. Karlsson, F. Laurell, and L. K. Chen: Appl. Phys. Lett. **74**, 1519 (1999).

16) Q. Jiang, A. Lovejoy, P. A. Thomas, K. B. Hutton, and R. C. C. Ward: J. Phys. D **33**, 2831 (2000).

17) J. H. Kim and C. S. Yoon: Appl. Phys. Lett. **81**, 3332 (2002).

18) P. Gunter: J. Appl. Phys. **48**, 3475 (1974).

19) C. Canalias, V. Pasiskevicius, A. Fragmann, and F. Laurell: Appl. Phys. Lett. **83**, 734 (2003).

20) S. Kurimura and Y. Uesu: J. Appl. Phys. **81**, 369 (1997).

21) Y. Cho, S. Kazuta, and H. Ito: Appl. Phys. Lett. **79**, 2955 (2001).

22) J. D. Bierlein and F. Ahmed: Appl. Phys. Lett. **51**, 1322 (1987).

23) A. W. Hewat: J. Phys. C: Solid State Phys. **6**, 2559 (1973).

24) J. Fousek and V. Janovec: J. Appl. Phys. **40**, 135 (1969).

25) E. Weisendenger: Czech. J. Phys. B **23**, 91 (1973).

Chapter 5. Fabrication and characterization of periodically-poled devices Paper II, V, VI)

5.1. Introduction

In this chapter, I want to show how difficult (or easy) it is to fabricate PP structures. Unfortunately, there is no single set of perfect conditions in order to fabricate QPM structures in arbitrary samples, so the conditions have to be optimized for each material and sometimes even for every sample. That is due to the different material properties and the different device designs: sample size, presence of micro domains, non-perfect homogeneity, different grating periods, etc. In addition, there are many control parameters in the QPM structure fabrication: the magnitude of the electric field, the pulse shape, the pulse duration, the poling circuit configuration, the electrode structure, etc. Thus, although there are many previous reports on different fabrication conditions, the detailed conditions have not always been perfectly described. That is why all researchers and companies in this area have their own recipes for fabricating QPM structures. As a result, the prices of these devices are still relatively high. Among the parameters above, the most critical issue might be the material homogeneities, which makes it difficult to fabricate QPM structure with good reproducibility.

In the following, a typical periodic-poling procedure and a model for the the periodic domain growth are described in Section 5.2. In Section 5.3, the poling system used in this study is described. In Section 5.4, the optimized recipes for the investigated materials are described and compared with each other. At KTH, department of laser physics, substantial effort has been developed in understanding the ferroelectric domain growth in KTP and its isomorphs and the optimizing poling conditions for different periodicities. The experience has showed that the consistency in initial material properties is of utmost importance. This work has resulted in sub-μm periodic structuring in KTP.1) In this work we focus on extending this expertise to relatively new ferroelectric crystals, MgO:SLN, SLT, MgO:SLT, and KN, which have certain advantages for short wavelength devices, and also non-180°-domain structures in KN. Presently, the optimized recipes at KTH are achieved for a 30 μm periodicity for MgO:SLN, MgO:SLT, SLT, and KN. The results presented in this thesis give some idea for future development in the fabrication of PP devices with even smaller periodicities. In Section 5.5, the nonlinear optical conversion properties of the fabricated PP devices are characterized in an OPO experiment. Also, a new configuration of QPM by using a PP structure composed of 90°-domains of KN is demonstrated.

5.2. Periodic-poling procedure

The schematic of a typical poling procedure is shown in Fig. 5-2-1. First, we cut the wafer into small pieces whose sizes are typically 5×10 mm to 10×20 mm and with a 1 mm thickness. Then, the side surfaces are polished to an optical finish in order to monitor the process by using a suitable laser. After that, the + P_s side of the surface is determined by using a piezoelectric tester (American Piezo Ceramics, Inc. Pennebaker Model 8000 Piezo d_{33} tester). Then, the samples are cleaned and a 2 μm layer of positive photoresist (S1818) is spun onto one of the polar faces. The photoresist is then soft-baked for 90 s at 120°C and exposed through a photolithographic mask using a g-line of Hg lamp and the pattern is developed. Afterwards, an aluminum thin film (50-100 nm) is evaporated onto the top of the photoresist pattern. Finally, the samples are poled by applying an electric field and the PP structures are finally obtained. After the poling, since there are remnant stresses in the switched domains, these samples are annealed at a temperature higher than 100°C. Some materials need additional processing steps due to their specific properties, which will be described in the following sections.

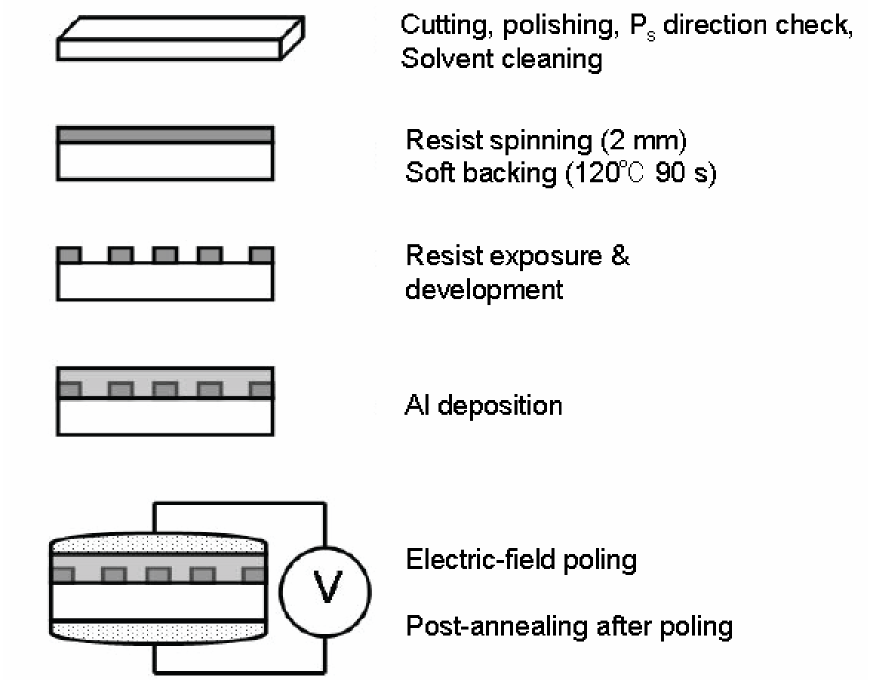

Figure 5-2-1. Schematics of the steps involved in the fabrication process of the QPM structure.

The typical sequences of ferroelectric domain generation by electric field poling is described in the papers. Phenomenologically, the domain growth proceeds as follows; first the opposite orientation domains will nucleate at the two edges of each electrode where the field is the strongest. Then the nuclei will propagate to the opposite crystal surface. Afterwards the domains will merge horizontally

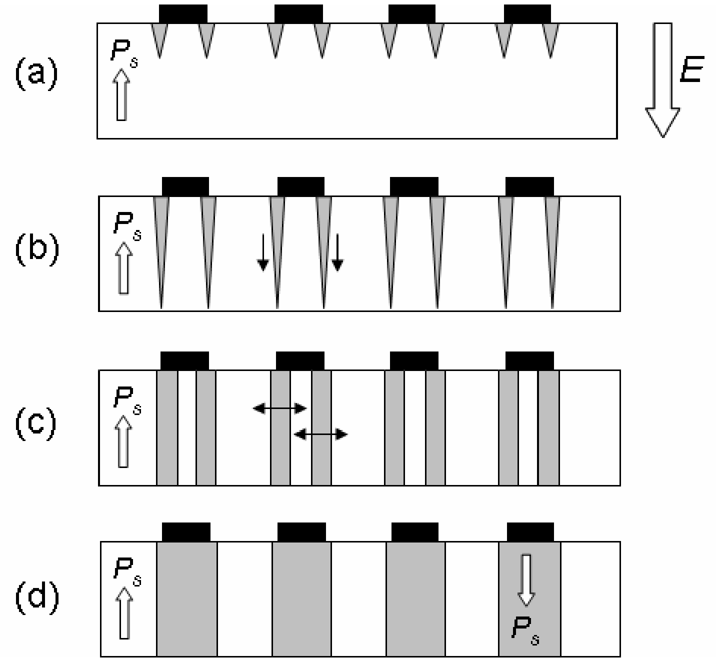

Figure 5-2-2. Model of the periodic-poling process. (a): Nucleation, (b): Domain growth in depth direction, (c): Sidewise domain growth, and (d): Stabilization of the domains

under each electrode. And finally, the new domains will stabilize (as shown in Fig. 5-2-2).[2)] In general, the nucleation process needs higher energy than the other three processes. In low conductivity ferroelectrics such a MgO:SLN, SLT, MgO:SLT, and KN, the stabilization of newly grown domain structure can take certain amount of time during which the capacitances associated with the surface and possibly domain tips are uncharged. If the stabilization time is not long enough, the unstable domains will switch back to the original state; a phenomenon called backswitching. This sequence of events is typically observed when a pulse with electric field higher than the coercive field is employed for poling. However, the latter three processes seem to vary slightly and, furthermore, they depend on the electric field strength, the number of pulses, and the serial resistances in the electric circuit.

5.3. The poling setup

The poling setup consists of an electric circuit and a process monitoring system based on using lasers. The poling circuit employed is shown in Fig. 4-2-1 and the schematic of the process monitoring system is shown in Fig. 5-3-1. Apart from just providing an electric field pulse of predetermined shape and amplitude, the set up has to provide means of monitoring of poling process, possibility to control domain spreading by circuit modification. Needless to say is that the homogeneity of the electrical contact with the sample is of at utmost importance. These points are described below.

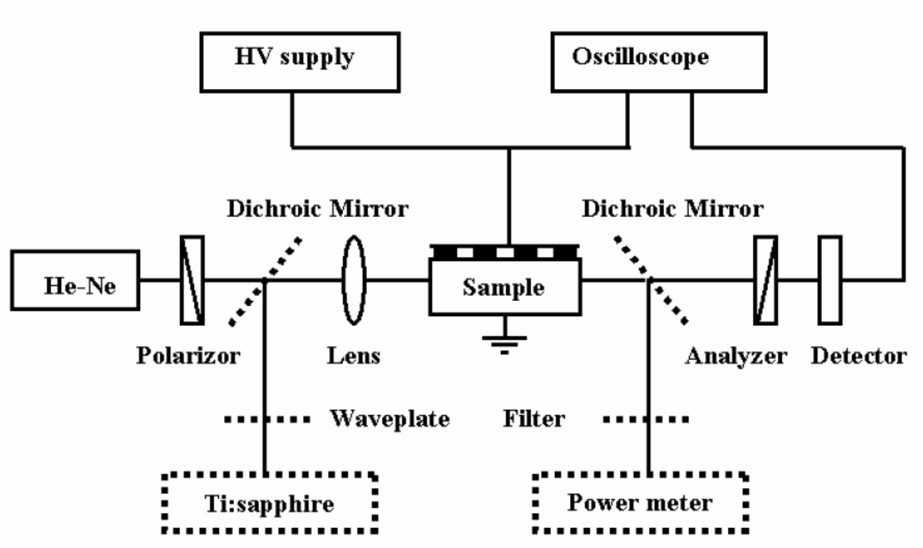

Figure 5-3-1. Schematics of the process monitoring system.

5.3.1. The process monitoring method

Three process monitoring methods are used in order to optimize the fabrication conditions. The first one is based on the monitoring the electric charge transport through the current flow. This method works well for low conductivity materials such as MgO:SLT, SLT, and KN. To obtain the charge flow accurately, it is important to remove any background noise, which can vary quite substantially. In the case of poling by using many pulses, or in the low current regime, the accuracy then becomes low and this method of monitoring does not work so effectively. In addition, the charge information alone does not give information on the uniformity of the poling area. So, even though the flow integrated charge could correspond to the half of area poled, [that is $Q = 2P_sA/2$ based on Eq. (4-1)], in principal, half the area can be over-poled while the remaining half of the area will stays unpoled.

The second monitoring method is based on monitoring the electro-optic (E-O) effect.[3)] In this technique, a He-Ne laser probe beam, which is linearly polarized at 45° to the P_s direction, propagates along the grating vector. When the domains grow through the crystal, the output polarization state changes accordingly. This change is detected by a second polarizer aligned orthogonally to the first one, together with a photodiode. This method is very useful as it gives us average information of the domain growth and it works effectively when the samples are homogeneously poled. However, since it monitors only one spot at a time, it is impossible to characterize the complete uniformity over the whole periodicity of the sample. (In principle, one can use a wide beam and a CCD to monitor the whole structure.)

The third method used in this work is direct second-harmonic (SH) monitoring by utilizing Ti:Sapphire laser. In this particular work, the SH power was compared with theoretical estimate after each poling pulse, providing most useful information on when to stop the poling pulse sequence. For single-pulse poling, a time-resolved detection can be utilized. In addition, to the quality of the QPM structure this method also give information about the QPM homogeneity over the aperture of the sample.

5.3.2. Effect of the serial resistance

As shown in Section 4.2, the current flow for the P_s switching has a peak value when applying a triangular pulse form of the electric field. A current peak is also observed when applying a constant electric field. In general, therefore, once the nucleation starts, the current suddenly increases due to polarization current component given by, $2P_s \partial A_i / \partial t$. Since the nucleation probability is different from sample to sample, the current flow pulse shape and amplitude at the same applied electric field will also be different. To increase reproducibility of the poling, a high serial resistance (R_1 in Fig. 4-2-2) improving limited-current region is typically used. The relation between the voltage at the sample (V_{sample}), the amplifier voltage (V_{set}), and the current flow (i), is given by

$$V_{sample} = V_{set} - R_1\, i \quad . \qquad (5\text{-}1)$$

Thus, by using a higher resistance value of R_1, the V_{sample} is correspondingly reduced by increasing the current i. As a result, the poling process is slowed down or can even be terminated because of the reduced V_{sample}. A typical effect of the current limitation with a high serial resistance is shown in Fig. 5-3-2. In the low serial-resistance case, the voltage at the sample is almost constant and the current flow is varying. On the other hand, in the case of a higher resistance, the voltage at the sample decreases when the current increases. As a result, the current is kept constant at the lower level. By using this technique, it is possible to reduce the poling speed, thus, the controllability of the poling now becomes easier.

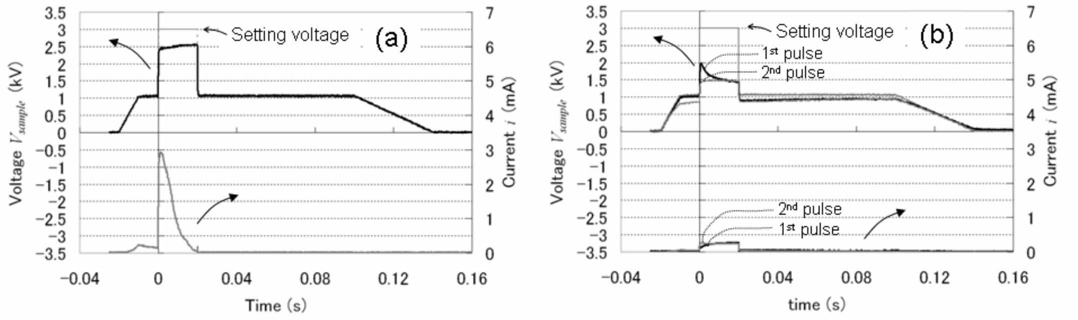

Figure 5-3-2. Voltage and current profiles for different serial resistance conditions. (a): R_1 = 45 kΩ, (b): R_1 = 5 MΩ. Higher resistance values will suppress both the current, i, and the voltage at the sample, V_{sample}.

The effects of the current limitation with different serial resistances (5 to 50 MΩ) are compared as shown in Fig. 5-3-3. As can be seen, the effect is of course larger when using a higher resistance. However, the relation between the voltage at the sample, V_{sample}, and the current, i, is almost the same. That means the current density is the same at a certain voltage at the sample V_{sample}. Current limiting, however, does not work so well in the routine fabrication of PPKTP because the V_{sample} is reduced too much by the conductive current, thus preventing domain switching. In the work of this thesis, the R_1 = 5 MΩ was used as a high serial resistance value and R_1 = 0 or 15 kΩ was used as a low serial resistance value for voltage-limited poling regime.

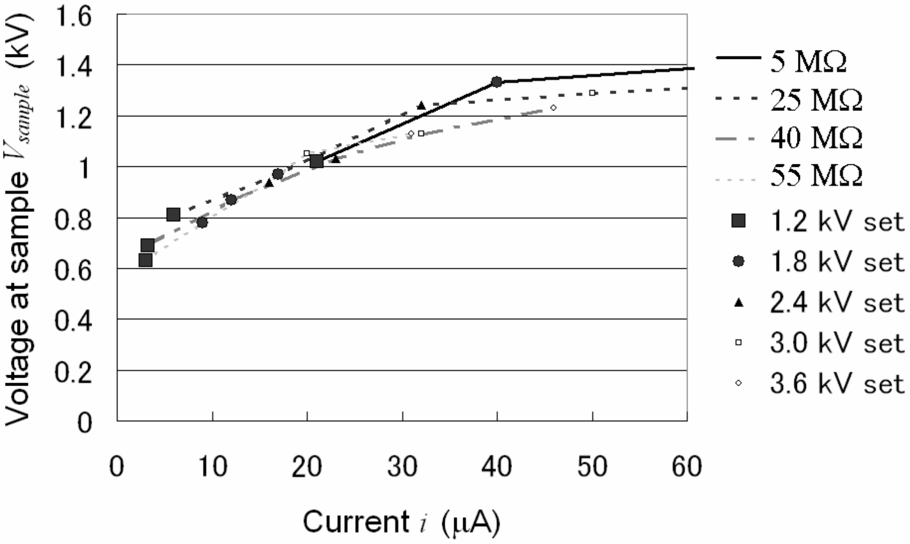

Figure 5-3-3. Relation between the applied electric field and the saturated current in different serial resistances.

Although the V_{set} and the V_{sample} of Eq. (5-1) are different in each case, and depend on the serial resistance, the poled area size, and the current density of the material, most of the reports in literature only indicate the applied total voltage, V_{set}. As our discussion above shows, that makes it difficult to verify the results of previous reports.

5.3.3. Electrode structures

There are mainly two major considerations in choosing the electrode structure: the duty ratio and the electrode material. Since the electric field is highest at the edge of the electrode,4) the area of the switched domain can easily become wider than the width of the electrode as shown in Fig. 5-2-2. To make a periodically-poled structure with 50:50 duty cycle, the electrode pattern should be made narrower than 50% of the whole period. The appropriate duty cycle will strongly depend on the material and on the periodicity of the pattern.

Several types of electrode materials have been used: a liquid electrode (saturated LiCl or KCl solution), an electrode gel (Spectra 360 Electrode gel, Parker Laboratories INC.), and metal electrode. In general, since metal coated on the sample surfaces facilitates nucleation process, the Al film is coated above the photoresist in this study. Two different types of sample holders have been also used, as shown in Fig. 5-3-4. The holder, marked type A, holds a sample at its edge by silicone rubber and is filled by a liquid electrode inside the silicone rubber square. In the holder of type B, Cu foil is in direct contact with the Al metal contact. The electrode gel is coated onto the un-patterned surface in order to make a uniform contact between the sample surface and the Cu foil. The latter structure improves the homogeneity of periodic-poling in the MgO:SLN, MgO:SLT and the SLT (as described in the next section).

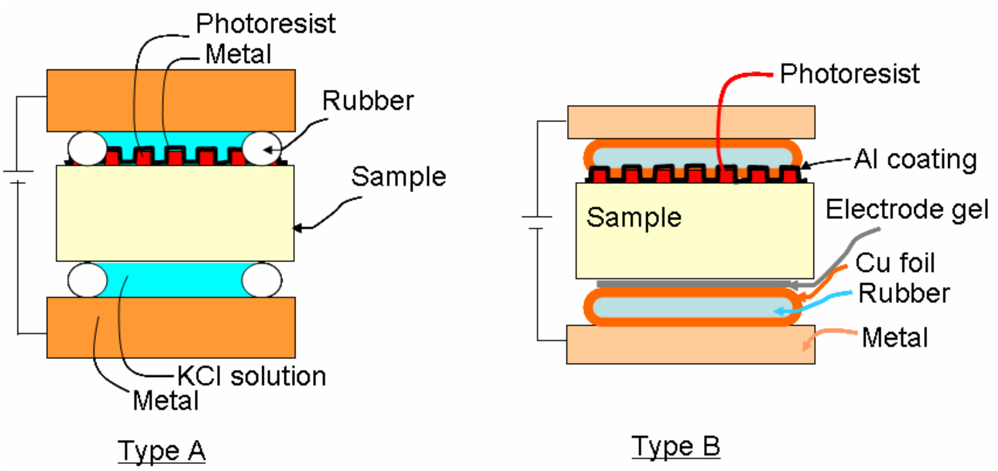

Figure 5-3-4. Two different types of electrode holder. Type A: Sample clamped by silicone rubber at the edges of the crystal and filled with a KCl liquid electrode as electrode contact. Type B: Sample clamped by silicone rubber which was wrapped in Cu foil. Electrode contacts are provided by direct contact with the Cu foil and Al electrode on the pattered side and the electric gel on the un-patterned side.

5.4. Fabricating conditions of periodically-poled ferroelectrics

As it has already been established the electric-field poling involves several processes with different activation energies: domain nucleation, domain propagation along the polar direction, and domain broadening perpendicular to the polar direction. Following domain growth, the domain stabilization has to be done in some cases, especially for the low-conductivity ferroelectrics. The domain nucleation is the most critical stage in controlling the homogeneity of the whole QPM structure. The nucleation homogeneity can be controlled, to a large degree, by ensuring uniform conditions on the sample surface and a uniform low-resistance contact with the circuit. The fidelity of the QPM structure, on the other hand, can be controlled by using a proper contact-pattern geometry and monitoring the current flow through the circuit, the electro-optic modulation, and/or the SHG signal as described above. In the following the detailed procedures are outlined of domain growth as well as the results we obtained using these procedures. Moreover, the optimization necessary for short-period QPM fabrication are outlined and our initial results are provided.

5.4.1. Stoichiometric $LiNbO_3$ and $LiTaO_3$

MgO:SLN

Previous reports

Periodic poling conditions for MgO:SLN in previous publications are summarized in Table 5-4-1.[5-8] Basically, two techniques have been utilized: applying an electric field above or below the coercive field, E_c. The higher electric field technique has been employed for the standard congruent $LiNbO_3$.[4] For MgO:SLN, Maruyama et al. have fabricated a 70 mm long periodically-poled structure by applying electric field lower than the E_c with multiple pulses.[5)] Huang et al. has by applying electric field slightly higher than the E_c poled MgO:SLN uniformly, but the well-poled area was only 2 mm long and 5 mm wide.[6)] In the other papers the poling conditions were not clearly defined.[7-8)] From studying the first two reports, it seems advantageous to pole at a lower electric field than E_c. It might be related to a higher surface capacitance, C_s, which can be charge compensated even by applying electric field below E_c as is shown in Fig. 4-2-3.

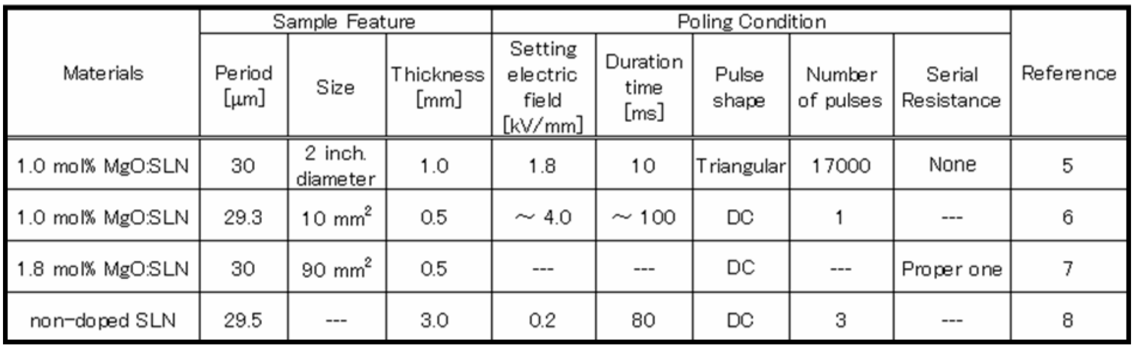

Materials	Sample Feature			Poling Condition					Reference
	Period [µm]	Size	Thickness [mm]	Setting electric field [kV/mm]	Duration time [ms]	Pulse shape	Number of pulses	Serial Resistance	
1.0 mol% MgO:SLN	30	2 inch. diameter	1.0	1.8	10	Triangular	17000	None	5
1.0 mol% MgO:SLN	29.3	10 mm^2	0.5	~ 4.0	~ 100	DC	1	---	6
1.8 mol% MgO:SLN	30	90 mm^2	0.5	---	---	DC	---	Proper one	7
non-doped SLN	29.5	---	3.0	0.2	80	DC	3	---	8

Table 5-4-1. Reported poling conditions for MgO:SLN. '---': not mentioned in the paper.

Nucleation control

Purchased wafers usually have micro domains nucleated by processing procedures like polishing because of the relatively low coercive field of the materials. Thus, it is important to remove those micro domains before we start periodic poling and to avoid generation of new micro domains during the soft-baking process (described below in the MgO:SLT and SLT section in detail).

When the type A sample holder was employed, homogeneous QPM structures could not be obtained. Although some other previous reports have described similar electrode structures,[5-7)] our own results always showed poor uniformity of the structure in this case as shown in Fig. 5-4-1.

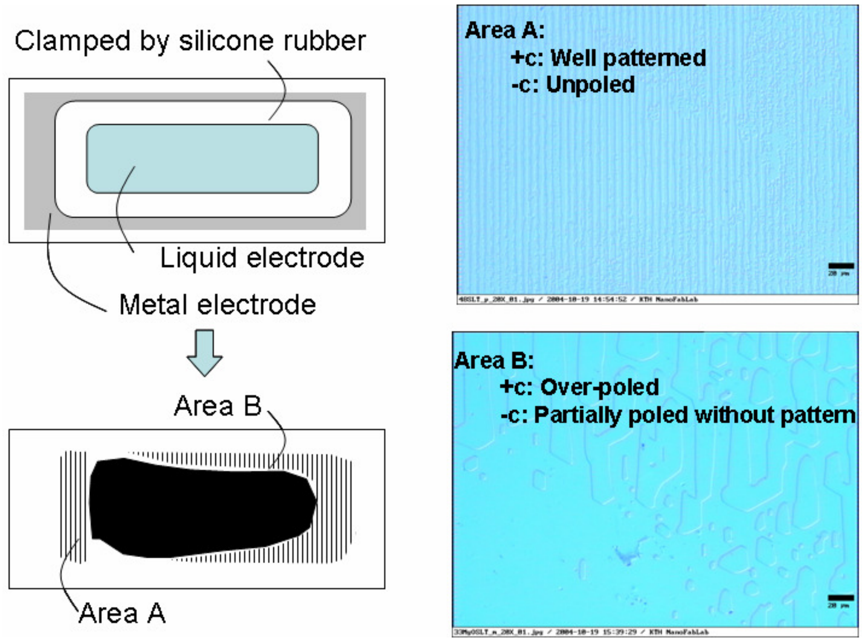

Figure 5-4-1. Schematics of a less uniform PP structure in the stoichiometric materials poled using a type A electrode holder.

That might be so because of the differences in the actual electric field with- and without-clamping by silicone rubber.

To increase the contact uniformity and resistance, the sample holder type B was used. This electrode holder gives a much better homogeneity; probably because of the uniform pressure and uniform electrical contact under the whole electrode area.

Optimizing the periodic domain growth

The duty cycle of the electrode:photoresist = 30:70 was used for the 30 μm QPM period samples. For the 6 μm period, a ratio of 30:70 was also tested but the created domains merged with each other for all of the poling conditions. Thus, shorter period requires much narrower electrode width. At the same time, the increasing influence of the fringing fields would probably require domain growth at even lower applied electric field.

Based on the report in Ref. 5, triangularly shaped pulses with 10 ms duration were tested for several samples. The maximum electric field varied between 1.2 and 2.4 kV/mm, which is still much lower than the coercive field of 5.3 kV/mm. Both low and high serial resistances were tested but the difference was not observed because of low current poling and the short pulse duration. Thus, poling in this material was performed in the voltage-limited regime. Since the switching area of each pulse is very small in this low field poling regime, no remarkable backswitching current was observed. The optimum number of pulses was different from sample to sample, and, typically, more than 150,000 pulses were needed. The stopping points were decided by monitoring the direct SH signal. The results for the fabricated PPMgO:SLN are shown in Fig. 5-4-2. As can be seen, the un-patterned side of the crystal is still of lower homogeneity; however, the periods with 30 μm are clearly recognized over the whole poled area of a size of approximately 3 mm×8 mm. PPMgO:SLN were fabricated with much lower voltage than the coercive field with multiple short pulses due to low activation energy of domain propagation along polar direction.

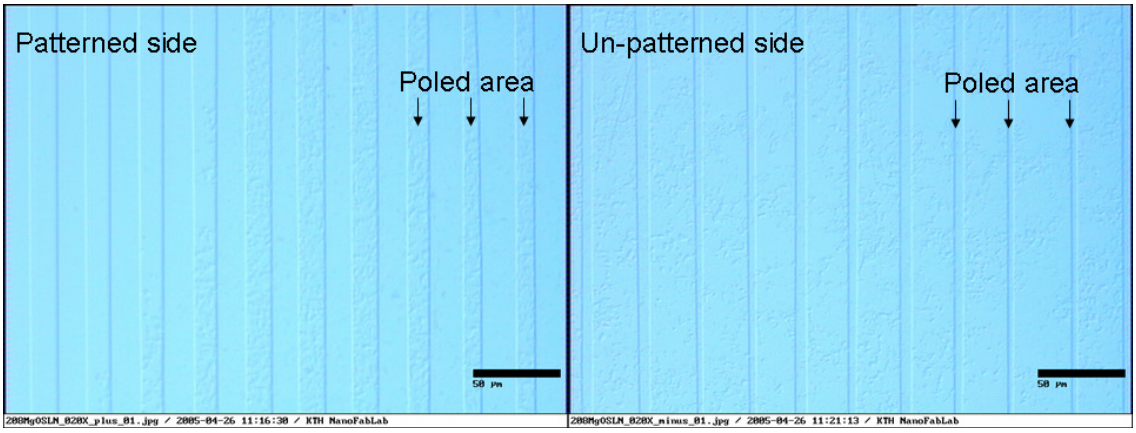

Figure 5-4-2. PPMgO:SLN.

MgO:SLT and SLT

Previous reports

The reported poling conditions for MgO:SLT and SLT are summarized in Table 5-4-2.[9-16] Detailed conditions are only described in Ref. 9. In almost all reports a charge monitoring technique was used. For a 30 μm period, successful poling by applying electric-field above E_c were obtained (Ref. 9).

That might mean that the domains do not merge because of a limited domain broadening occurs. In addition, higher electric field gives a higher current that makes the resolution of the charge flow monitoring technique better. On the other hand, for shorter period (<10 μm) successful demonstrations have only been obtained by applying electric-field lower than E_c. That might suggest that the domain broadening still becomes critical in the short period regime and, thus it is important to keep a low electric field then.

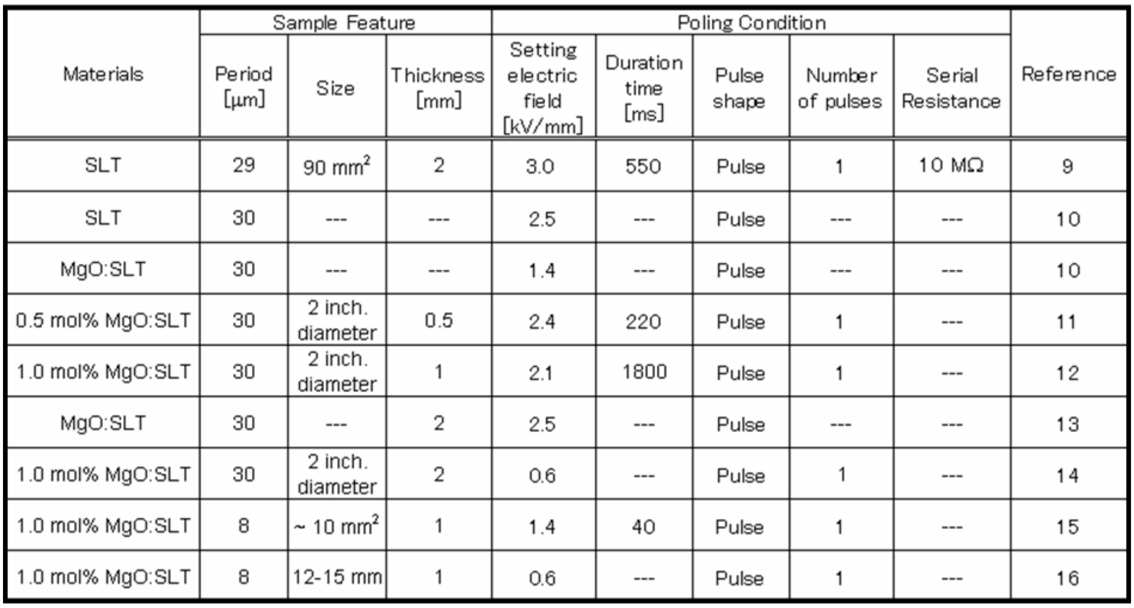

Materials	Sample Feature			Poling Condition					Reference
	Period [μm]	Size	Thickness [mm]	Setting electric field [kV/mm]	Duration time [ms]	Pulse shape	Number of pulses	Serial Resistance	
SLT	29	90 mm^2	2	3.0	550	Pulse	1	10 MΩ	9
SLT	30	---	---	2.5	---	Pulse	---	---	10
MgO:SLT	30	---	---	1.4	---	Pulse	---	---	10
0.5 mol% MgO:SLT	30	2 inch. diameter	0.5	2.4	220	Pulse	1	---	11
1.0 mol% MgO:SLT	30	2 inch. diameter	1	2.1	1800	Pulse	1	---	12
MgO:SLT	30	---	2	2.5	---	Pulse	---	---	13
1.0 mol% MgO:SLT	30	2 inch. diameter	2	0.6	---	Pulse	1	---	14
1.0 mol% MgO:SLT	8	~ 10 mm^2	1	1.4	40	Pulse	1	---	15
1.0 mol% MgO:SLT	8	12-15 mm	1	0.6	---	Pulse	1	---	16

Table 5-4-2. Reported poling conditions for SLT and MgO:SLT. '---': not mentioned in the paper.

<u>Nucleation control</u>

The purchased wafers of SLT and MgO:SLT also displayed micro domains as shown in Fig. 5-4-3(a). These were, however, easily removed by the applying electric field parallel to the major P_s direction [This is called pre-poling treatment, as shown in Fig. 5-4-3(b)]. From photographs of the etched crystal and the value of the switching current, the total micro domain area in the as-purchased wafer was estimated to be 3 to 7% of the total wafer area. Those micro domains will cause disturbances in the photoresist layer during the soft-baking process as shown in Fig. 5-4-3(c). Thus, a pre-poling treatment is very important. Even after the pre-poling treatment is properly performed, micro domains can still easily be generated during the soft-baking process because of the pyroelectric effect. To avoid this, the temperature has to be increased slowly up to 120°C and then decreased down to room temperature slowly for this processing step. The same careful treatments should be used for MgO:SLN wafers.

<u>Optimizing the periodic domain growth</u>

A duty ratio of the electrode:photoresist of 30:70 was also used for the 30 μm period samples and the sample holder type B was effectively working for SLT and MgO:SLT also. Both low and high serial resistances were tested in our experiment and we found that the high serial resistances gave much more controllable domain growth. The pulse shape we used is shown in Fig. 5-4-4. This shape has four stages: stage I with slowly increasing voltage to avoid large displacement current; stage II mainly involved in the P_s switching by having a constant voltage; stage III used to stabilize the

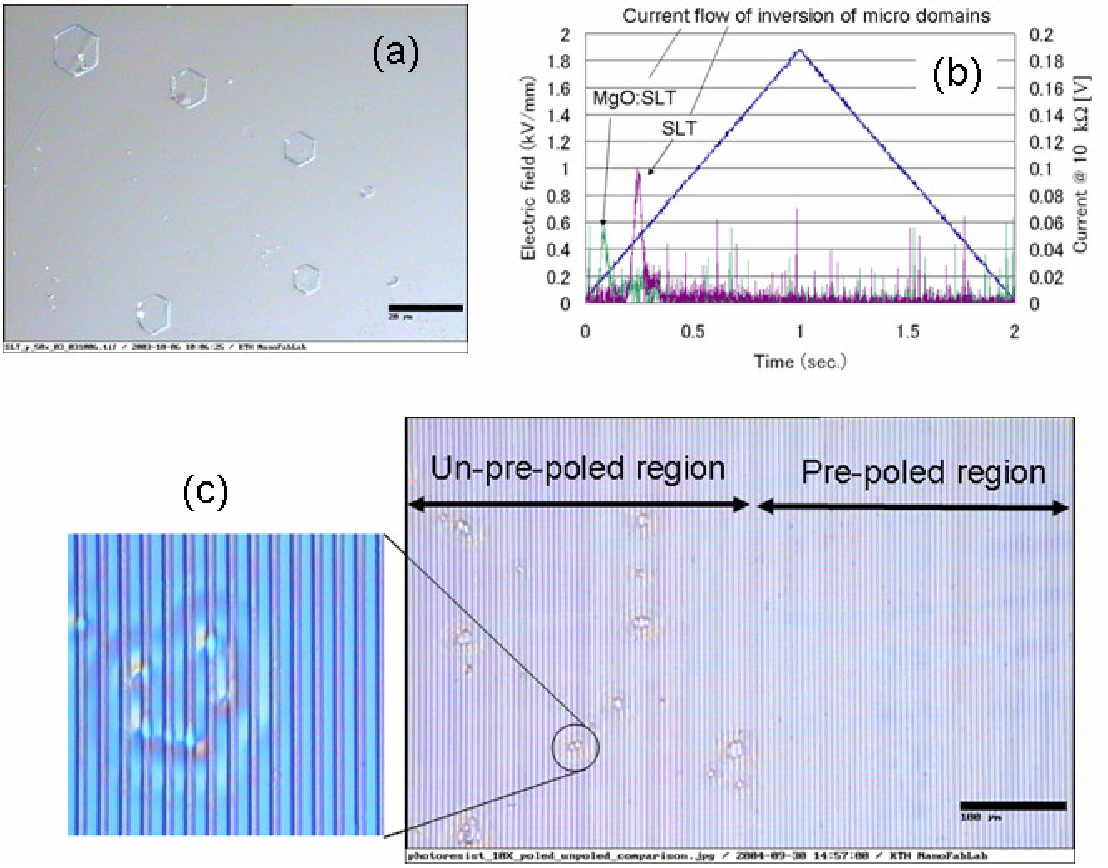

Figure 5-4-3. Micro domains in as-purchased wafers. (a) Etched picture, (b): Observed current of the micro-domain switching, (c): Photoresist disturbance caused by the micro domains.

newly oriented domains and to avoid backswitching; and stage IV with slowly decreasing the voltage not only to avoid the still remaining risk of backswitching but also for monitoring of the structure by the E-O effect. In stage II, different conditions of applied electric fields were tested corresponding to the amplifier voltage between 0.8 kV/mm and 2.4 kV/mm with pulse length varying from 25 ms to 250 ms duration of the stage II.

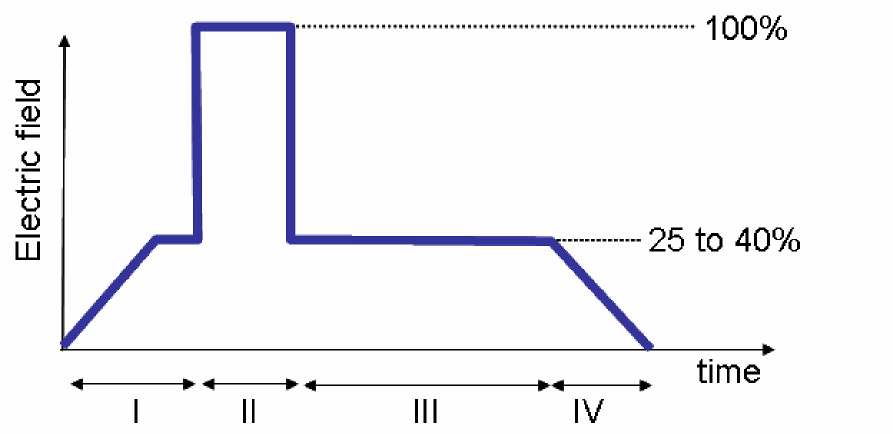

Figure 5-4-4. The pulse shape used for the poling of MgO:SLT and SLT. Stage I: Slow increase of the field to avoid shock; Stage II: Main poling process; Stage III: Stabilization and avoidance of backswitching; Stage IV: Slow decrease to avoid backswitching and also to monitor the electro-optic effect.

In all of the cases, periodic-poling was achieved performed by using the charge measurement and the direct SHG monitoring feedback. In the lower electric field regime (0.8 to 1.2 kV of the amplifier voltage for 1 mm thick samples), we needed to apply longer pulses or even multiple pulses (more than 50 times) to achieve domain reversal. Typically, more than half of the poled area backswitched in this regime in the first 5 to 20 pulses as deduced from the backswitching current. That might be because of the relatively larger surface capacitance, C_s, as mentioned in Section 4.2.2. In addition, since the amplitude of current from domain switching (less than 2 μA) is low and close to the noise level (approximately 0.4 μA), the integrated charge monitoring was not effectively worked with enough accuracy. It might be possible to improve the accuracy by reducing backswitching employing longer pulse duration and a low number of pulses. And it might also possible to use a much lower resistance R_4 for monitoring the current.

In the higher electric field regime (more than 1.3 kV/mm of the amplifier setting), the switching current was more than 5 μA and was readily measurable. In addition, the amount of backswitching was much smaller than in the low electric field regime. Thus, the accuracy of the charge integration worked effectively. A typical current profile when poling by using a 1.5 kV/mm of amplified voltage setting with 100 ms duration pulses is shown in Fig. 5-4-5. The poled area was approximately 3 mm×8 mm. In both SLT and MgO:SLT cases, the current flow is self-terminated and that specific point is almost the same as the optimum stopping point. The charge measurement results were in good agreement with the direct SHG monitoring results. In case of the SLT, an almost perfect QPM structure was obtained with 8 to 12 pulses while only 4 to 6 pulses were required for the MgO:SLT. Although MgO:SLT has a slightly higher coercive field than that of the SLT as mentioned in Section 4.2.2, the required number of pulses were smaller than for SLT. This fact might be related to the lower surface capacitance C_s of MgO:SLT, which might make nucleation and stabilization of new domains easier.

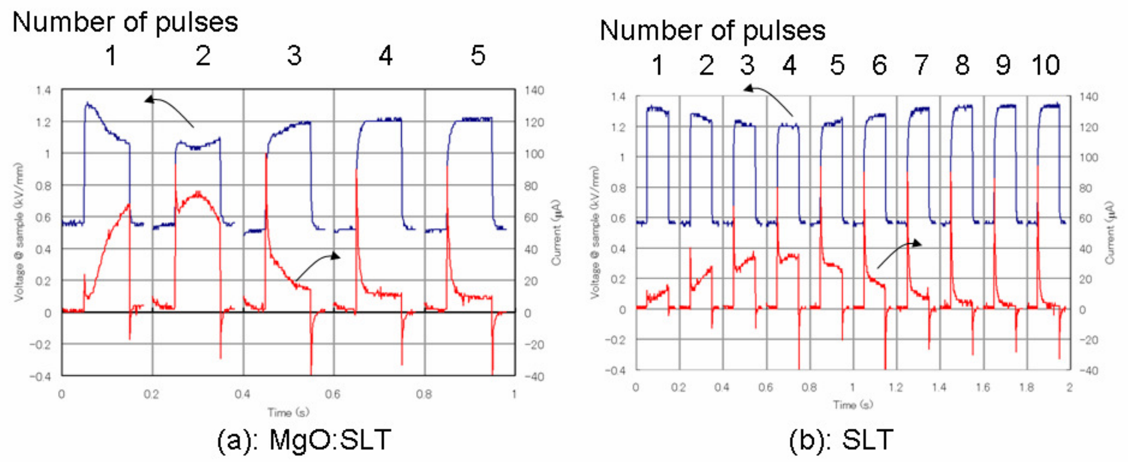

(a): MgO:SLT

(b): SLT

Figure 5-4-5. Current flow and voltage at the samples in Stage II.

Pictures of etched PPMgOSLT and PPSLT samples are shown in Fig. 5-4-6. A period of 30 μm was fabricated with 40:60 to 50:50 duty cycles over the whole poled area of approximately 3 mm×8 mm with thickness of 1 mm. This corresponds to a domain broadening by approximately 3 μm compared to on the patterned side. . The duty cycle of patterned surfaces was slightly wider in poled area than the opposite face. Typically, the unpatterned surface tended to become a curtain like domain wall structure, especially in PPMgO:SLT.

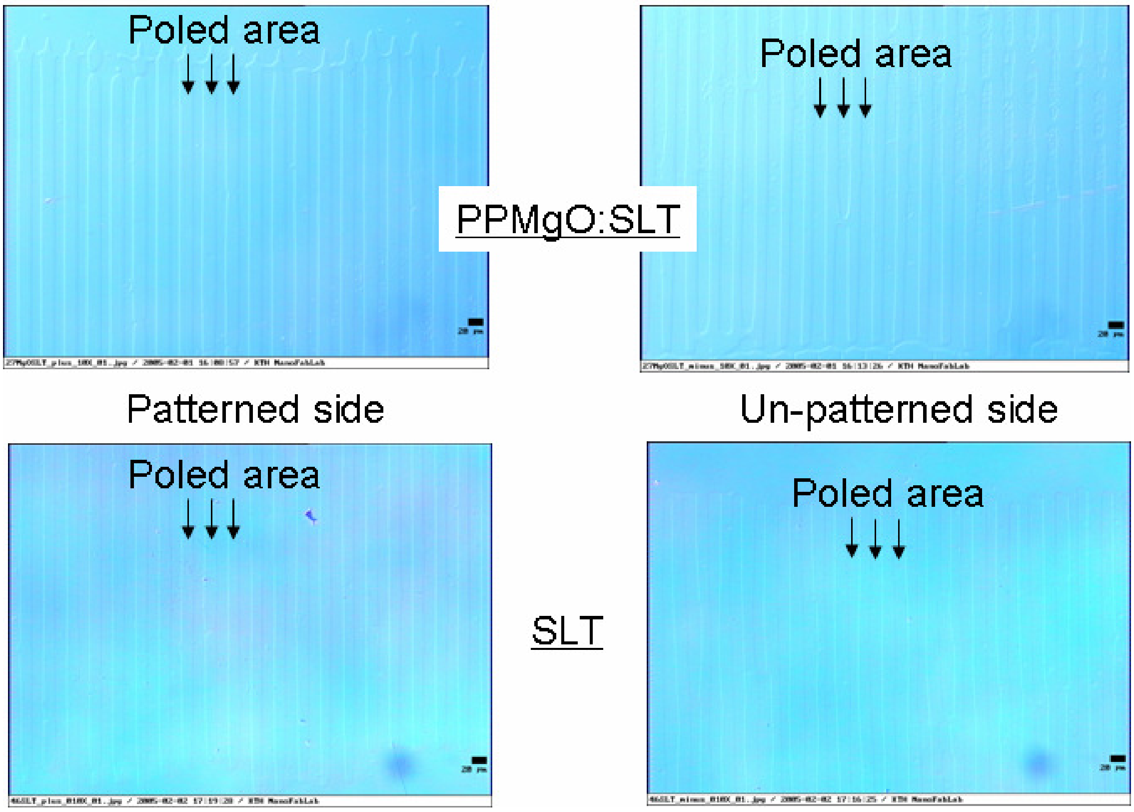

Figure 5-4-6. PPMgO:SLT and PPSLT with 30 µm period.

Several trials for poling of a 7.5 µm QPM period were also performed using a similar procedure. In this case, much more precise control was required to avoid domain merging. A duty cycle of the electrode:photoresist of 15:85 or much less was required. Since the domain broadening was larger in the higher applied voltage regime, it is necessary to use the low voltage regime, although in this case it is difficult to follow the domain growth by monitoring of the poling current flow. Direct monitoring of the SHG is then the most useful feedback for the QPM quality. An amplifier voltage of 0.7 kV to 1.0 kV with pulse duration time of 1 s was applied approximately 400 times. The periodically-poled pattern on the patterned surfaces were obtained over the area of 3 mm×5 mm as shown in Fig. 5-4-7. Optimization of the process is still in progress with the aim to improve the uniformity and the reproducibility.

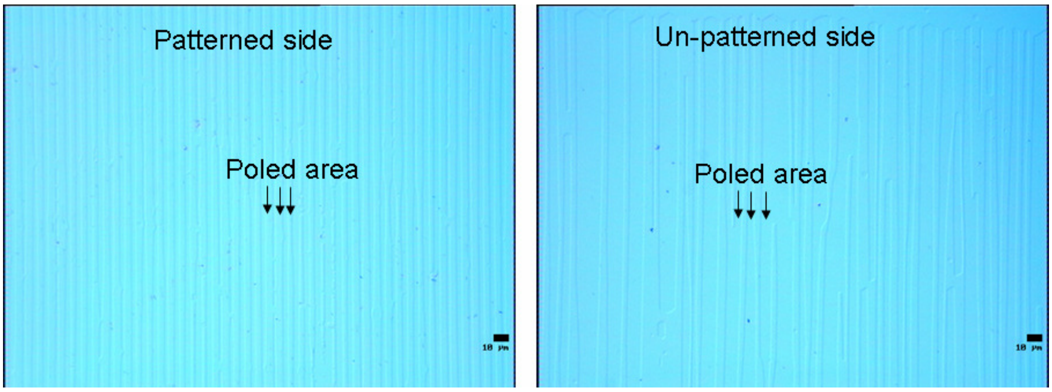

Figure 5-4-7. SLT fabricated with 7.5 µm periodicity.

5.4.2. $KTiOPO_4$ and its isomorphs

KTP isomorphs are characterized by a large anisotropy in domain wall propagation velocities in different directions, which makes the domain broadening less severe compared to SLN or SLT. On the other hand, the relatively high ionic conductivity in KTP at room temperature compensates the poling and prevents implementation of an effective feedback to control the poling process. Therefore methods with selective ion diffusion and low temperature poling have been derived to tackle this problem.[17, 18)] Over the years the quality of commercial KTP wafers has increased substantially allowing implementation of a rather simple room temperature poling techniques at KTH. Here we present a brief outline of these procedures, which have also been reported in a number of publications.[1, 19)]

Nucleation control

First, it is important to check the conductivity distribution of the wafer. A map of the conductivity is attained for each wafer. Since the coercive field depends on the conductivity as described in Section 4.2.3, the wafers are then cut into smaller pieces with as uniform conductivity as possible. KTP usually does not contain micro domains in, probably due to its higher conductivity which compensates the pyroelectric effect and that prevent micro domain generation. The nucleation density in KTP is larger on the C^- surface than the C^+ surface and Al electrode enhance the number of nucleation than direct contact with liquid electrode.[1)] Thus, the periodic electrode pattern is formed on the C^- surface and created by Al thin film.

Optimizing the periodic domain growth

For 20 to 30 μm periods, the duty ratio of the electrode:photoresist is preferred to be 40:60, For periods shorter than 10 μm, which are commonly used for the generation of visible light, the ratio is preferred to be 25:75 or even a smaller aspect ratio. For the case of sub-micron periods, a selective chemical treatment such as K^+ ion diffusion is needed in order to fabricate the proper PP structures. For KTP, homogeneous PP structures can be fabricated by using the type A sample holder, as the contact resistance in much less critical for KTP than SLN or SLT, probably due to lower surface capacitances C_s.

The high conductivity of KTP does not allow use of a high serial resistance. The shape of the electric poling pulses has been a square shape with a rise time shorter than 100 μs and a fall time around 1 ms. The pulse duration was typically 1 to 10 ms. There are several reasons to use short pulses instead of a continuous poling field. First, the poling in KTP is too fast (less than 1 s) to allow a manual stop of the pulse and, furthermore, since the poling current is masked by the ionic current, no effective feedback loop can easily be implemented. The third reason is that domain wall pinning is prevented by switching the voltage on and off. The last reason is that the high conductivity of KTP could cause material breakdown by using pulses much longer than several tens of ms. Thus, there are two control parameters in the KTP case; the strength of the applied electric field and the number of the applied pulses. Since KTP normally does not show backswitching phenomena, we do not need a domain stabilization stage in the pulse shape as shown in MgO:SLT and SLT. That might also related to lower surface capacitance C_s.

The starting point of domain switching is mainly monitored by the E-O effect method. The final tunings are done by the direct SHG measurements. In KTP, domain propagation along the polar axis and sideways spreading of the domain wall seem to be two competing processes due to the limited supply of external electrostatic energy. If the domain propagation along the polar axis is slowed down for instance due to presence of crystal defects, then we should expect larger domain broadening. Also sidewise domain growth and merging occurs before the tips reach the opposite polar face. Correct domain growth seems to depend on the electric field strength and the number of pulses.

At KTH, three different poling regimes have been investigated:1) low field, high field, and a combination of high and low field regimes. For poling in the low field regime we mean poling with fields below or very close to the coercive field; and poling with fields higher than the coercive field for poling in the high field regime. The idea behind poling in the low field regime is to obtain slow domain speeds, so that the domain merging can be controlled. Although this seems to work in some case, it usually yields overpoling under the pattern and a shallow domain depth. Poling in the high field regime will be beneficial in the sense that the domains will propagate much faster to the opposite face. The best results have been obtained by poling the samples with one or two single pulses in the high field regime, in contrast with MgO:SLN, SLT, and MgO:SLT where a moderate or low field is desired in order to prevent domain broadening. The pulse should give enough energy to pole the sample all the way through but prevent excessive domain broadening and merging. However, if the magnitude of the applied field is too high, the domains maintain a periodic structure close to the patterned face and the broadening and merging occurs in the bulk. Thus, the magnitude of the pulse needs to be adjusted for each particular sample, and its value can be guessed from the conductivity and the E_c measurements. A typical picture of a homogeneously fabricated PPKTP is shown in Fig. 5-4-8.

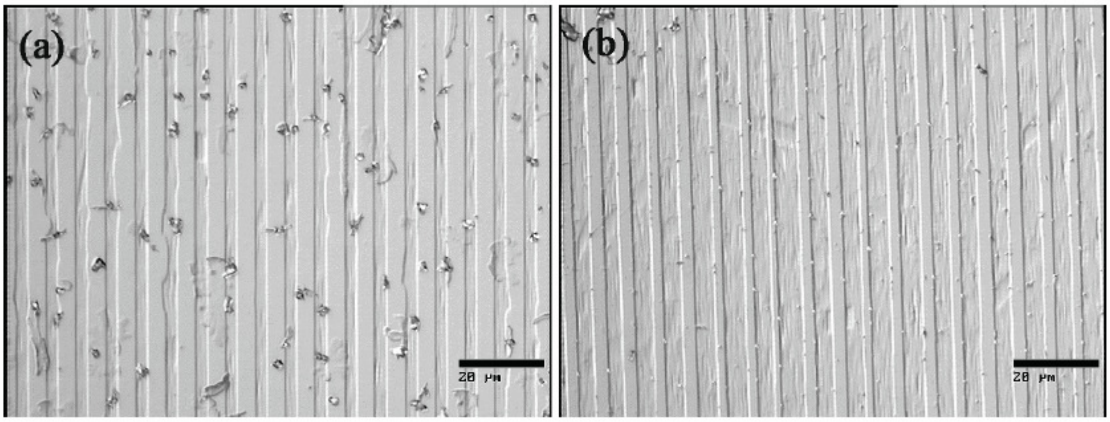

Figure 5-4-8. PPKTP where the poling condition was one pulse with an amplitude of 2.65 kV/mm and 6 ms duration. The period is 10.6 μm.1)

The idea behind poling with a combination of the high and low field regimes is to give enough energy in the first pulse to propagate the domains deep enough and then, with pulses of lower magnitude, slowly merge them. Usually, with the first high field pulse, the domains penetrate to a depth of 300 - 400μm. With the subsequent low field pulses it is possible to propagate them 200-300μm more before any severe domain merging occurs.

5.4.3. $KNbO_3$ Paper II, V)

For the KN crystals, two different types of PP structures are described: one of them consists of the normal 180°-domains (PPKN) and the other one made from the 90°-domains (PP90KN). This part of the research has been done both at Mitsui Chemicals, Inc. and the Royal Institute of Technology (KTH) in Stockholm.

PPKN

Previous reports

Two other groups have reported on conditions for poling of PPKN. The poling parameters are summarized in Table 5-4-3.[20-21)] In both reports, undesirable non-180°-domains have been observed during the periodic poling process. From my experience of crystal growth and post growth processes, generations of non-180°-domains are strongly related to crystal quality, which requires a very precise and careful control. Meyn et al. fabricated PPKN by applying two sets of electric field pulse of 500 V/mm with 5 ms duration. They observed that approximately 50% of the charge flowed back through the crystal after switching off the applied electric field.[20)] This backswitching might be related to the generation of 90°-domains. Kim et al. observed many 60°-domain on the surface.[21)] That might be much related to both crystal quality and a high applied electric field of 500 V/mm.

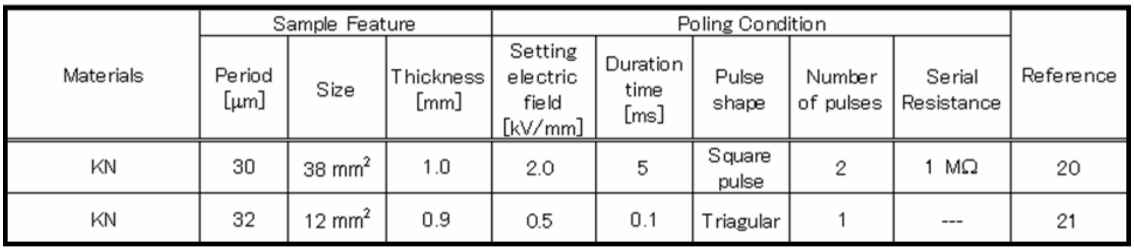

Materials	Sample Feature			Poling Condition					Reference
	Period [μm]	Size	Thickness [mm]	Setting electric field [kV/mm]	Duration time [ms]	Pulse shape	Number of pulses	Serial Resistance	
KN	30	38 mm^2	1.0	2.0	5	Square pulse	2	1 MΩ	20
KN	32	12 mm^2	0.9	0.5	0.1	Triagular	1	---	21

Table 5-4-3. Reported poling conditions for KN. '---': not mentioned in the paper.

Nucleation control

Typically commercial wafers do not have any micro-domains and non-180°-domains. However, considering the low coercive field and the low conductivity, it is important to keep a slow temperature change in the soft-baking process in order to prevent formation of unwanted 60°- or 90°-domains. For KN, the inhomogeneity of the poled area related to the contact edge fringing field effect, as was seen in MgO:SLN, was much smaller than in MgO:SLN, SLT, and MgO:SLT and similar to that in KTP. This should be related to its substantial anisotropy in the domain morphology similar to the case for KTP. An electrolyte electrode of type A was used for periodic poling, signifying a relatively small surface capacitance in this method. There are no significant difference observed between periodic electrode pattern created on the –c and on the +c surface.

Optimizing the periodic domain growth

A duty cycle of 30:70 (electrode:photoresist) was used for the 14 to 45 μm period samples. For the sub-10 μm periods, the optimum ratio should be smaller. In the initial experiment, a low serial resistance was used. By following Ref. 20, a 500 V/mm pulse was applied to the prepared sample but, typically, three problems occurred: generation of unwanted non-180°-domains, partial poled, and non-reproducible process.[Paper II)] The first problem was solved by reducing the electric field amplitude and even modifying the pulse shape of the applied electric field. For the second and third issues, we introduced the pre-switching process (the embryonic nucleation process), in which the spontaneous polarization was switched back and forth approximately 2 to 10 times before the real pulse-poling was performed. This technique was based on the observation of a reduction of the coercive field after repeating the P_s switching, as mentioned in the Section 4.2.5. By switching the polarization back and forth several times, it is easier to generate nuclei for new domains and, thus, the homogeneity is increased. This reduction of the coercive field might indicate a reduction of the surface capacitance C_s. which might be originally different from point to point. The embryonic nucleation process is performed by using a triangular pulse to avoid a quick change of the electric field which, otherwise, could cause unwanted non-180°-domains. Afterwards, the pulse-poling process was performed by using the pulse shape as shown in Fig. 5-4-9. By using this technique, the current profiles of the pulse-poling process became reproducible as shown in Fig. 5-4-10. As it seems nearly optimum poling condition is given by a field strength of 300 V/mm and with pulses of 50 ms duration. In this way, homogeneous PPKN was obtained with a size of 11 mm×11 mm, as shown in Fig. 5-4-11, and the patterned periods are clearly recognized on both the patterned and the un-patterned surfaces. By using a high serial resistance, it is thus possible to fabricate homogeneous PPKN with a 30 μm periodicity. However, also in this case, it is better to the combine the current monitoring method with the direct SH-monitoring technique.

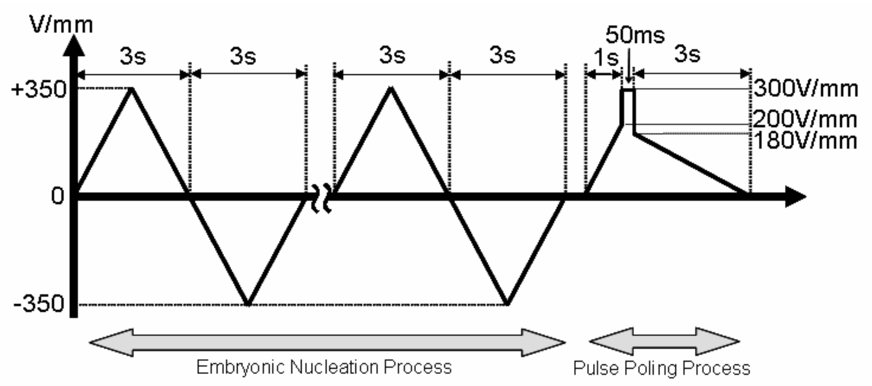

Figure 5-4-9. Pulse shapes for PPKN poling.

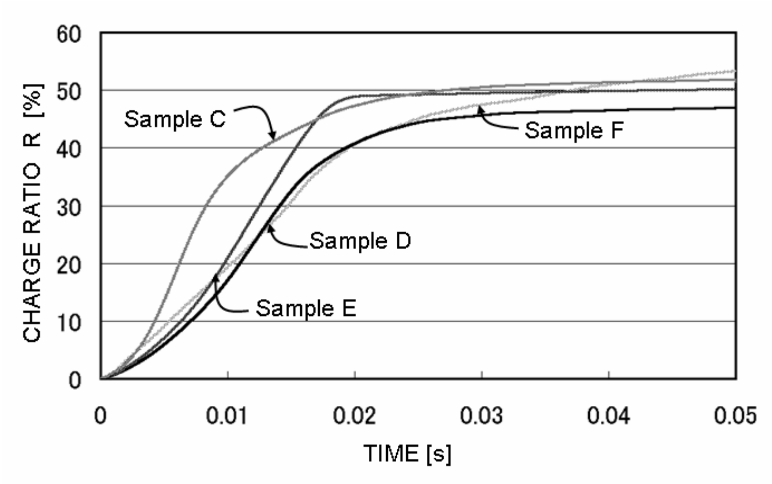

Figure 5-4-10. Reproducibility of the charge flow during PPKN poling. Charge ratio R = 50% corresponds to the optimum charge to create a 50:50 duty cycle of PPKN.

In some cases, unwanted 90º-domains were still generated during the poling process. That might be because they have lower coercive field than that of the 180º-domain as was mentioned in Section 4.2.4. However, since these 90º-domains are very thin and unstable, they can be removed by annealing at 215ºC for 4 hours as is shown for samples in Fig. 5-4-12.

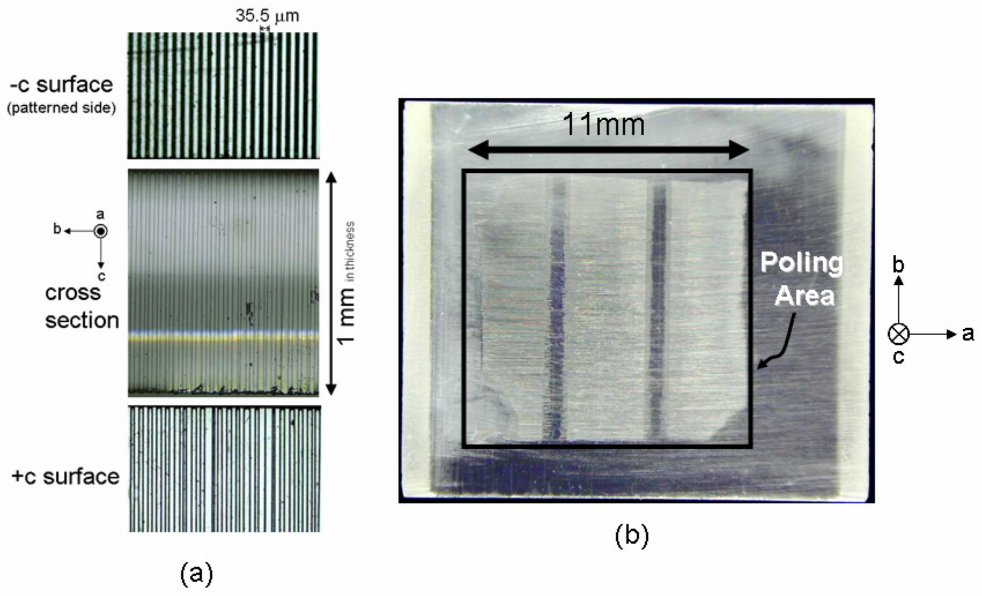

Figure 5-4-11. Fabricated PPKN. (a): Patterned, un-patterned and cross-section view. (Cross section is revealed by cutting the sample in the a-c plane at an angle of 70° with respect to the +c direction.) (b): Homogeneity of the PPKN structure.

Figure 5-4-12. Removing unwanted domains in PPKN by annealing as a post-poling process.

PP90KN

Nucleation control

The schematics for fabrication of PPKN with 90º-domains (PP90KN) is shown in Fig. 5-4-13. Several $(\bar{1}01)$-cut $KNbO_3$ plates, approximately 10 mm × 5 mm × 0.7 mm (as measured along the [101], [010] and $[\bar{1}01]$ directions, respectively) were prepared in order to fabricate the periodic 90º-domain structures perpendicular to the sample surface. The photoresist layer was coated on the $(\bar{1}01)$ surface. The duty cycle for the electrode:photoresist was 30:70 for the samples with a periodicity of 18.6 µm. The constant grating lines were made parallel to the [010] direction to obtain an allowed domain wall direction. Then, gold contacts were deposited by evaporation on the entire $(\bar{1}01)$ and $(10\bar{1})$ surfaces in order to prevent preferential nucleation of the 60°-domains by the electric field inhomogeneities at the electrode edges.

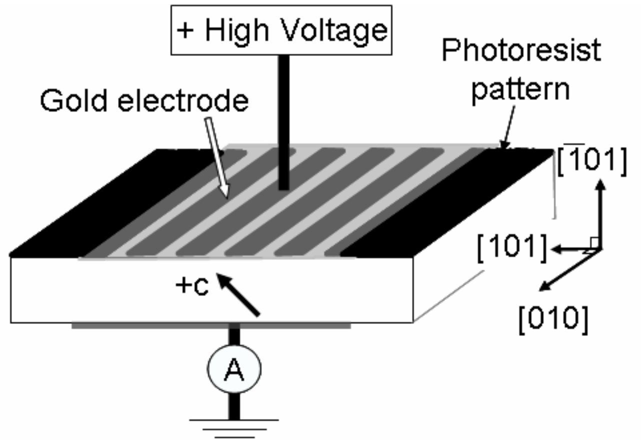

Figure 5-4-13. Schematic configuration of the PP90KN fabrication setup.

Optimizing the periodic domain growth

During poling, a low serial resistance was used. Since the electric current flow was very weak (5 to 60 μA) comparing to the noise level (12 μA in this case), we put a low-pass filter (cutoff frequency at 5 Hz) between the resistor and the oscilloscope to improve the signal/noise ratio. To optimize the parameters for the fabricating of uniform PP90KN, different forms of voltage patterns (DC, pulse) were applied while changing the amplitude and the duration at room temperature. Using the pulsed voltage technique substantial amounts of unwanted domains were generated in most cases. We then instead optimized the poling parameters using only DC voltage. Figure 5-4-14 shows an example of the observed current signal during the fabrication process when applying an electric field of 200 V/mm for 600 s at room temperature. The poling current increased quickly within 10 seconds after applying the DC electric field and decreased again exponentially with a time constant of approximately 200 seconds.

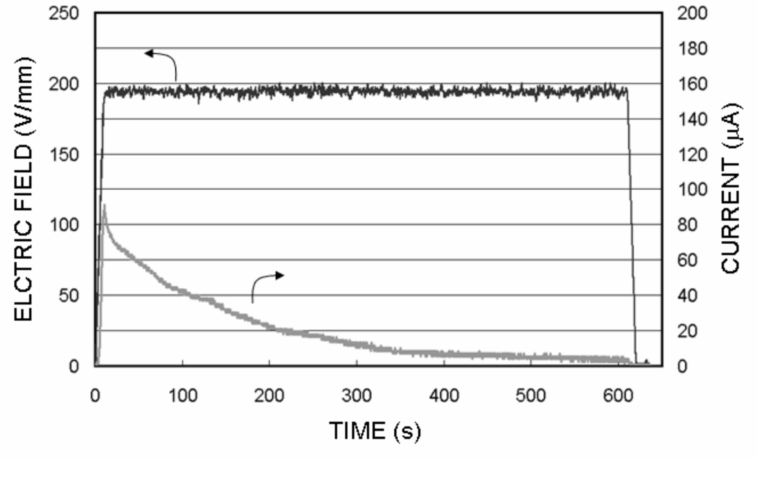

Figure 5-4-14. The profiles of the applied electric field and the current for the PP90KN fabrication.

Figure 5-4-15 shows a schematic drawing of the PP90KN sample together with a transmission optical microscope image of the fabricated PP90KN structure with 18.6 μm period as observed along the [$\bar{1}$01] direction. Since the crystallographic axes, X (a) and Z (c), are rotated by 90° between the original- and the 90°-domains, the domain walls are recognized as bright and dark lines due to the opposite directions of the Poynting-vector walk-off in the adjacent domains, The domain walls are parallel to the input surface of the sample; i. e., to the (101) plane. The homogeneity of the 18.6 μm periodicity was, however, not perfect over the whole sample due to some domain merging which we associate with the homogeneity of the original single-crystal wafer.

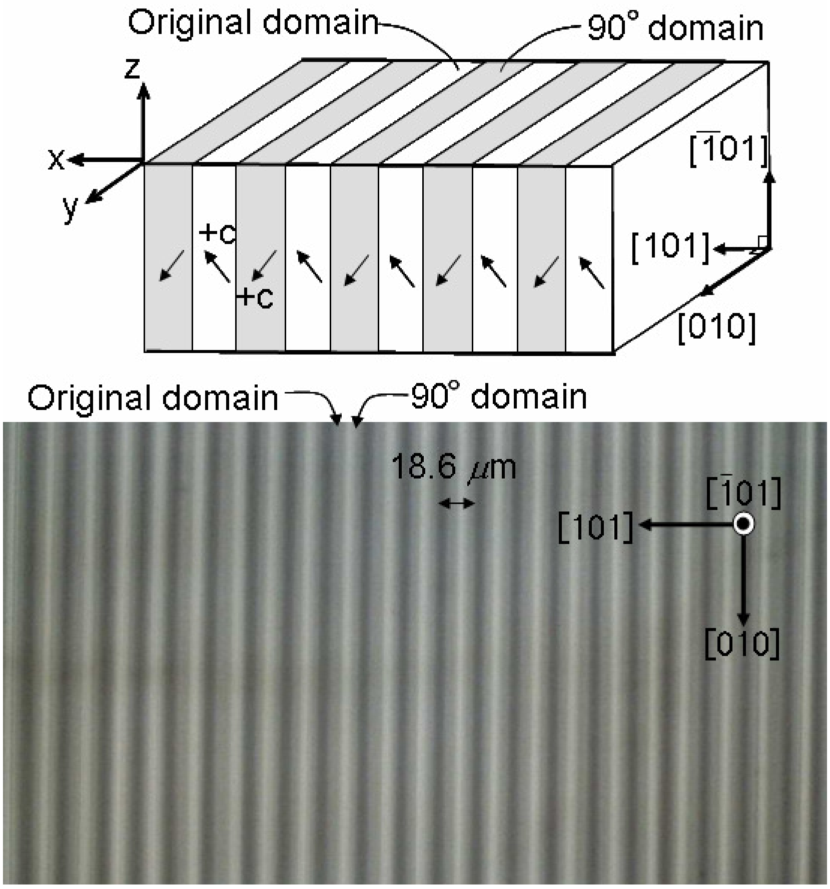

Figure 5-4-15. Schematics of the PP90KN structure and a picture of the fabricated PP90KN as observed by a transmission microscope.

5.5 Optical performances of the fabricated periodically-poled devices Paper V, VI)

Ultimately, the quality of the QPM structure and its usefulness is revealed in optical frequency conversion experiments. The QPM structures with approximately 30 μm periods fabricated in different materials were subsequently tested in OPO setup pumped at 1064 nm. In addition, the PP90KN with 18.6 μm period was tested in SHG experiment to reveal wave properties of these structures.

5.5.1. Comparison of OPOs by pulsed 1064 nm laser

OPOs were constructed with PP samples in all our materials with experimental configuration as shown in Fig. 5-5-1. The radiation from a 1064 nm Nd:YAG with 5 ns pulses and a repetition rate of 20 Hz was focused into the cavity which was resonant for the signal wavelength at 1500 nm. The input mirror was coated with high transmission for 1064 nm and high reflection (99%) for 1500 to

1650 nm while the output mirror was coated with high reflection (90%) for 1500 to 1650 nm. The OPO pump threshold, which is related to the effective nonlinear coefficient as described in Eq. (3-5), were measured at room temperature for each PP sample. The same pump focusing conditions were kept in all cases.

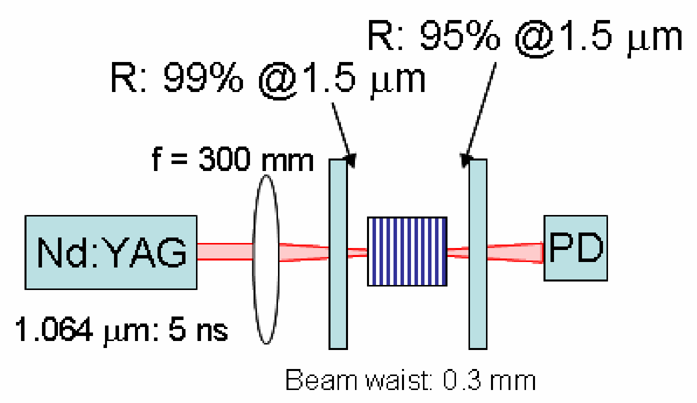

Figure 5-5-1. Experimental configuration for the OPO setup.

The measured results are summarized in Table 5-5-1. The OPO threshold power of the PPKTP was the lowest among the fabricated materials. Since the OPO threshold is proportional to the figure of merit, the effective nonlinear optical coefficient, d_{eff}, and nonlinear optical coefficient, d_{33}, are estimated as based on the measured PPKTP value and Eq. (2.18). The estimated d_{eff} and d_{33} of PPMgO:SLN has the highest value, however, the value is more than 20% smaller than the reported values as shown in Table 3-4-2. Both PPMgO:SLT and PPSLT are almost comparable to PPKTP and estimated d_{33} values for the stoichiometric materials are similar or slightly lower than the previous reported values. There might be several reasons for this. One reason could be that the reported values are overestimated. The second reason might be that the duty cycle of the fabricated PP structures are not perfectly 50:50. The third reason can be non-straight domain walls. The non-straight domain walls also generate diffraction colorful patterns when the OPO is operated, as shown in Fig. 5-5-2. The diffraction is obtained with green light which is non-phase-matched SHG of 1064 nm radiation and the red light which is the sum-frequency generation of the 1064 nm pump beam and the 1500 nm signal light. The diffraction line which is perpendicular to polar direction has quasi-continuous intensity distribution which can be approximated by normal distribution. This points to a random distribution of domain lengths across the pump beam radius. Thus, the amplitude of diffraction corresponds to the mean irregularity of the domain wall, <y>. This value can be extracted from an

Material	Interaction length [mm]	OPO threshold P_{th} [mW]	Refractive index n_p n_s n_i	Estimated d_{eff} [pm/V]	Estimated d_{33} [pm/V]
PPKTP	8	5.0	5.88	10.6	16.7
PPMgO:SLN	8	5.4	9.56	13.0	20.4
PPMgO:SLT	8	8.0	9.28	10.6	16.7
PPSLT	8	7.5	9.28	10.9	17.1
PPKN	6	18.0	9.14	---	---

Table 5-5-1. Measured OPO threshold power and estimated nonlinear coefficient, d_{eff}, of fabricated devices. The estimation values are based on Eq. (3-5) to (3-7), and the measured PPKTP value. PPKN could not be compared with the others because of different interaction length.

inverse Fourier transform of the diffraction pattern. These diffraction effects were not removable even after annealing the samples. Since no linear diffraction effects were observed when the 532 nm or 632 nm lasers were incident directly into the samples, these phenomena are clearly associated with the nonlinear effects. The nonlinear diffraction phenomena were not observed in PPKN or in PPKTP. This might be because the rectangular domain morphologies of these crystals produce much more straights domain walls compared with PPMgO:SLN, PPMgO:SLT, and PPSLT. On the other hand, considering large sensitivity of E_c on stoichiometry of MgO:SLT, SLT, and MgO:SLT, the sub-μm variation in stoichiometry might result in sub-μm to wavelength, λ, irregularity in the domain walls.

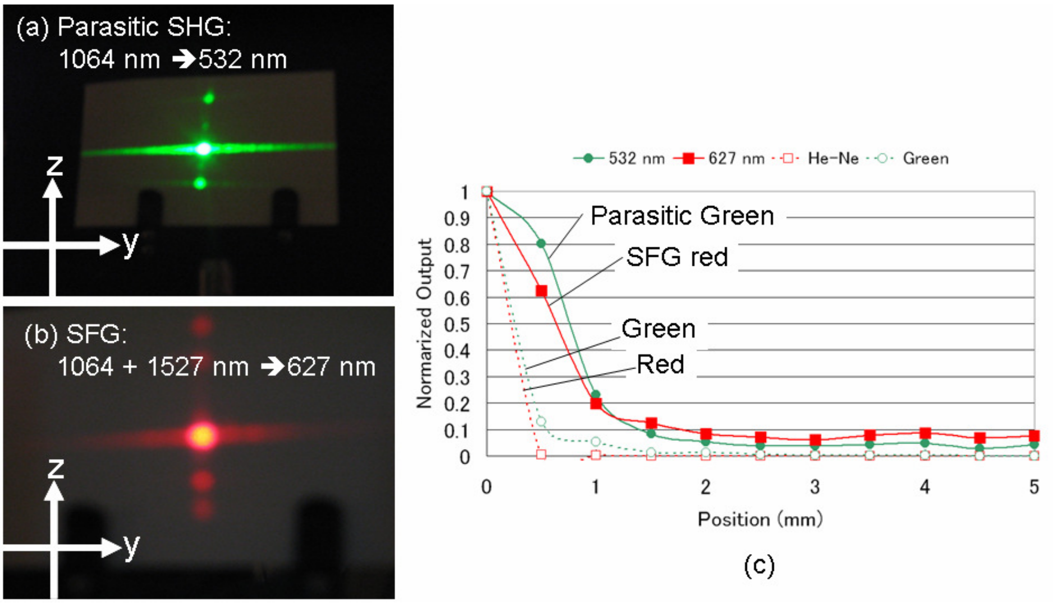

Figure 5-5-2. Nonlinear diffraction in the OPO experiment. (a): Parasitic green light, (b): Red light from SFG by 1064 nm and 1500 nm. (c): Intensity plot of the diffracted light compared to the transmission of green or red light.

Typically, PPMgO:SLT and PPKN can sustain similar fundamental pump power levels as that of PPKTP in this configuration. However, PPMgO:SLN showed photorefraction when the peak intensity of the fundamental beam exceeded 700 MW/cm^2 at a temperature lower than 80°C. In addition, the photorefraction in PPMgO:SLN caused material breakdown by the parasitic green light in the cavity as shown in Fig. 5-5-3(a), so the material has to be further improved for real-worked

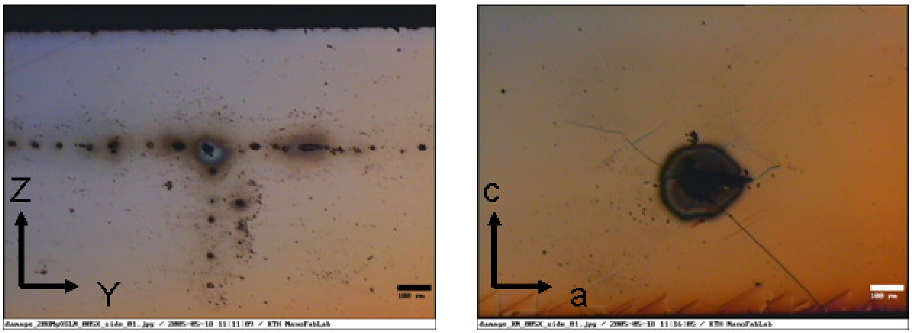

(a) PPMgO:SLN (b) PPKN

Figure 5-5-3. Material breakdown tracks in the OPO experiments. (a): PPMgO:SLN, (b): PPKN.

applications. In the case of PPKN, the material breakdown was observed at a much higher peak intensity (~ 1 GW/cm^2) using 1 ns pulses as shown in Fig. 5-5-3(b). Under the same conditions, the PPKTP was not damaged.22) In the case of PPKN, the breakdown mechanism is different from that in PPMgO:SLN. The high-peak intensity pump beam would cause thermal shock in the crystal, which induced the generation of 90°-domains. This high-peak power pump beam were paetly reflected at the 90°-domain walls, which might have caused high intensity spots in the crystal which, consequently, could have induced the crystallographic material damage.

5.5.2. Second harmonic generation by PP90KN Paper V, VI)

The typical scheme we used for SHG with PP90KN is shown in Fig. 5-4-15. When the optical beams propagated along the original [101] axis, we consider here two cases of QPM frequency doubling, with the fundamental beam polarized parallel to the $[\bar{1}01]$ and the [010] directions, respectively. We define three new coordinates, the *x*, *y*, and *z* axes, respectively, corresponding to the [101], [010], and $[\bar{1}01]$ direction of the original domain. Since $KNbO_3$ has 5 different nonlinear coefficients (d_{31}, d_{32}, d_{33}, d_{15}, and d_{24}), the nonlinear coefficients, d'_{zzz} and d'_{zyy}, as defined in the new coordinate system and for the two polarizations of the fundamental beam, can be written as follows,

$$d'_{zzz} = \frac{1}{\sqrt{2}} \cdot (d_{15} + \frac{d_{31} + d_{33}}{2}) \quad , \qquad (5\text{-}2)$$

$$d'_{zyy} = \frac{1}{\sqrt{2}} \cdot d_{32} \quad . \qquad (5\text{-}3)$$

Substituting the values for d_{31}, d_{32}, d_{33}, and d_{15} in the case of SHG at 960 nm into the above equations, gives d'_{zzz} = 21.1 pm/V and d'_{zyy} = 10.1 pm/V, respectively. The QPM periods corresponding to these nonlinear coefficients were then calculated for a temperature of 22°C by using the Sellmeier equations from Ref. 23. The periods for SHG at 960 nm are approximately 4 μm for the d'_{zzz} case and 18.6 μm for the d'_{zyy} case, respectively.

After polishing both of the (101) surfaces (the *x* surfaces) of the fabricated PP90KN with 18.6 µm periodicity, the second-harmonic generation experiment was tested by using the d'_{zyy} coefficient. The nominal interaction length was estimated to be 9 mm. Due to the critical phase matching, the Poynting vector walk-off (approximately 3°) for the second-harmonic-wave is introduced in this configuration in bulk crystals.23) In the PP90KN case, the direction of the Poynting vector changes at the 90° domain boundaries. Figures 5-5-4 show the relationship between the wave vectors, $\boldsymbol{k_1}$, $\boldsymbol{k_2}$ and the Poynting vectors $\boldsymbol{P_1}$, $\boldsymbol{P_2}$ in both the original and the 90° domain cases for a p-polarized wave (with electric vector perpendicular to the *y*-axis).24, Paper VI) The directions of $\boldsymbol{P_1}$ and $\boldsymbol{P_2}$ are determined as the tangential direction at the points A and B, respectively (see Fig. 5-5-4). When the $\boldsymbol{k_1}$ is nearly perpendicular to the domain boundary, the $\boldsymbol{P_1}$ is refracted toward the $\boldsymbol{P_2}$ negatively [Fig. 5-5-4(a)]. On the other hand, when the $\boldsymbol{k_1}$ is nearly parallel to the domain boundary, the $\boldsymbol{P_1}$ is refracted to the $\boldsymbol{P_2}$ positively [Fig. 5-5-4(b)]. Since the $\boldsymbol{k_1}$ is perpendicular to the domain boundary in our experimental configuration, the $\boldsymbol{P_1}$ refracts negatively at all of the domain boundaries. In addition, since the input and output angles of the Poynting vectors (θ_1 and θ_2 in Fig. 5-5-4) are equal, the periodic structure periodically compensates for the walk-off. Eventually, a maximum output power of 77 μW was generated at 480 nm from a single-pass frequency doubling of 550 mW power from a Ti: sapphire laser at 22.0°C. The measured QPM wavelength is coincident with the calculated one for a period of 18.6 μm. Due to the walk-off compensation, the output second harmonic beam was circular and collinear with the fundamental beam. In contrast to the alternating direction of the Poynting vector walk-off, as discussed above, there is no refractive index change at the 90° domain walls, when the beam propagates in the *b* plane [(010) plane].24, Paper VI) Consequently, there should be no reflections at the domain boundaries. This phenomenon was also observed in this study, i.e., no reflection was observed at the domain boundaries for both the fundamental and the second harmonic waves.

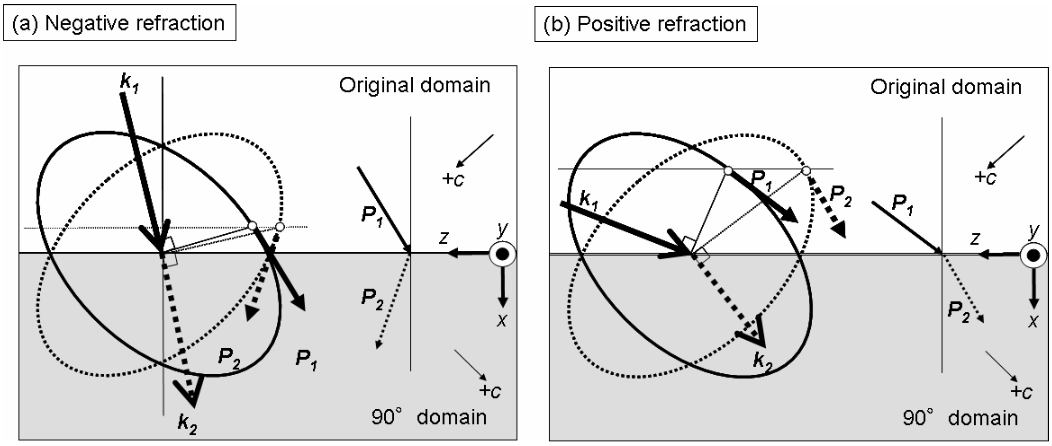

Figure 5-5-4. (a): Negative and (b): positive refraction at the 90°-domain boundaries.

From the measured efficiency of SHG we calculated the effective nonlinear coefficient using:

$$d_{eff} = \left[\frac{P_{out}}{(P_{in})^2} \cdot \frac{\lambda_\omega^3 \cdot n_\omega \cdot n_{2\omega} \cdot \varepsilon_0 \cdot c}{16\pi^2 \cdot l} \cdot \frac{1}{h} \right] \quad , \tag{5-4}$$

where P_{in} is the fundamental power inside the crystal, P_{out} is the corresponding second-harmonic power, λ_ω is the fundamental wavelength, n is the refractive index evaluated at the frequency given in the subscript, l is the interaction length, and h is the Boyd-Kleinman factor.[25] The ratio of the effective interaction length, and the confocal parameter, $\xi = l / b$ was 0.68 in this experiment, which gives the value h = 0.7. The PP90KN sample that was used in this experiment had an effective nonlinear coefficient of $d_{eff,\ meas}$ = 1.8 pm/V. This is approximately 28% of the theoretical value, $d_{eff.calc} = (2/\pi)\ d'_{zyy}$ = 6.4 pm/V. The main reason for the difference between the measured and the theoretical values of d_{eff} could be that the duty ratios of the 90°-domain structures were not 50:50 over the whole sample length. Figure 5-5-5 shows the measured wavelength and temperature tolerance curves. Both curves bear a similarity to a sinc^2 function, the apparent distortions indicating, however, that the structure is not perfectly periodic.

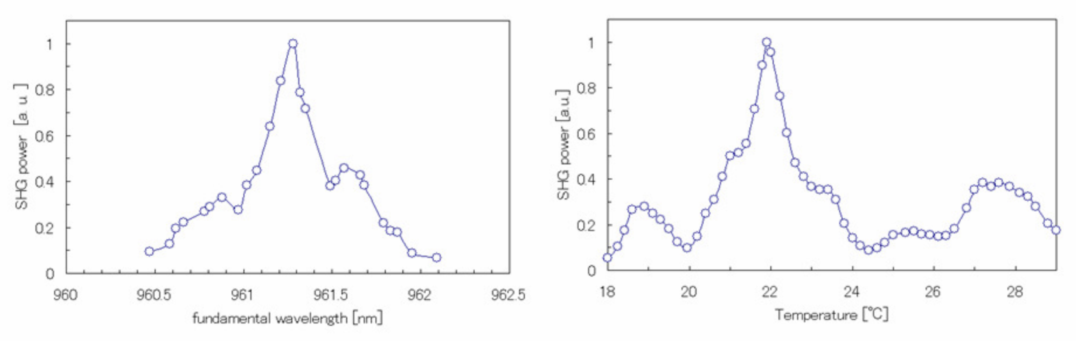

Figure 5-5-5. SHG temperature and wavelength tolerances of fabricated PP90KN.

References in Chapter 5

1) C. Canalias: “Domain engineering in $KTiOPO_4$,” Ph. D Thesis. ISBN 91-7178-152-8, Royal Institute of Technology, (2005).

2) G. D. Miller: “Periodically poled lithium niobate: modeling, fabrication, and nonlinear-optical performance,” Ph. D Thesis. Stanford University (1998), Chapter 2 .

3) H. Karlsson, F. Laurell, and L. K. Cheng: Appl. Phys. Lett. **74**, 1519 (1999).

4) K. Nakamura, J. Kurz, K. Parameswaran, and M. M. Fejer: Appl. Phys. Lett. **91**, 4528 (2002).

5) M. Maruyam, H. Nakajima, S. Kurimura, N. E. Yu, and K. Kitamura: Appl. Phys. Lett. **89**, 011101 (2006).

6) L. Huang, D. Hui, D.J. Bamford, S.J. Field, I. Mnushkina, L. E. Myers, and J. V. Kayser: Appl. Phys. B, **72**, 301 (2001).

7) H. Takasaka, T. Sato, Y. Sasaki, K. Suizu, H. Ito, H. Matsumoto, and S. Suwabe: The 8th international symposium on ferroic domains and micro- to nanoscopic structures (ISFD-8), Tsukuba, Japan, (2004), P02-30.

8) A. Grisard, E. Lallier, K. Polgar, and A. Peter: Electron. Lett. **36**, 1043 (2000).

9) T. Hatanaka, K. Nakamura, T. Taniuchi, H. Ito, Y. Furukawa, and K. Kitamura: Opt. Lett. **25**, 651 (2000).

10) M. Nakamura, S. Takekawa, K. Terabe, K. Kitamura, T. Usami, K. Nakamura, H. Ito, and Y. Furukawa: Ferroelectrics **273,** 199 (2002).

11) N.E. Yu, S. Kurimura, Y. Nomura, M. Nakamura, K. Kitamura, J. Sakuma, Y. Otani, and A. Shiratori: Appl.

Phys. Lett., **84**, 1662 (2004).

12) N.E. Yu, S. Kurimura, Y. Nomura, M. Nakamura, K. Kitamura, Y. Takeda, J. Sakuma, and T. Sumiyoshi: Appl. Phys. Lett. **85**, 5134 (2004).

13) T. Usami, K. Nakamura, H. Ito, and K. Kitamura: 2001 Annual report of Prof. Ito’s lab., Tohoku University.

14) S. Kurimura, N. E. Yu, Y. Nomura, K. Nakamura, K. Kitamura, Y. Takada, J. Sakuma, and T. Sumiyoshi: Abstract of 2004 Spring Meeting of Applied Physics Society of Japan 29p-ZC-7 [in Japanese].

15) N.E. Yu, S. Kurimura, Y. Nomura, and K. Kitamura: Jpn. J. Appl. Phys. **43**, L1265 (2004).

16) A. Bruner, D. Eger, and S. Ruschin: J. Appl Phys. **96**, 7445 (2004).

17) H. Karlsson and F. Laurell: Appl. Phys. Ltt. **71**, 3474 (1997).

18) G. Rosenman, A. Skliar, D. Efer, M. Oron, and M. Katz: Appl. Phys. Lett. **73**, 3650 (1998).

19) S. Wang: “Fabrication and characterization of periodically-poled KTP and Rb-doped KTP for applications in the visible and UV,” Ph. D Thesis. ISBN 91-7178-153-6, Royal Institute of Technology, (2005).

20) J.-P. Meyn, M. E. Klein, D. Woll, R. Wallenstein, and D. Rytz: Opt. Lett. **24**, 1154 (1999).

21) J. H. Kim and C. S. Yoon: Appl. Phys. Lett. **81**, 3332 (2002).

22) V. Petrov, F. Noack, F. Rotermund, V. Pasiskevicius, A. Fragemann, F. Laurell, H. Hundertmark, P. Adel, and C. Fallnich: Jpn. J. Appl. Phys. **42**, L1327, (2003).

23) B. Zysset, I. Biaggio, and P. Gunter: J. Opt. Soc. Am. B **9**, 380 (1992).

24) Y. Zhang, B. Fluegel, and A. Mascarenhas: Phys, Rev. Lett. **91**, 157404 (2003).

25) G. D. Boyd and D. A. Kleinman: J. Appl. Phys. **39**, 3597 (1968).

Chapter 6. Comparison of laser-induced damage properties [Paper VII)]

6.1. Introduction

The high nonlinearities and the possibility for quasi-phase matched (QPM) non-critical interaction are the two main attractive features why ferroelectric crystals recently have become important in nonlinear optics. Advances in growth technology of these materials have to a large degree been stimulated by applications requiring more efficient all-solid-state visible lasers, particularly frequency doubled near-infrared lasers in the blue-green spectral region. Power handling and reliability of the frequency conversion stage is of critical importance for the laser performance. Nonlinear crystals employed in frequency conversion stages have to sustain near infrared and visible light intensities from several MW/cm^2 in continuous wave (CW) to tens of GW/cm^2 in pulsed systems. At these intensities ferroelectric crystals might exhibit an array of unwanted nonlinear effects, among which photorefraction and blue-green light-induced infrared absorption are the most damaging ones, appearing both in the CW and the pulsed regime. As these effects substantially limit the range of possible applications of the ferroelectric QPM crystals, it is not surprising that a substantial effort has been devoted by crystal growers in order to produce modifications of the most promising ferroelectrics, congruent $LiNbO_3$ (CLN) and $LiTaO_3$, so these would be less susceptible to the photorefractive effect. As a result, a number of materials have been developed, with $KTiOPO_4$ (KTP),[1)] MgO doped congruent $LiNbO_3$ (MgO:CLN),[2)] MgO doped stoichiometric $LiNbO_3$ (MgO:SLN) and $LiTaO_3$ (MgO:SLT),[3, 4)] and $KNbO_3$ (KN)[5)] as the most promising ones for QPM frequency conversion applications.

Blue or green light-induced infrared absorption (BLIIRA and GRIIRA, respectively), although not as damaging as photorefraction to the performance of the frequency converter, presents a latent problem in laser system with frequency conversion. For instance, the GRIIRA or BLIIRA in CW laser system with external-cavity resonant frequency doubling can be driven completely out of resonance by increasing of the thermal lens in the nonlinear crystal, rendering the whole system unusable. In pulsed systems the induced absorption causes slow power decrease and can eventually lead to a catastrophic optical damage. Light-induce absorption has been investigated before in the above-listed ferroelectrics.[6-15)] However the investigations have been mostly limited to the regime of relatively low intensities of CW or Q-switched sources and primarily using single-domain ferroelectric crystals. Applications of QPM crystal for frequency-conversion using picosecond and femtosecond lasers are growing in importance, but the issue of light induced absorption for high-peak intensity pulses has not been properly addressed so far, to the best of our knowledge. Moreover, in this short-pulse regime, the light-induced absorption can appear not only in frequency-doubling crystals but also in mid-infrared optical parametric amplifiers due to blue or green light generation by parasitic higher-order QPM processes.[16)] In this work we attempt to fill this void in knowledge by performing a systematic study of BLIIRA induced by 1 ps pulses in the 400 nm spectral regions.

In this chapter, we compare the BLIIRA properties of the most promising nonlinear ferroelectrics: MgO:SLN, MgO:SLT, SLT, KTP, and KN, as listed in Section 4.2.1, and 5 mol% MgO-doped congruent $LiNbO_3$ fabricated by the CZ method by Yamaju Ceramics Co. Ltd., which is denoted MgO:CLN below. The BLIIRA properties are discussed from the following three points of view: a) the dynamics of the inducing and the relaxing transition, b) the BLIIRA dependences on the induced blue light intensity, and c) differences of those properties in the unpoled and the periodically-poled materials.

6.2. The BLIIRA measurement setup

The BLIIRA measurement set up is shown in Fig. 6-2-1. In essence, it is a common-path interferometer similar to the devices reported previously.[12, 15, 17, 18)] Compared to previous reports, the present system uses picosecond blue pulses to induce IR absorption. Three laser beams were collinearly aligned through the sample: a probe beam at 633 nm (He-Ne) with 100 μm radius, a continuous wave pump beam at 1064 nm (Nd: YVO_4) with 20 μm radius. The pump laser generated 780mW of CW power in a TEM00 mode. The IR pump beam and was mechanically chopped in order to provide reference frequency for lock-in detection. The absorption-inducing blue light pulses at 410 nm were generated by a picosecond Ti:Sapphire regenerative amplifier, followed by a BBO frequency doubling stage. The fundamental was separated from the second harmonic beam by a dichroic mirror DM1. The power of the blue light was controlled by adjusting the power of the fundamental beam with a half-wave plate-polarizer arrangement. The pulse width of the blue light was approximately 1 ps generated at a repletion rate of 1 kHz. The blue beam was loosely focused to 200 μm radius in the sample. Finally the dichroic mirror DM3 reflected only the 632 nm probe beam into the detection system. All beams were polarized parallel to the spontaneous polarization vector of the ferroelectric samples. This polarization of light is the most commonly used in QPM devices.

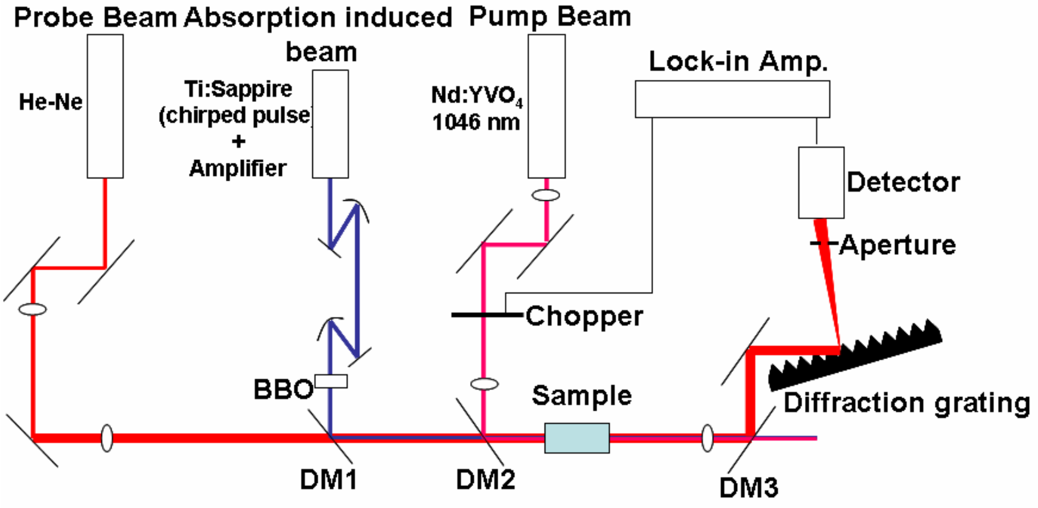

Figure 6-2-1. BLIIRA measurement set up.

The blue light can induce the IR absorption by creating color centers, polarons or temporarily altering stationary occupation states of the electron and/or hole trap levels due to intrinsic defects or extrinsic impurities. In any case, the absorption of the IR beam pump, in turn creates a thermal lens in the sample. The thermal change leaves an imprint i.e. leads to a spatial distortion of the phase front of the co-propagating probe beam. The phase modulation can be converted into an amplitude modulation in the Fourier plane. The spatial Fourier transform of the probe beam is accomplished by a f = 250 mm lens placed at the focal distance behind the sample. As the phase modulation by the thermal lens results in a modulation of the spreading angle of the probe beam, this effect can be further enhanced by proper placement of a diffraction grating behind the Fourier lens. Finally a Si *p-i-n* detector placed behind a 300 μm diameter aperture was positioned to monitor the highest spatial frequencies of the Fourier spectrum. So when the pump beam is switched off only a very small amount of the probe beam power can reach the detector. When the thermal lens is present, on the other hand, the probe power transmitted through the aperture increases dramatically. This arrangement gives a high signal-to-noise ratio and thus a high sensitivity. Additional BG 39 and OG 54 filters have been put in front of the detector aperture in order to suppress remnant pump and blue photons by additional four orders of magnitude. The detector signal was measured by a lock-in amplifier (SRS530) whose output was connected to an oscilloscope for BLIIRA trace recording.

The absolute absorption of the different samples were deduced by comparing their values with that of a BK7 optical glass (Schott glass BK7 517642) reference sample, with known material constants, and using the following equation for callibration:

$$\alpha_{sample} = \alpha_{BK7}\sqrt{\frac{S_{sample}}{S_{BK7}}}\,\frac{(dn/dT)_{BK7}\,\kappa_{sample}L_{BK7}}{(dn/dT)_{sample}\,\kappa_{BK7}L_{sample}}\,, \qquad (6\text{-}1)$$

where S_{sample}, S_{BK7}, and L_{sample}, L_{BK7} are the maximum lock-in signals measured in samples and BK7, and the sample lengths, respectively. The reported temperature derivatives of the refractive index, *dn/dT,* and the thermal conductivity, κ, are summarized in Table 6-2-1, which are used for calculation in this study. The infrared pump power was held constant throughout the measurement, while the peak intensity of the blue light through the measurements was changed from 35 MW/cm^2 to 12.5 GW/cm^2, corresponding to the average powers from 0.03 W/cm^2 to 11 W/cm^2, which is much lower than intensities typically used for CW BLIIRA characterization. So this arrangement can specifically give pulsed BLIIRA response which can differ substantially from the material response using CW absorption-inducing beams. The absorption measurement sensitivity of the current setup was better than 10^{-5} cm^{-1}.

	BK7 [19)]	KTP [15)]	MgO:CLN [20-21)]	MgO:SLN [20-21)]	MgO:SLT [21-22)]	KN [6, 23)]
dn/dT	9.84×10^{-7}	1.60×10^{-5}	3.44×10^{-5}	3.44×10^{-5}	2.01×10^{-5}	6.37×10^{-5}
κ [W/(cm K)]	1.11	13	4.63	5.62	4.82	4

Table 6-2-1. The reported temperature derivatives of the refractive index, dn/dT, and the thermal conductivity, κ*.*

6.3. The BLIIRA performance

As mentioned above, six different promising materials (MgO:SLN, MgO:CLN, MgO:SLT, SLT, KTP, and KN) were prepared. It should be mention that the growth method and post-growth processing history of the crystals are important factors that can affect the performance and reliability of the frequency doubling stage. In our case, we have had limited knowledge of the actual growth conditions. However each type of crystal was provided by a single vendor and our repeated measurements over different growth batches revealed surprisingly little variation in either the absolute values of initial and induced absorption or BLIIRA dynamics. All crystals were cut and polish in dimensions 10 mm × 5 to 10 mm (x, y) and with a thickness in the polar direction of either 1 or 2 mm. Half of the samples were periodically poled as shown in Fig. 6-3-1 by the electric-field poling techniques with 10-30 μm periodicities, as mentioned in Chapter 4, in order to compare the differences between the unpoled and the periodically-poled area of the same sample. The optical surfaces of the crystals were left uncoated. All crystals were annealed after poling to reduce eventual stress remaining in the samples which typically causes higher initial absorption of infrared light and in some cases can give photorefraction-like slow modulation of the measured signal[15].

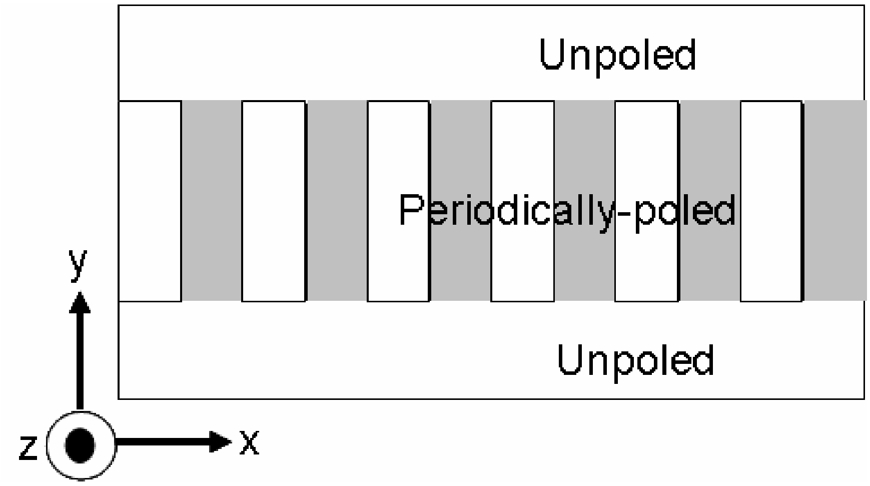

Figure. 6-3-1. Illustration of how unpoled and periodically-poled regions are made on the same substrate.

6.3.1. BLIIRA transitions when switching blue light on and off

We measured intrinsic IR absorption of the ferroelectric crystals at the pump wavelength without presence of the blue-light pulses. The measured absorption in KTP, KN, MgO:CLN, MgO:SLN, and MgO:SLT were 7.6×10^{-4} cm^{-1}, 1×10^{-5} cm^{-1}, 1×10^{-4} cm^{-1}, 1.3×10^{-4} cm^{-1}, and 3.8×10^{-4} cm^{-1}, respectively. The poled samples showed only marginally higher absorption, and the difference from single-domain samples being close to the sensitivity limit of the setup. This small difference is inconsequential and might be an indication of some remaining electrochromic effect introduced during poling and not totally annealed away after poling. It should be pointed out that for all poled samples the domain inversion period had been carefully chosen not to correspond to any QPM process either for the 410 nm blue light or the near-infrared pump beam.

Next, we studied the dynamics of the BLIIRA after switching on and off the absorption-inducing blue beam. A typical example of the dynamics for the different crystals is shown in Fig. 6-3-2, where Fig. 6-3-2(a) shows rise of the BLIIRA after switching on the blue-pulses while the Fig. 6-3-2(b) shows the BLIIRA relaxation dynamics. Here the peak intensity of the blue pulses for all materials except KN was 1.2 GW/cm^2, corresponding to an average intensity of only 1.0 W/cm^2. For KN and PPKN, we had to increase the intensity to 2.8 GW/cm^2 in order to obtain substantial enough BLIIRA. Note that the traces in Fig. 6-3-2 are normalized to the intrinsic near-IR absorption given above. Moreover, for the sake of clarity in the Fig. 6-3-2 we present only the traces for single-domain crystals because the response in periodically poled materials was qualitatively the same except the BLIIRA values were higher, as will be shown below.

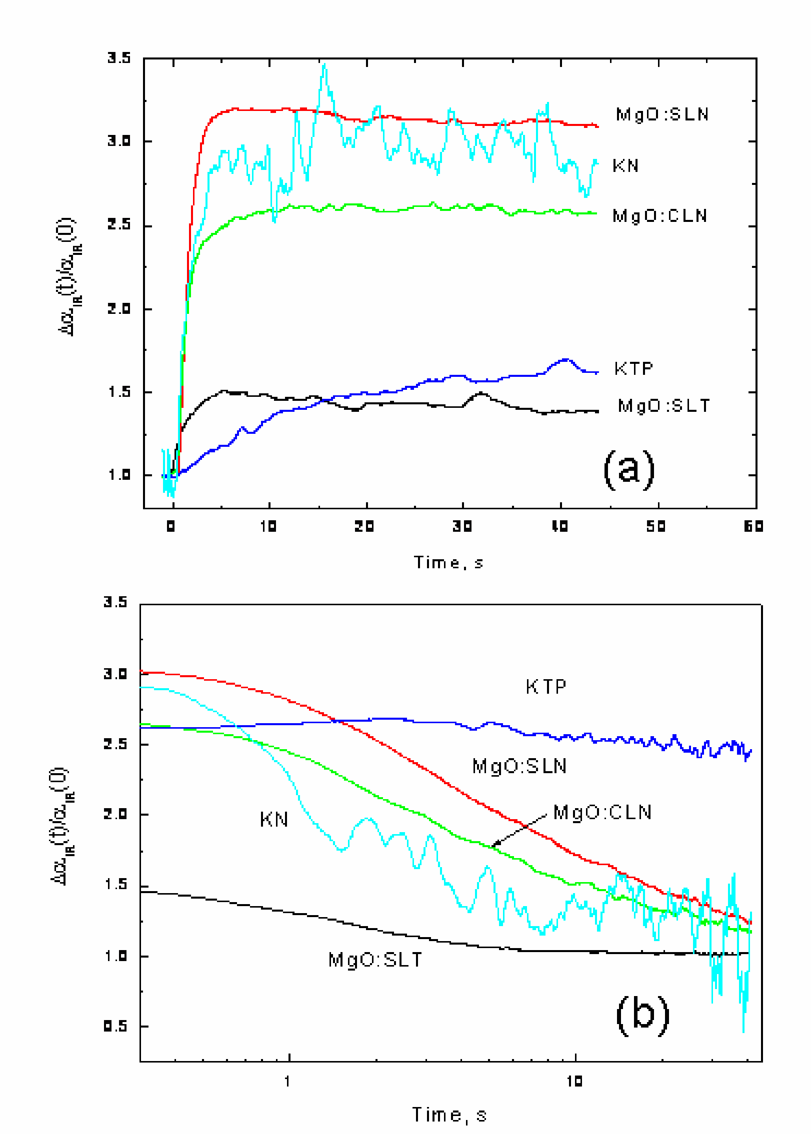

Figure 6-3-2. Dynamics of induced absorption normalized to the absorption coefficient before blue light illumination. Rise of BLIIRA (a), Relaxation of BLIIRA (b). The peak intensity of blue light is 1.2 GW/cm^2 for all materials except for KNbO$_3$ where the peak intensity is 2.8 GW/cm^2 .

From the traces in Fig. 6-3-2 we have the following observations: i) the rise and relaxation of the BLIIRA in all materials except KTP was of the order of 1 s to 2 s which is the temporal resolution of the lockin amplifier. ii) The saturation value of BLIIRA was reached within less than 10 s in all materials except KTP, which reached stationary induced absorption level in approximately 2 to 5 minutes. iii) The induced absorption in KN (and PPKN) for these excitation conditions is remarkably low, which is in stark contrast to the strong BLIIRA response under CW excitation conditions.[6, 7] iv) After the blue pulses have been switched off the relaxation of BLIIRA proceeds non-single-exponentially in all materials, but the relaxation is substantially slower in KTP. The double exponential decay fit to the relaxation traces give the time constants of 2 s and 4.5 s for MgO:SLT, while for MgO:SLN and MgO:CLN the relaxation is very similar with two time-constants of 6 s and 10 s. The relaxation of BLIIRA in KTP is very similar to that reported for

GRIIRA[15] and it takes several days for the increased absorption value in the excitation spot to disappear at room temperature. Complementing the traces of Fig. 6-3-2, the traces in Fig. 6-3-3 show relaxation of BLIIRA in MgO:PPSLT, MgO:PPSLN and PPKTP for different blue light peak intensities. Here the traces are normalized to the maximum BLIIRA value. Within the temporal resolution of the experiment the relaxation in MgO:PPSLT and MgO:PPSLN does not depend on the intensity of the blue pulses while PPKTP shows initial increase in the relaxation rate for higher peak intensities. Again this is consistent with the KTP GRIIRA reponse.[15]

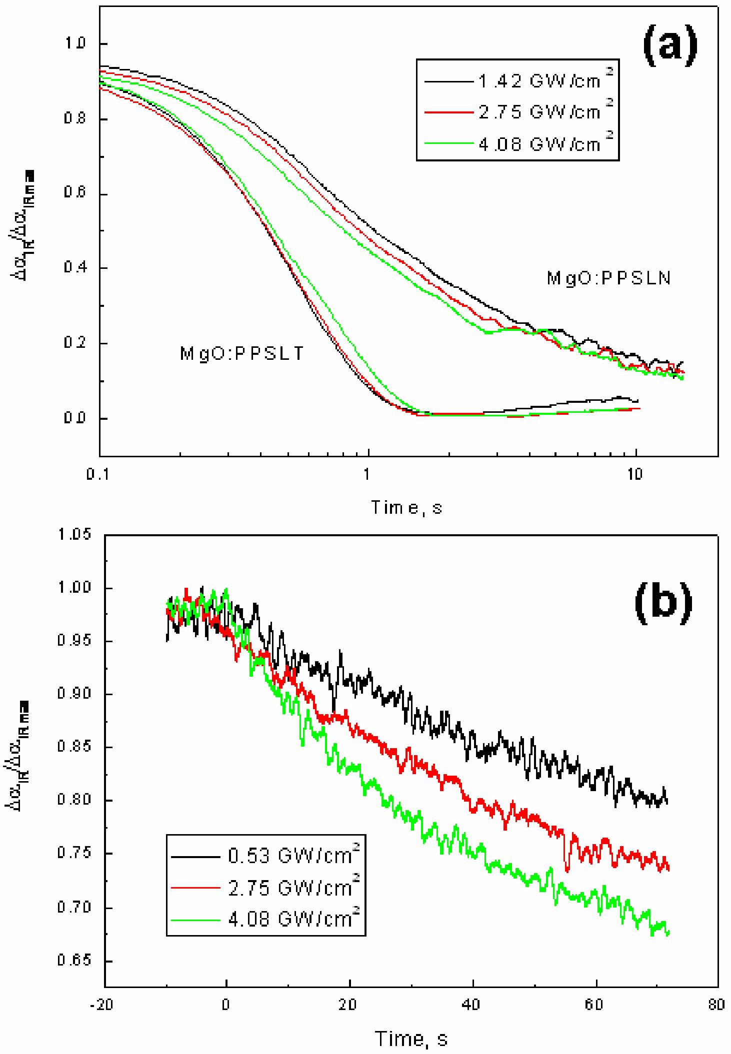

Figure 6-3-3. Comparison of BLIIRA relaxation for different blue-light excitation intensities in MgO:PPSLT and MgO:PPSLN (a) and PPKTP (b).

The character of the BLIIRA dynamics suggests that the induced absorption in KN, MgO:SLN, MgO:CLN and MgO:SLT are related to the trap filling dynamics by the charge carriers excited by the blue light pulses. The 410 nm photons are within the bangap in those ferroelectrics, however, two photon absorption is very likely especially for picosecond pulses. Moreover, there might be impurities and tails in the density of states in the conduction band which would allow charge carrier generation by linear absorption. There are several possible electron and hole trapping mechanism in

MgO:SLN, MgO:CLN and MgO:SLT. For instance, Nb_{Li}^{4+} antisite defect can act to be a center for electron small polaron formation at least in MgO:CLN.[11, 24] It should be noted that the Mg doping and near-stoichiometric crystal composition are supposed to reduce the concentration of Li vacancies and thus the concentration of the Nb_{Li}^{4+} defect should also be reduced. However our results show that BLIIRA and the reported GRIIRA are higher in crystals with close to stoichiometric composition.[11] Another candidate for induced infrared absorption might be a small hole polaron formed at O^- near Li vacancy.[25] Clearly unintended doping with impurities such as Fe cannot be excluded.

In KTP, on the other hand the BLIIRA dynamics and it's dependence on peak intensity of the blue light suggests that carrier ambipolar carrier diffusion and associated K^+-ion and local $V(K^+)$ vacancy redistribution might be involved in formation of color centers. KTP is a well known ionic conductor, where the conduction is provided by a vacancy $V(K^+)$ hopping mechanism. These vacancies can also stabilize the O^{2-}/O^- hole trap and the Ti^{4+}/Ti^{3+} electron trap.[15, 26] At least the latter electron trap has absorption in the near infrared spectral region. Excitation by the blue light generates a radial free carrier concentration gradient and also a pyroelectric field. Ambipolar diffusion of carriers build up a space charge field around the beam and causes loosely bound K^+ ions and $V(K^+)$ to move in order to screen the field. This process should change the net $V(K^+)$ concentration in the beam area thus allowing a higher concentration of carrier trap centers.

6.3.2. The BLIIRA dependences on the pulse intensities

It is important to investigate the dependencies of the stationary induced absorption in single-domain and periodically poled samples on the peak intensity of the blue light. The plotted values in Fig. 6-3-4 are the induced absorption value after blue light irradiation for 6 min. First, in the low blue light power regime, no induced absorption was observed at peak intensities lower than 35 MW/cm^2 for KTP and PPKTP, 75 MW/cm^2 for PPMgO:SLT, 150 MW/cm^2 for MgO:SLT, and 250 MW/cm^2 for KN and PPKN. However, both MgO:CLN and MgO:SLN show BLIIRA at blue light intensity as low as 35 MW/cm^2. Compared to MgO:CLN, MgO:SLN, and MgO:SLT this result is in good agreement with an earlier report showing a lower green-light induced absorption (GRIIRA) threshold for MgO:SLT.[10] It is worth noting that in the case of both unpoled and periodically poled non-doped stoichiometric $LiTaO_3$, which is also grown by double-crucible Czochralski method, the probe beam was completely distorted after a few seconds by photorefraction even at a blue light peak intensity of 35 MW/cm^2 (which corresponds to only 0.03 W/cm^2 of the average intensity).

In the high power regime, the induced absorption in MgO:CLN, MgO:SLN, and KN are saturated at a blue peak intensity lower than 2 GW/cm^2. In KTP the BLIIRA saturates at peak intensities of around 4 GW/cm^2. Such saturation behavior has also previously been observed in KTP.[13] On the contrary, the induced absorption in MgO:SLT and MgO:PPSLT increases approximately linearly with the blue peak intensity at least up to 8 GW/cm^2. This is very clearly seen in Fig. 6-3-5, where the relative change in IR absorption is shown as a function of blue peak power for the periodically poled crystals. The solid line is a linear fit to the MgO:PPSLT data points. At the peak power of 8 GW/cm^2 the relative increase of IR absorption in MgO:PPSLT is equal to that of the PPKTP. So our results show that in comparison to MgO:SLN, the MgOSLT has higher peak intensity threshold for BLIIRA but at the same time a stronger dependence of the induced absorption on the blue light intensity at least in the intensity region used in our experiment. Considering that Mg doping concentration and stoichiometry can be tuned during crystal growth it is feasible to expect that MgO:SLT with lower susceptibility to induced absorption would be produced in the future.

The data in Fig. 6-3-4 shows that BLIIRA is higher in the periodically poled samples for all materials studied. This is especially notable in PPKTP and MgO:PPSLT. Similar tendency was reported for GRIIRA in PPKTP.[15] The higher susceptibility to the induced absorption can be expected in periodically poled crystals, considering that the electric field poling induces stresses in the material and might be responsible to creation or gettering native crystal defects in the regions close to the ferroelectric domain walls. Moreover it is interesting to note that BLIIRA in MgO:SLN is always stronger than in MgO:CLN. This might be attributed to the higher concentration of MgO doping in MgO:CLN which helps to reduce the concentration of Nb_{Li}^{4+} defects acting as pinning centers for small electron polarons.

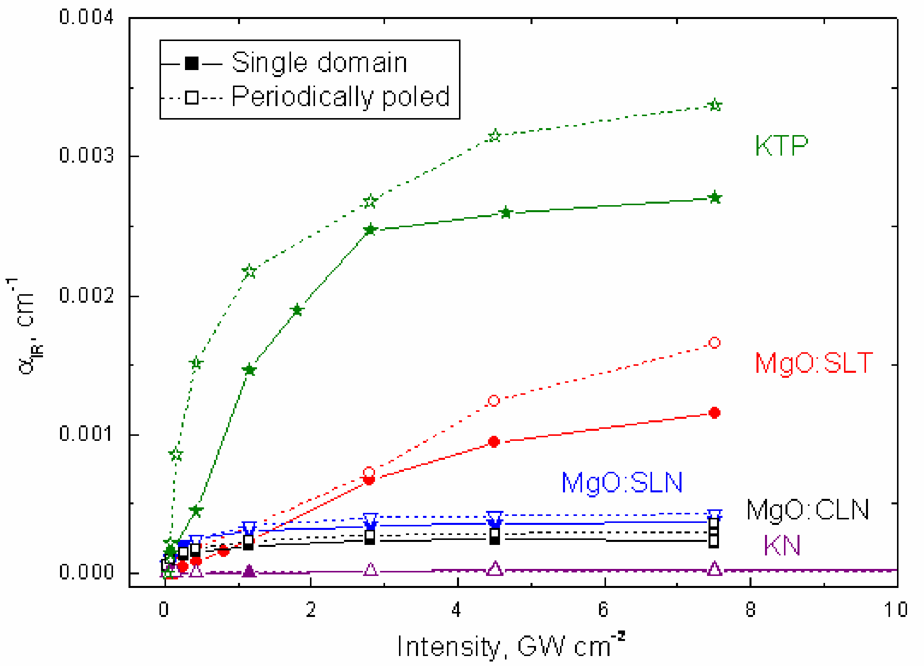

Figure 6-3-4. Dependence of the absorption coefficient at 1064 nm on the peak power of the blue light in single-domain (solid symbols and solid lines) and periodically poled (open symbols and dashed lines) crystals: KTP (stars), MgO:SLT (circles), MgO:SLN (down-triangles), MgO:CLN (squares), KN (up-triangles).

It is also remarkable that KN and PPKN showed a very low change in the infrared absorption under blue light irradiation, although rather substantial BLIIRA in KN has been reported previously,[6, 7] although obtained at rather high blue average intensities of about 1 kW/cm^2. Our results would corroborate the three-trap level scheme proposed tentatively in Ref. 7. According to that scheme there should be a very shallow hole trap level with fast capture and re-excitation exchange dynamics with the valence band. This level is responsible for BLIIRA induced by short low-average intensity pulses. At higher average intensities, the deeper traps become increasingly populated by holes. These traps have much slower response producing strong integrated BLIIRA response to the CW blue light excitation. What could be the origin of these traps is not clear at the moment.

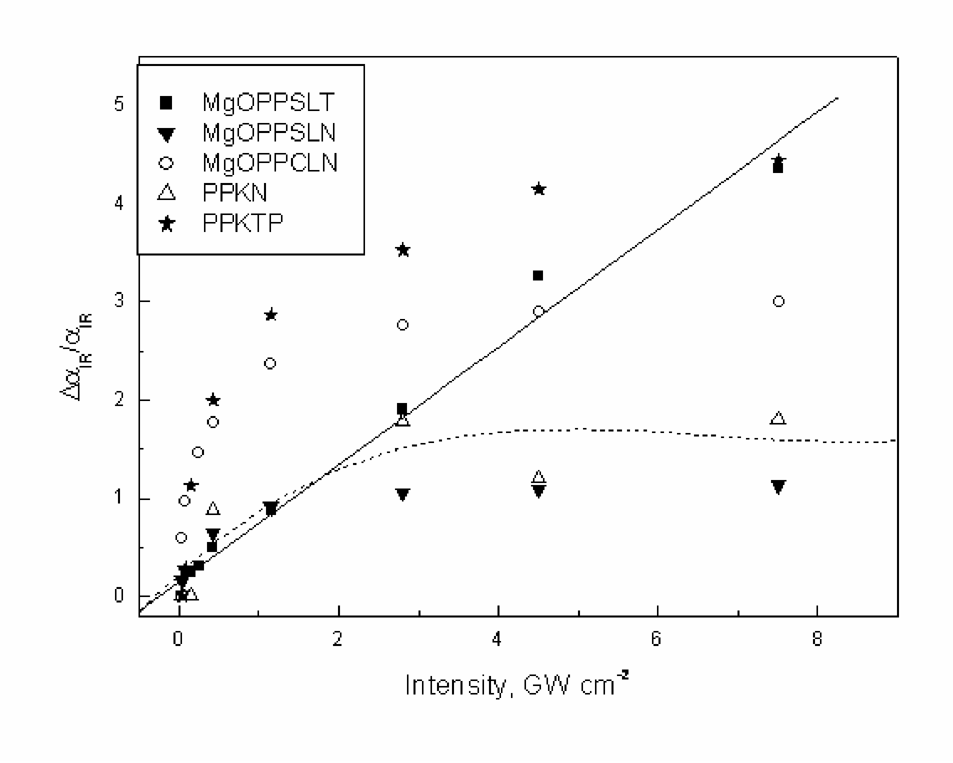

Figure 6-3-5. BLIIRA normalized to the initial infrared absorption in periodically poled crystals: PPKTP (solid stars), MgO:PPSLT (solid squares), MgO:PPSLN (solid down triangles), MgO:PPCLN (open circles), PPKN (open triangles). Solid line is a linear fit to the MgO:PPSLT data, dashed line – polynomial fit to the PPKN data.

6.4. Summary

BLIIRA has been investigated for the unpoled and the periodically poled KTP, MgO:CLN, MgO:SLN, MgO:SLT, and KN materials. The results are summarized from the three following points:

a) Dynamics of the inducing and the relaxing transition:

The rise and the relaxation times of the BLIIRA in all of the materials above, except KTP, was of the order of 1 s to 2 s. The saturation value of the BLIIRA was reached within less than 10 s in all of the materials, except for KTP, which reached a stationary level of the induced absorption in approximately 2 to 5 minutes. After the blue pulses have been switched off, the relaxation of BLIIRA proceeds not single-exponentially in all materials, particularly, the relaxation is substantially slower in KTP. The fit of the double exponential decay fit to the relaxation traces gives the time constants of 2 s and 4.5 s for MgO:SLT, while for MgO:SLN and MgO:CLN the relaxation is very similar with two time-constants of 6 s and 10 s.

b) The BLIIRA dependences on the induced blue-light intensity:

The highest BLIIRA thresholds were observed in MgO:SLT and KN. However, SLT showed a strong photorefraction even at a blue-light peak intensity of 35 MW/cm^2 (which corresponds to only 0.03 W/cm^2 of average intensity). KN, MgO:CLN, and MgO:SLN show the lowest susceptibility to BLIIRA. A strong dependence of BLIIRA on the peak intensity of the excitation in MgO:SLT, at high blue peak power, was observed. This trend can be more critical for the device reliability in high power applications. For MgO:SLT and MgO:SLN, there are two degrees of freedom for future material improvement, namely, the MgO doping concentration and the stoichiometry. By properly understanding the interplay of these parameters and their effect on the photorefraction and the light-induced absorption, the materials will be optimized.

c) The differences of those properties in the unpoled and the periodically-poled materials:

Periodic-poling slightly increases the susceptibility to the induced absorption in all of the materials, especially for KTP, MgO:SLT, and KN. However, no remarkable differences were observed in the BLIIRA dynamics.

References in Chapter 6

1) H. Karlsson and F. Laurell, Appl. Phys Lett. **71**, 3474 (1997).

2) K. Mizuuchi, A. Morikawa, T. Sugita, and K. Yamamoto, Jpn. J. Appl. Phys. **42**, L90 (2003).

3) L. Huang, D. Hui, D.J. Bamford, S.J. Field, I. Mnushkina, L. E. Myers, and J. V. Kayser, Appl. Phys. B, **72**, 301 (2001).

4) N.-E. Yu, S. Kurimura, Y. Nomura, M. Nakamura, K. Kitamura, Y. Takeda, J. Sakuma, and T. Sumiyoshi, Appl. Phys. Lett., **85**, 5134 (2004).

5) J. Hirohashi, K. Yamada, H. Kamio, and S. Shichijyo, Jpn. J. Appl. Phys, **43**, 559 (2004).

6) L. E. Busse, L. Goldberg, M. R. Surette, and G. Mizell, J. Appl Phys. **75**, 1102 (1994).

7) H. Mabuchi, E. S. Polzik, and H. J.Kimble, J. Opt. Soc. Am. B, **11**, 2023 (1994).

8) K. Buse, and E. Krätzig, Opt. Mater. **1** 165 (1992).

9) H. Qiao, and Y. Tomita, Optics Express, **14**, 5773 (2006).

10) K. Kitamura, Y. Furukawa, S. Takekawa, T. Hatanaka, H. Ito, and V. Gopalan, Ferroelectrics **257**, 235 (2001).

11) Y. Furukawa, K. Kitamura, A. Alexandrovski, R. K. Route, M. M. Fejer, and G. Foulon, Appl. Phys. Lett. **78**, 1970 (2001).

12) A. L. Alexandrovski, G. Foulon, L. E. Myers, R. K. Route, and M. M. Fejer, Proc. SPIE **3610**, 44 (1999).

13) B. Boulanger, I. Rousseau, J. P. Féve, M. Maglione, B. Menaert, and G. Marnier, IEEE J. Quant. Electro. **35**, 281 (1999).

14) S. Wevering, J. Imbrock, and E. Krätzig, J. Opt. Soc. Am. B, **18**, 472 (2001).

15) S. Wang, V. Pasiskevicius, and F. Laurell, J. Appl. Phys. **96**, 2023 (2004).

16) F. Rotermund, V. Petrov, F. Noack, V. Pasiskevicius, J. Hellström, and F. Laurell, Optics Lett. **24**, 1874 (1999).

17) A. Marcano, O. C. Loper, and N. Melikechi, Appl. Phys. Lett., **78**, 3415 (2001).

18) M. Roth, N. Angert, M. Tseitlin, and A. Alexandrovski, Optical Mater., **16**, 131 (2001).

19) Schott glass catalogue.

20) D. S. Smith, H. D. Riccius and R. P. Edwin, Opt. Comm. **17**, 332 (1976).

21) K. Kitamura, S. Takekawa, and H. Haneda, Oyo buturi **74**, 573 (2005).

22) A. Bruner, D. Eger, M. B. Oron, P. Blau, M. Katz, and S. Ruschin, Opt. Lett., **28**, 194 (2003).

23) B. Zysset, I. Biaggio and P. Gunter, J. Opt. Soc. Am. B **9**, 380 (1992).

24) G. Kh. Kitaeva, K. A. Kuznetsov, A. N. Penin, and A. V. Shepelev, Phys. Rev. B, **65**, 054304 (2002).

25) P. Herth, T. Granzow, D. Schaniel, Th. Woike, M. Imlau, and e. Krätzig, Phys.Rev. Lett. **95**, 067404 (2005).

26) V. Mürk, V. Denks, A. Dudelzak, P.-P. Proulx, and V. Vassilitsenko, Nuclear Inst. And Meth. B, **141**, 472 (1998).

Chapter 7. Description of the original work and contribution by the candidate

Paper I: Polarization switching characteristics of flux grown $KTiOPO_4$ and $RbTiOPO_4$ at room temperature

C. Canalias, J. Hirohashi, V. Pasiskevisius, and F. Laurell:
J. Appl. Phys. **97**, 124105 (2005).

A study of polarization-switching characteristics under an applied electrical field at room temperature is presented for flux-grown $KTiOPO_4$ and $RbTiOPO_4$. By optimizing the experimental conditions, we determined the coercive field and the domain-switching time quantitatively by direct observation of the switching current. For both isomorphs, the inverse of the polarization-switching time, $1/t_s$, follows an exponential dependence on the applied field E in the low-field regime, and a linear dependence on E in the high-field regime. Domain morphology of $KTiOPO_4$ based on selective etching reveals laminar structures elongated in the b crystallographic direction. An estimation of the domain-wall velocity shows that the domain speed in the polar direction is, at least, two orders of magnitude larger than in the *a-b* plane. The velocity along the *b*-direction is ~30 times larger than along the a-axis.

Contributions by the candidate: The candidate introduced the measurement method of threshold voltages and modified the poling set-up together with C. Canalias and V. Pasiskevisius. Almost all of the experiments were done by C. Canalias. The paper was written together.

Paper II: Embryonic nucleation method for fabrication of uniform periodically poled structures in potassium niobate for wavelength conversion devices

J. Hirohashi, K. Yamada, H. Kamio, and S. Shichijyo:
Jpn. J. Appl. Phys. **43**, 559 (2004).

A new electric-poling concept called the ‘Embryonic Nucleation Method’ for fabrication of periodically-poled structures was presented. By applying this method to $KNbO_3$, a 1-mm-thick uniform PPKN with domain-inverted period of 35.5 μm and an interaction length of 10 mm has been successfully fabricated by applying only 300 V/mm without generation of unwanted domains. Furthermore, the reproducibility of the periodic-poling process has been greatly improved. Second-harmonic generation using PPKN fabricated by this method was demonstrated and 100 mW second-harmonic generation at the wavelength of 532 nm was obtained at 40°C from 1W pumping without photorefractive damage.

Contributions by the candidate: The candidate constructed the poling set-up and poled all of the crystals. The second-harmonic measurement was done by S. Shichijyo and the candidate together. The candidate was responsible for writing the paper.

Paper III: Controllability of specific domain structures in $KNbO_3$ single crystals by electric poling at room temperature

J. Hirohashi, K. Yamada, H. Kamio, M. Uchida, and S. Shichijyo:
J. Appl. Phys. **98**, 034107 (2005).

Controllability of specific domain structures in $KNbO_3$ single crystals was investigated by electric field poling for several different orientations at room temperature. By applying an electric field to the direction that is corresponding to the difference direction between the original and the intended spontaneous polarization direction (differential vector poling (DVP) method), 60°-, 90°-, and 180° domain pairs were successfully fabricated in $KNbO_3$. The threshold electric field for 90° domain pairs was the lowest (140 V/mm), which could be related to the difference between the piezoelectric coefficients and the poling direction. For the 60°- and 90°-domain pairs, theoretical uncharged domain walls were fabricated under control without generation of other domains. For the 120° domain pairs, $(011)_{pc}$ uncharged domain wall was not observed, which suggests the difficulty of the generation of an uncharged 120° domain wall without passing through the phase transition.

Contributions by the candidate: The candidate introduced the original concept and did all of the experiments by himself. K. Yamada, H. Kamio and M. Uchida provided the $KNbO_3$ single crystals. The candidate was responsible for writing the paper.

Paper IV: Fabrication of 90°-domain structures in $KNbO_3$ single crystals

J. Hirohashi, K. Yamada, H. Kamio and S. Shichijyo:
Ferroelectrics **282**, 29 (2003).

90° domain structures could be fabricated in a $KNbO_3$ single crystals fr the first time by applying an electric field at room temperature. The coercive electric field of the 90° domain is very low (140 V/mm) compared with that of a 180° domain (250 V/mm). A very sharp boundary was observed across the whole sample thickness (2 mm). Fabricated 90° domain structures were also confirmed by the (101) surface profile measurement using the optical interferometer and two peaks of the 404 X-ray diffraction analysis. We also demonstrated the fabrication of periodic 90° domain structures with a 200 μm period without generating any unwanted domains. As the 90° domain structure feels the difference of the refractive index, new applications other than those for pure 180° domains will be possible.

Contributions by the candidate: The candidate made the poling set-up and did all of the experiments by himself. K. Yamada and H. Kamio provided the $KNbO_3$ single crystals. The candidate was responsible for writing the paper.

Paper V: Quasi-phase-matched frequency conversion in $KNbO_3$ structures consisting of 90° ferroelectric domains

J. Hirohashi and V. Pasiskevicius:
Appl. Phys. B **81**, 761 (2005).

Periodic 90° domain structure with 18.6 μm periodicity was fabricated by applying a 200 V/mm electric field over a (101)-cut $KNbO_3$ plate. Blue-light generation by quasi-phase-matched frequency doubling in this periodic 90° domain structure was demonstrated. The 90° domain structure completely compensates for a Poynting vector walk-off of the second-harmonic beam. Moreover, these structures exhibit amphoteric Poynting vector refraction properties, i.e., the refraction can be negative or positive depending on the angle of incidence at the 90° domain boundary.

Contributions by the candidate: The candidate poled the materials and calculated the phase matching conditions. The second-harmonic measurement was done by V. Pasiskevicius and the candidate together. V. Pasiskevicius and the candidate wrote the paper together.

Paper VI: Total Refraction of P-polarized light at the 90-degree domain boundary in the ferroelectric crystal

S. Shichijyo, J. Hirohashi, H. Kamio and K. Yamada:
Jpn. J. Appl. Phys. **43**, 3413 (2004).

A 90°-domain structure was fabricated using electric field poling in ferroelectric birefringent $KNbO_3$ crystal. The refraction and reflection characteristics of the light at the boundary of the 90°-domain structure were investigated, and the novel behavior of total refraction (no reflection) has been found for the P-polarized light throughout the entire range of incident angle ($0° < \theta < 90°$). Strong refraction of the light was observed after it exits the crystal output surface at the incidence parallel to the domain boundary. These behaviors were explained analytically.

Contributions by the candidate: The candidate poled the crystals which were used in the experiment. The optical measurements were done by S. Shichijyo and the candidate together. The theoretical introduction was done by S. Shichijyo. K. Yamada and H. Kamio provided the $KNbO_3$ single crystals. S. Shichijyo was responsible for writing the paper.

Paper VII: Picosecond blue light-induced infrared absorption in single-domain and periodically poled ferroelectrics.

J. Hirohashi, V. Pasiskevicius, S. Wang, and F. Laurell:
Submitted to J. Appl. Phys.

Picosecond blue light-induced infrared absorption is investigated in bulk and periodically poled ferroelectrics known to have high photorefractive resistance ($KTiOPO_4$, MgO-doped congruent-$LiNbO_3$, MgO-doped stoichiometric-$LiNbO_3$, MgO-doped stoichiometric-$LiTaO_3$, and $KNbO_3$). $KNbO_3$ and MgO-doped congruent and stoichiometric-$LiNbO_3$ show the lowest susceptibility to induced absorption. Periodic poling slightly increases the susceptibility to the induced absorption in all materials but the most noticeably in $KTiOPO_4$, MgO-doped Stoichiometric-$LiTaO_3$, and $KNbO_3$. Different dynamics of induced absorption is investigated. Relatively high thresholds for induced absorption were observed in MgO-doped stoichiometric $LiTaO_3$ and $KNbO_3$. By increasing the peak power intensity of blue light, the induced absorption for $LiNbO_3$, $KTiOPO_4$ and $KNbO_3$ are saturated while in MgO-doped stoichiometric $LiTaO_3$ the induced absorption increases almost linearly with the blue peak intensity. The low susceptibility to induced absorption observed in $KNbO_3$ corroborates well with the earlier proposed existence of very shallow traps close to the valence band.

Contributions by the candidate: The candidate constructed the measurement set-up and did the characterizations together with V. Pasiskevicius and S. Wang. The samples were prepared by the candidate. The candidate was responsible for writing the paper.

Chapter 8. Summary

In this thesis work, several novel ferroelectric materials have been investigated for their employment in nonlinear optical applications; especially, quasi-phase-matching (QPM) devices, consisting of periodically-poled structures have been considered. Selected promising candidates are drawn from the following types of ferroelectric materials: 1) MgO-doped stoichiometric $LiNbO_3$ (MgO:SLN) and $LiTaO_3$ (MgO:SLT), and non-doped stoichiometric $LiTaO_3$ (SLT), 2) $KTiOPO_4$ (KTP) and its isomorphs $RbTiOPO_4$ (RTP), and 3) $KNbO_3$ (KN). Focus has been put on the following salient points of view: a) spontaneous polarization switching phenomena, b) optimization of the periodic-poling conditions, and c) photochromic optical damage properties characterized by blue light-induced infrared absorption (BLIIRA) measurement.

Employing electrical studies for the spontaneous polarization switching, we were able to determine quantitatively and to compare the values of the coercive field for the different materials by applying triangularly shaped electric fields. We found that the coercive fields depended on the ramp of the applied voltage and that KN had the lowest coercive field (less than 0.5 kV/mm) followed by KTP, SLT, and MgO:SLT (1.5 to 2.5 kV/mm). MgO:SLN and RTP showed relatively high coercive fields of approximately 5.0 to 6.0 kV/mm, respectively. The electrical current contribution, due to the material conductivity measured during poling, reduced the reliability of the current monitoring as a sole poling control technique for MgO:SLN, and for KTP and its isomorphs. Furthermore the domain switching and stabilization time of MgO:SLN, SLT, and MgO:SLT were all considerably longer than the other materials, which might be related to a higher surface capacitance.

The ferroelectric domain morphology, which is very important for designing the QPM grating direction, was characterized by selective etching. MgO:SLN, MgO:SLT, and SLT all showed a hexagonal domain nuclei shape whose main side was along the X-direction. On the contrary, KTP and KN both showed primarily a rectangular domain shape. We found that the domain anisotropy of KN was strongly related to the displacement of the O^{2-} ions before and after the switching of the spontaneous polarization.

Throughout our test fabrication of numerous periodically-poled structures, the important conditions such as the applied electric field, the electrode structures, and the serial resistances in the electric circuits were optimized by using the results obtained from the in-situ monitoring of the second-harmonic generation, the electro-optic responses, and the integration of charge flow. We found that the most critical parameter for obtaining homogeneously periodically-poled structures of MgO:SLN, SLT, and MgO:SLT was the homogeneity of the electrical contacts. It might possibly caused by the hexagonal domain morphology. The other important material property in those three materials is the large surface capacitance, which might be strongly related to the nucleation and backswitching process. We arranged the pulse amplitudes and shapes of the applied electric field in order to nucleate new domains homogeneously and to prevent undesirable backswitching. For KTP and KN, it was possible to create homogeneous periodically-poled structures with the conventional type of liquid electrode contacts. We have successfully fabricated structures and devices in all the materials mentioned with 30 μm periodicities and sample thicknesses of 1 mm. By measuring their performance in an optical parametric oscillator, pumped by a 5 ns pulsed Nd:YAG laser, the quality of the periodically poled structures, the effective nonlinearity, the conversion efficiency and the damage threshold could be compared with our standard PPKTP. The estimated effective nonlinear coefficient, d_{eff}, was almost 30% larger for the case of PPMgO:SLN and almost similar for the case of PPMgO:SLT and PPSLT as compared with that of PPKTP. However, nonlinear diffraction was observed in the as-fabricated PPMgO:SLT, PPSLT, and the PPMgO:SLN structures even after annealing. This might be due to the curtain-like domain-wall structures of these devices. PPMgO:SLN devices had a lower threshold power of mechanical break-down compared with that of

PPKTP in the OPO experiment, which might be caused by photorefraction in the MgO:SLN material. The PPKN devices also had lower threshold power of mechanical break-down in the OPO experiment when pumped by the 1 ns-pulsed laser. This break-down might be related to the generation of 90°-domains as caused by a change of the specific heat in the material.

Apart from the typical anti-parallel 180°-domains we primarily have investigated, we have also demonstrated the fabrication of periodic, non-180°-domain structures in KN for the first time and compared that with the 90°-domains in the same material. In this configuration, the walk-off process in each domain was compensated for by the periodic-domains and no reflection was observed at the domain boundaries even though the directions of the crystallographic axis changed at each adjacent domain boundary. Blue light generation was successfully obtained by QPM-SHG by using such a device with an 18.6 μm periodicity.

Blue light-induced infrared absorption processes (BLIIRA) were investigated for the listed materials, both using unpoled bulk and periodically-poled devices with a high-sensitivity, thermal-lens spectroscopic technique. SLT showed a huge photorefraction effect and the BLIIRA signal could not be properly measured because of the substantial distortion of the probe beam. In contrast to this, KN and MgO:SLN showed the lowest susceptibility to the induced absorption. Periodic poling slightly increased the BLIIRA susceptibility in the case of KTP, MgO:SLT, and KN. A higher BLIIRA threshold was observed for MgO:SLT and KN. By increasing the peak power intensity of the blue light, the induced absorption for MgO:SLN, KTP and KN saturated immediately, while that of MgO:SLT continued to increase. This trend is quite critical for device reliability in high-power applications. The transition and the relaxation times of BLIIRA were within the span of 10 to 30 sec except for KTP and its isomorphs, which needed minutes to hours in order to saturate at a certain fixed value.

QPM devices are now starting to be recognized as possible commercial products for many nonlinear optical applications, but, still they have not been able to find their place in many of the envisioned applications which are potentially of great interest and promises. Behind all of this, there are still many unknown problems which one need to overcome and which are always going back to the many subtle material qualities and fabrication processes of both the crystal growth and the preparation of the periodically-poled structures. I humbly hope the results and the discussions given in this thesis will become helpful for future investigations of the fabrication and the characterization of both the ordinary and the new promising periodically-poled materials.

Acknowledgement

First, I would like to thank Professor Fredrik Laurell for accepting me to join his research projects at KTH. During my time in his group, my scientific experience has been extremely expanded. That is because of his wide view of thinking and an extended variety of scientific and industrial connections over the whole world. In addition, he has always considering positive alternatives for me, and that was made me very satisfied all the time during my stay at KTH.

Secondly, I am gratefully appreciating Dr. Valdas Pasiskevicius for guiding me in the field of optics. His enormous knowledge, huge experience, and a wide view of the futures of this research have still enhanced me very much. His advices on various topics have made me more scientifically aware than before.

I am also very glad to thank the members of Mitsui Chemicals, Inc. (MCI), Japan. Especially Dr. Shiro Shichijyo has given me a lot in the way of in scientific thinking. Mr. Kazuhiro Yamada, also, gave me the essence of the art of crystal growth and materials characterization. During my time at MCI, they were always cheering me up and spending much time for discussions. I have entered this field of ferroelectric research in October 2000. At that time, since the MCI had a crystal-growth technology for $KNbO_3$ and the market for $KNbO_3$ single crystals was increasing, MCI were planning to expand the $KNbO_3$ operations combining it with domain-engineering techniques. So I was engaged in developing domain engineering of $KNbO_3$. For the first job I was put in charge of ordering a high-voltage power supply. Since nobody in the company had any experiences in the poling procedures, it was not possible to gain any detailed answers or correct indications from my superiors, however, this fact made me more independent and technically speaking much stronger than before. I would also like to thank the other colleagues at MCI, Masao Uchida, Hiroyuki Kamio, Susumu Kato, Takashi Takaya, Shoichi Shinoda, Kazumi Itakura, and Yuka Shimizu with whom I collaborated. They prepared the $KNbO_3$ samples very properly and maintained the high quality for these strange and inconvenient crystals. Since the MCI terminated the business of crystal research during my visiting-scientist program at the Laurell's group at KTH, unfortunately, I needed to leave the company in order to continue my research interest in this very attractive field. However, I am very proud and grateful foe having worked with all those nice colleagues at MCI.

Next, I would also like to thank all of the members in the Laser physics group at the Royal Institute of Technology (KTH). The first day I came to Stockholm was the 27th of August in 2003. At that time I could not communicate well with anybody because of my lack of experience in English. But, everybody always made their effort in taking time to listen my weak English speaking and also to help me in the very many private affairs which I couldn't have solved by myself. In this regards, I want to mention Associate professor emeritus Jens Tellefsen, Lars-Gunnar Andersson, Rune Persson, Agneta Falk, Dr. Carlota Canalias, Dr. Stefan Bjurshagen, Dr. Anna Fragemann, Dr. Mikael Tiihonen, Dr. Shunhua Wang, Dr. Stefan Spiekermann, Stefan Holmgren, Sandra Johansson, Jonas E. Hellström, Björn Jacobsson, Pär Jelger, Anna-Kristin Georgi, and Dr. Simonetta Grilli. Especially, I would like to give special thanks and appreciation to Jens for spending such a long time during his summer holiday for correcting my thesis and also for guiding me through initial Swedish bureaucratics in the first days and weeks of my visit to Stockholm. Carlota has always wanted to discuss the poling results with me and I have learnt a lot from her. I have always been impressed by her quick decisions and her straight way of thinking, 'yes' or 'no'. (This is the most difficult thing for a typical Japanese like me.) Mikael, Björn, Jonas, and Pär, they have helped me a lot not only during the work but also in our everyday lives. Stefan H., thanks for playing with my daughter. With all of their help, I could stay in Stockholm without any troubles for my family. Rune, he always been preparing my crystal in will the aluminum coating. Agneta, our secretary, is always helpful and has always been giving me all kinds of assistance when needed.

I would, furthermore, also thank other teachers and researchers around the world that I have been in contact with for nice and helpful discussions. Especially, it was great experience for me to work with Prof. Kenji Kitamura, Dr. Sunao Kurimura, Dr. Nan Ei Yu (National Institute of Materials Science), and Dr. Satoshi Ashihara (University of Tokyo) through the PPKN project. I also would like to thank Dr. Yasunori Furukawa (the OXIDE Corporation) and his company members for their helpful advices related to stoichiometric materials.

Finally, and needless to say, I gratefully thank my wife Mitsuko and our pretty daughter Ririka. Mitsuko has always been by my side and believes in me since we were married in 2001. Stockholm was the first place for me to live away from my own country and I encountered many difficulties. However, I managed to get over them with the extensive support and much understanding and, finally, we could enjoy our life in Stockholm very much.

Thanks to all and everybody!

Junji Hirohashi